UNIVERSITÄT
DES
SAARLANDES

Low-temperature sintering of metal-based pastes for sustainable printed electronics

Dissertation
zur Erlangung des Grades
des Doktors der Ingenieurwissenschaften
der Naturwissenschaftlich-Technischen Fakultät
der Universität des Saarlandes

von

David van Impelen

Saarbrücken

2024

Tag des Kolloquiums: 24.03.2025
Dekan: Prof. Dr.-Ing. Dirk Bähre
Berichtstatter:
Prof. Dr. Tobias Kraus, Prof. Dr. mont. Christian Motz

Vorsitz: Prof. Dr.-Ing. Markus Gallei
Akad. Mitarbeiter: Dr.-Ing. Christoph Pauly

Abstract

Low-temperature printed electronics allow for the manufacturing of high-throughput, sustainable, cheap, and flexible electronics. Silver microparticles are commonly used as conductive fillers in printing pastes, owing to silver's high conductivity and good oxidation resistance. They can be sintered at low temperatures to achieve highly conductive prints, but a mechanistic understanding is lacking. The ecological and financial impacts of using silver are high and need to be reduced.

In this thesis, I studied the low-temperature sintering of silver microflakes and spheres to screen-print recyclable and sustainable conductors. A mechanism is proposed that explains the low-temperature sintering of silver microparticles. Mechanically weak sinter necks could be created that increased the conductivity and could be broken up through probe sonication, allowing for recycling and reusing of the particles. Flakes led to more porous prints than spheres, which resulted in higher recycling yields.

The last chapters focus on the sintering of copper microparticles. We found that polymer-capped particles required high-temperature treatments in a vacuum to have a comparable conductivity to silver-based conductors. Silver-coated copper particles reached high conductivities at low temperatures in air by forming silver necks bridging the copper cores. The particles could also be recycled and reused in a new generation of prints.

Zusammenfassung

Gedruckte Elektronik ermöglicht die Herstellung von nachhaltiger, kostengünstiger und flexibler Elektronik mit hohem Durchsatz. Aufgrund der hohen Leitfähigkeit und guten Oxidationsbeständigkeit von Silber werden Silbermikropartikel häufig als leitfähige Füllstoffe in Druckpasten verwendet. Sie können bei niedrigen Temperaturen gesintert werden, um leitfähige Drucke herzustellen, aber es fehlt ein mechanistisches Verständnis. Die ökologischen und finanziellen Auswirkungen der Verwendung von Silber sind hoch und müssen daher verringert werden.

In dieser Arbeit untersuchte ich die Niedrigtemperatursinterung von Silbermikroflocken und -kugeln, um recycelbare und nachhaltige Leiter im Siebdruckverfahren herzustellen. Es wurde ein Mechanismus vorgeschlagen, der das Niedrigtemperatursintern von Silbermikropartikeln erklärt. Es konnten mechanisch schwache Sinterhälse erzeugt werden, die die Leitfähigkeit erhöhten und durch Ultraschall aufgebrochen werden konnten, was das Recycling und die Wiederverwendung der Partikel ermöglichte. Flocken führten zu poröseren Abdrücken als Kugeln, was zu einer höheren Recyclingausbeute führte.

Die letzten Kapitel befassen sich mit der Sinterung von Kupfermikropartikeln. Wir haben festgestellt, dass polymerbeschichtete Partikel Hochtemperaturbehandlungen im Vakuum benötigen, um eine mit Silberleitern vergleichbare Leitfähigkeit zu erreichen. Silberbeschichtete Kupferpartikel erreichten hohe Leitfähigkeiten bei niedrigen Temperaturen an der Luft, indem sie Silberhälse bilden, die die Kupferkerne überbrücken. Die Partikel konnten auch recycelt und in einer neuen Generation von Drucken wiederverwendet werden.

Publications and contributions

Chapter 3 and 6 of this thesis are based on papers published in peer-reviewed journals. The contribution of each author is specified.

- **Publication 1 (Chapter 3):** "Recyclability-by-design of Printed Electronics by Low-Temperature Sintering of Silver Microparticles".

  Authors: David van Impelen, Lola González-García, Tobias Kraus.

  Author contributions: Tobias Kraus and Lola González-García took part in the planning, discussion, and revisions of the manuscript. David van Impelen performed the experiments, processed the data, and wrote the paper.

  DOI: https://doi.org/10.1002/aelm.202400533

- **Publication 2 (Chapter 6)**: "Low-temperature sintering of Cu@Ag microparticles in air for recyclable printed electronics".

  Authors: David van Impelen, Lola González-García, Tobias Kraus.

  Author contributions: David van Impelen wrote the original draft of the manuscript and performed all experiments. All authors took part in the conceptualization, reviewing and editing of the manuscript. Tobias Kraus and Lola González-García were leading the supervision. Tobias Kraus was responsible for the funding acquisition and resources.

  DOI: https://doi.org/10.1039/D4TC02028F

Chapter 4 of this thesis is based on a submitted manuscript, which has not gone through a peer review yet.

- **Submitted manuscript (Chapter 4):** "The importance of shape: flakes and spheres in recyclable conductive pastes for printed electronics"

  Authors: David van Impelen, Dominik Perius, Lola González-García, Tobias Kraus.

  Author contributions: David van Impelen wrote the original draft of the manuscript and performed the majority of the experiments. Dominik Perius performed FIB-SEM tomography, made the 3D reconstructions, and wrote the section on tortuosities and 3D reconstructions. All authors took part in the conceptualization, reviewing, and editing of the manuscript. Tobias Kraus and Lola González-García were leading the supervision. Tobias Kraus was responsible for the funding acquisition and resources.

Acknowledgements

There were many people during the four years of my PhD that have helped me, motivated me, or who just gave me the push in the right direction. I will try to list all of you in this section.

I would like to start with thanking my supervisor, Professor Tobias Kraus. Your feedback and advice on scientific writing and bringing forward ideas in a clear and concise manner has been a huge help for me. I learned a lot from you and for that I am very grateful.

The second person I would like to thank is Lola González-García, who also supervised me throughout these years. I truly feel our update meetings kept me on the right track. Your door was always open, conveniently next to my office, and I felt like I could always ask you anything. Even more important, I am very grateful that you included me and Dominik to all of the fun Electrofluids activities over the years. I could not have wished for more than to be the camera man/adopted child of the Electrofluids group!

I would like to thank Anna Zimmerman for having the patience to introduce me to the TGA, and Long Zhang for giving me instructions for the four-point probe setup and the LUMiSizer.

Björn Kuttich, many thanks for always making sure there were cookies during the Christmas period. After you left, we tried to keep this tradition in our office.

The next thanks goes to Dominik and Dominik, the loyal members of the D^3. There was no better way to deal with the frustrations of a PhD than to have a good 'depression session' with you guys. Dominik Perius, thanks for all the measurements you did for me and the time you took for scientific discussions. Dominik Schmidt, thanks for all your help with experiments and your scientific input. Many figures and parts of this thesis have significantly improved by your advice.

I am also grateful to Roman Buchheit, who was not only a pleasant colleague, but also a great roommate and dear friend. Cycling home and eating wraps with you after a long day of work made the hard days a little less hard.

I had the great honor to supervise Felix Kruchten, Aya Bennouk, and Homero Tolentino. Felix, you were involved with some of the first silver sintering experiments I did, which was a great setup for chapter 3 of this thesis. Aya, you were a great Hiwi. In no time you mastered the equipment in the lab and your results contributed a lot to this thesis. Homero, you did great work in a short amount of time and for that I am very grateful. Your results taught me a lot about my own recycling experiments. And not to forget, your turtle is still guarding my desk!

Of course I cannot forget to thank Sergio Lago Garrido. Your ability to make every conversation fun is a true gift and made the coffee breaks and ice cream breaks amazing. Besides the fun, our scientific discussions and telling each other how to improve a PowerPoint figure helped me out a lot as well. And don´t worry, I will make sure to come by for visits on a regular basis.

Another special thanks goes to Maedeh Najafi. Maddie, thanks for all our fruitful discussions on the sintering of silver particles. I am very grateful for all your help with my in-situ electrical characterizations, especially with helping me solve my struggles with the setup.

To all my colleagues from both Electrofluids and Structure Formation, thanks for making my time at INM unforgettable. I won´t forget our mensa breaks, coffee breaks, and group activities.

I also want to thank my parents and family for supporting me every step on the way. Your support is what made this thesis possible.

Last, but definitely not least, I want to thank my fiance Yesica Fernanda Florez Villabona. Your support has been more valuable than I can express in words. You were always there for me after busy days in the office and carefully listened to how my day went. Going home with you is all I need after a long day. I don't know what will be the next step in my career, but I for sure know it will be with you by my side.

TABLE OF CONTENTS

1 Motivation

Electronics are all around us. You wake up with the alarm on your phone. Your smartwatch tracks your heartbeat during a run in the morning. When you get home, you open your laptop to join that online meeting. Not a day goes by without using the benefits of electronic devices and the importance of electronics in our daily lives is only expected to further increase.

Paul Eisler invented the Printed Circuit Board (PCB) in 1936, which was considered to be a milestone in the manufacturing of electronic devices [1]. Such PCBs are still the main component in the majority of electronic devices that can be found on the market today. PCBs are made by coating or laminating a copper film on a rigid substrate. Circuit designs of conductive traces can then be fabricated by using an etching process. At last, the necessary electrical components of the device are mounted onto the circuit board by soldering [2].

Despite the fact that PCBs are dominating the electronic market, there are drawbacks. PCBs generate large amounts of metal waste, require energy-intensive processes, are rigid and relatively thick, make use of environmentally unfriendly materials, and are hard to recycle [2, 3]. These downsides of using PCBs to manufacture electronics triggered research on alternative manufacturing techniques. One of these alternatives is called printed electronics.

Printed electronics have the potential to make electronic devices cheaper, lighter, flexible, more environmentally friendly, and more energy efficient [4–6]. Printed electronics can enable recycling routes after the lifetime of electronic devices. In printed electronics, a conductive paste or ink, typically metal-based, is printed on a non-conductive substrate. A large variety of substrates can be chosen, including flexible substrates. In order to achieve a high conductivity of the traces, a post treatment removes non-conductive solvents and sinters the particles. At last, additional electrical components of the circuit can be mounted onto the substrate.

Printed electronics have already reached the market and can be found in applications such as wearable devices, medical devices, and flexible displays. NFT tags that allow for contactless paying with your bank card are made through printing electronics. Nonetheless, for electronic applications where high reliability, complex circuit designs, and maximum performance are required, PCBs are still favored over printed electronics. Printed electronics typically have a shorter lifetime and cannot reach the complexity reached by using PCBs [2].

One of the main challenges that printed electronics face is to achieve as high conductivities of printed traces as can be achieved for the conductive traces in PCBs. The conductive traces of PCBs are thin copper films with a conductivity equal to the high bulk conductivity of copper ($\sigma = 5.96 \times 10^7\,\mathrm{S\,m^{-1}}$). The conductive traces in printed electronics, however, rely on the conductivity of the printed paste after the post treatment. The most common fillers of conductive pastes are silver nano- or microparticles. Such pastes can potentially achieve the bulk conductivity of silver ($\sigma = 6.3 \times 10^7\,\mathrm{S\,m^{-1}}$), which is comparable to that of copper. However, even after high-temperature treatments, the conductivity of printed pastes is typically lower [7, 8]. There is interest in research and industry to improve the electrical performance of conductive pastes at a low thermal budget and temperatures that are compatible with commonly used flexible substrates [7]. To achieve this the particles in printed pastes need to be sintered at low tempera-

tures. Due to the high surface area of nanoparticles, they typically can be sintered at low temperatures [7]. However, the large scale production is costly. Microparticles are cheaper, easier to upscale, and more readily available. Standard sintering theory predicts high temperatures are required to sinter them [9, 10], nonetheless, numerous studies have demonstrated silver microparticle sintering at temperatures below 200 °C [11–13]. There is no consensus on the sintering mechanism of such particles. In this thesis, I will elaborate on the sintering mechanism of such particles and use them to make highly conductive prints at a low thermal budget.

Silver is an expensive metal and the mining, refining, and processing is resource intensive. The embodied energy of silver is $15\,\mathrm{MJ\,kg^{-1}}$ [14], and the CO_2 equivalent emission is $25\,000\,\mathrm{kg}$ [14]. There is a strong incentive to shift from silver towards cheaper and more environmentally friendly filler materials. Researchers have investigated the use of copper in conductive pastes and some conductive pastes have already reached the market [15–18]. Challenges that arise with replacing silver include copper's tendency to form electrically isolating oxides in ambient air [19, 20]. As a result, copper-based printed conductors require energy-intensive post processing or have lower conductivities than their silver-based competitors.

The high cost of silver and its high environmental impact are also incentives to recycle the silver from printed conductors. Life cycle analysis studies have identified silver recycling as crucial for making printed electronics more environmentally friendly than PCB-based electronics [2, 3]. Metals are conventionally recycled from electronic waste through hydrometallurgical- or pyrometallurgical processes [21]. Nonetheless, these processes are complex and energy-intensive. Kwon *et al.* explored an alternative route to recycle silver from printed electronics [22]. Silver flakes could be recovered from a printed polycaprolactone matrix by submersing the prints in water. They could recover up to 94 % of the silver flakes, which they used to make a new generation of prints with similar electrical performances. Due to the absence of sintering, however, the conductivity of these conductors is much lower than the commercially available silver pastes. So far, there are no studies of recycling sintered silver particles from printed conductors. In this thesis, I recycle and reuse weakly sintered metal particles.

The ideal printed conductor can reach a conductivity close to that of bulk silver at a low thermal budget, makes use of sustainable materials, and can be easily recycled. In this thesis I design conductive pastes, focusing on these targets. In Chapter 2, I will first discuss the current state of the art in conductive pastes for metal-based printed electronics. In Chapters 3 and 4, I will discuss how silver microparticles can be exploited to create highly conductive, recyclable printed electronics at a low thermal budget. In Chapters 5 and 6, I will address how silver can potentially be replaced or partially replaced by copper to both reduce costs and increase the sustainability of printed electronics.

2 State of the art and theory

First, I will introduce the screen printing process and the requirements of conductive pastes. In the following section, common conductive fillers for conductive pastes are introduced. This work will only focus on silver and copper powders as conductive filler material. Continuing, I will discuss dominating conduction mechanisms in metal particle-based printed conductors, followed by a section on the electrical characterization of such conductors. Afterward, the sintering of metal particles and how it improves conductivity will be discussed. Then, I will give the state of the art on silver-based, copper-based, and silver-coated copper-based printed conductors, focusing on achieving high conductivity at low temperatures. In the last section, the literature on increasing the sustainability of printed electronics is presented, including sustainable material choice and recycling of the conductive filler.

2.1 Screen-printed electronics

The high throughput and possibility to print thick layers make screen-printing a popular choice in PE applications [23–25]. Figure 2.1 below shows the screen-printing process and screen-printing paste with a typical formulation.

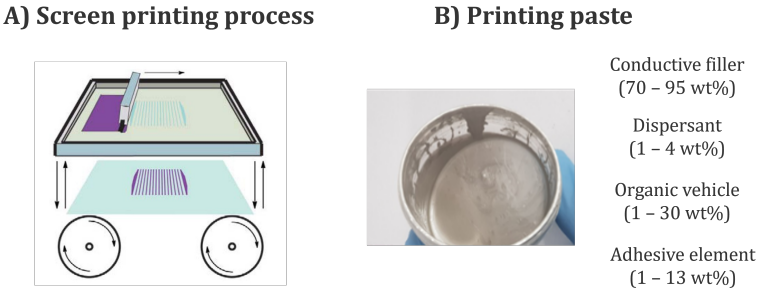

Figure 2.1: The screen-printing process for printed electronics. A) A schematic representation of a screen printer. Adapted and reprinted with permission from [26]. B) A screen-printing paste and the common paste additives [24].

The screen-printing process makes use of a screen printer, a mesh, a squeegee (the brush), a substrate, and a printing paste (Figure 2.1A). Commercial printing pastes generally contain a conductive filler (in this thesis metal particles), a dispersant to stabilize the conductive filler, an adhesive element to improve adhesion to the substrate, and an organic vehicle to control the viscosity of the pastes (Figure 2.1B). Common substrates in printed electronics are plastics, such as polycarbonate, polyimide, and poly(ethylene terephthalate) [7]. Screen-printing pastes need to be shear-thinning for the paste to flow under applied shear (printing) and be static after the desired shape is printed. The dynamic viscosity at low shear rates ($1\,s^{-1}$ or lower) should be in the range of $150\,Pa \cdot s$ to $1500\,Pa \cdot s$ and at high shear rates ($500\,s^{-1}$) in the range of $4\,Pa \cdot s$ to $15\,Pa \cdot s$ [23].

The mesh consists of a metallic frame with polyester or stainless steel wires spanning the frame. The mesh count is the amount of threads per squared inch of the mesh. The printed layer thickness can be tuned by tuning the mesh count: increasing the mesh count decreases the printed layer thickness. To

create a pattern a photo emulsion is applied to the mesh, an acetate sheet featuring the pattern is placed over the mesh, and the photo emulsion is hardened through UV exposure. After removing the acetate sheet and washing out the photo emulsion underneath, the patterned mesh is obtained.

For printing the paste is applied below the pattern, followed by filling the pattern with the squeegee, lowering the mesh onto the substrate, and pushing the paste onto the substrate. Afterward, the prints require a post-treatment to remove organic solvents (the organic vehicle) and sinter the particles to increase the conductivity. The sintering process will be discussed in more detail in Section 2.4.

2.2 Conductive fillers in printing pastes

Metals, carbon-based materials, and conducting polymers are used as a filler material in conductive paste formulations [4, 5, 27–29]. Metals are a logical choice due to their high intrinsic conductivity. The most common choices are gold ($\sigma = 4.42 \times 10^7\,\mathrm{S\,m^{-1}}$), silver ($\sigma = 6.3 \times 10^7\,\mathrm{S\,m^{-1}}$), aluminium ($\sigma = 3.78 \times 10^7\,\mathrm{S\,m^{-1}}$), copper ($\sigma = 5.96 \times 10^7\,\mathrm{S\,m^{-1}}$), and nickel ($\sigma = 1.43 \times 10^7\,\mathrm{S\,m^{-1}}$) [5,30]. The stability towards oxidation benefits silver and gold, but they are costly. Copper, aluminum, and nickel have the tendency to oxidize and anti-oxidation strategies are required. However, they often increase post-processing cost and complexity [19, 20, 31].

Metal-based fillers exist as nanoparticles, microparticles, and nanowires. The high aspect ratio of nanowires makes it possible to make conductive ink formulations already at very low filler concentrations. However, their tendency to agglomerate makes it challenging to create stable paste formulations with good printability [32]. Furthermore, the high cost and difficulty of upscaling synthesis limit their use in commercial conductive pastes [32]. Nanoparticles have the advantage of requiring a post treatment temperature typically below 200 °C, which makes it compatible with common flexible substrates [7]. The large-scale production of nanoparticles is still challenging and costly. Nanoparticle loading of inks is typically low due to their tendency to agglomerate, which makes it difficult to print thick layers. Microparticles are cheaper, easier to upscale, and allow for higher metal loading in the paste. They often require a high post treatment temperature, limiting the substrate choice and increasing the thermal budget of the manufacturing process of printed electronics [4]. Strategies to reduce the required post treatment temperature are discussed in Section 2.5.

Carbon materials and conductive polymers can yield highly flexible and stretchable electronics, but their conductivity is lower than metal-based printed conductors [5, 28, 29]. In the remainder of this thesis, I will focus only on the use of metal particles for printed electronics. We will first look at conduction mechanisms and electrical characterization of thin film, particle-based conductors.

2.3 Conductivity of printed conductors

Screen-printing of conductive pastes based on metal particles forms thin particle layers with typical thicknesses of below 100 µm [24]. In this section, I will first discuss the conduction mechanisms that contribute to the electrical conductivity of the printed material. Afterward, I will discuss how such thin films can be electrically characterized.

2.3.1 Conduction mechanisms in particle packings

The conductivity of a particle packing is determined by the ease of electron transport from particle to particle, which is determined by the particle-particle contact properties. I will define two types of contacts between particles here: ”direct” metal-metal contacts and tunneling contacts. For direct contacts, the metal surfaces are assumed to be in contact without an air gap separating the surfaces. Tunneling contacts are contacts where the metal surfaces are separated by a thin air gap. I will define the area of the direct particle-particle contacts A_1, and the area of tunneling contacts A_2.

The resistance of electron flow through direct contacts is called constriction resistance [33]. The constriction resistance decreases with increasing A_1. Compaction of the powder compact increases A_1 and therefore decreases the constriction resistance. Without applying an external force on the particle packing, A_1 is small and the macroscopic resistivity of the particle layer is much higher than the intrinsic resistivity of the particles [33–35].

The tunneling resistance scales exponentially with the tunneling distance [35]. Therefore, tunneling only contributes to conduction when the tunneling distance, hence the distance between the particle surfaces, is short enough. The current through a tunneling contact can be described as follows:

$$J = C_0 \cdot V \cdot \exp \frac{-d}{\varsigma}, \tag{2.1}$$

where J is the current density, C_0 the characteristic conductance, V the applied voltage, d the tunneling distance, and ς the characteristic tunneling length. The current flux through a tunneling contact, even with short tunneling distances, is generally lower than the current flux through restriction contacts. Nonetheless, since A_2 often is much larger than A_1, tunneling cannot be neglected and significantly contributes to the conductivity of printed metal particle layers [35].

2.3.2 Electrical characterization of thin film conductors

The most common way to electrically characterize thin film conductors is by using a four-point probe setup (see Figure 2.2).

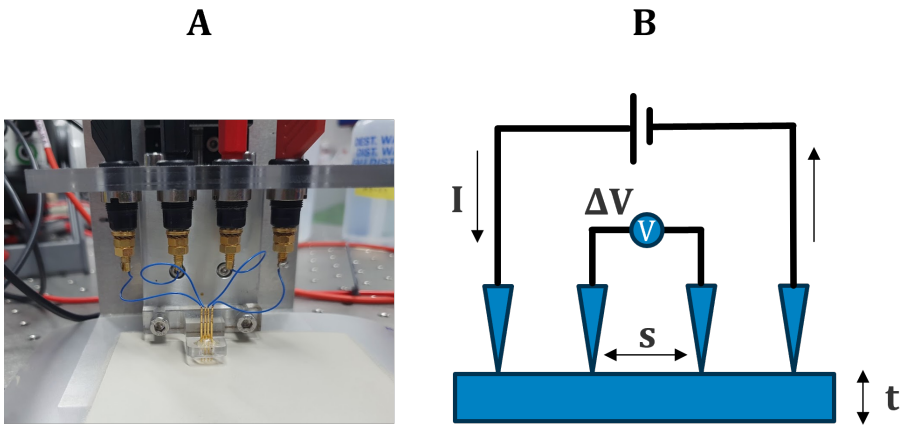

Figure 2.2: The four-point probe setup for electrical characterization of prints. A) Image of the setup. B) Schematic illustration of the setup. I is the current through the outer pins, ΔV the voltage drop over the inner pins, s the spacing between the pins, and t the thickness of the sample.

The four measurement pins are equally spaced and placed in the middle of the printed sample. The outer two pins are connected to a current source, while the inner two pins are connected to a voltmeter. The voltage is incrementally increased while measuring the current through the outer circuit. Then, the resistance between the inner two pins can be calculated through Ohm‘s law:

$$R_{\text{inner}} = \frac{\Delta V}{I}, \tag{2.2}$$

where I the current through the material, and ΔV the voltage drop over the inner two pins. R_{inner} can be converted to sheet resistance (R_{sh}) [36],

$$R_{sh} = \frac{\pi}{\ln(2)} \cdot R_{\text{inner}}. \tag{2.3}$$

R_{sh} is a property of the printed film and depends on the film thickness. For Equation 1.3 to be valid, the lateral dimensions of the sample need to be at least 40 times larger than the probe spacing, so that the current paths are not limited by the sample edges [37]. The thickness of the film needs to be less than $40\,\%$ of the probe spacing, so that current can be assumed to propagate cylindrically through the entire layer thickness instead of spherically, as is the case for thicker samples [36].

In this thesis, the probe spacing is $1\,\text{mm}$, the samples have a lateral dimension of 1 by $3\,\text{cm}^2$, and thicknesses ranging from $20\,\mu\text{m}$ to $80\,\mu\text{m}$. The thickness requirement is fulfilled, but the lateral dimensions are slightly smaller than 40 times the probe spacing. Based on the lateral dimensions, R_{sh} from Equation 1.3 is multiplied by a correction factor of 0.9345 to obtain the true sheet resistance.

If the film thickness is known, the bulk resistivity (ρ) can be calculated by,

$$\rho = t \cdot R_{\text{sh}}, \tag{2.4}$$

where t is the film thickness, and R_{sh} the sheet resistance [36]. The bulk resistivity treats the film as a homogeneous conductor and does not contain information about the metal content of the printed film. Reducing the metal content, however, is a common goal in printed electronics to reduce cost and

environmental impact.

An effective way to take the metal content into consideration is to use a mass-normalized sheet resistance,

$$R_{m/\mathrm{sh}} = m * R_{\mathrm{sh}}, \tag{2.5}$$

with m the metal mass of the printed layer. Minimizing $R_{m/\mathrm{sh}}$ equals maximizing the conductivity at minimal metal content. $R_{m/\mathrm{sh}}$ will be used throughout the entire thesis.

Metal-based printed conductors are post-treated to induce sintering and increase electrical conductivity. The sintering process and its effect on the electrical conductivity will be discussed in detail in Section 2.4. The four-point setup, as shown in Figure 2.2, was used for the electrical characterization of all sintered conductors in this thesis. The robustness of the setup is a result of decoupling current and voltage measurements, which discards pin-to-layer contact resistances. However, this setup cannot be used to track conductivity changes *in situ* during the sintering of the printed films, which can give insights into the sintering mechanism. For this purpose, I used an alternative electrical characterization setup (see Figure 2.3).

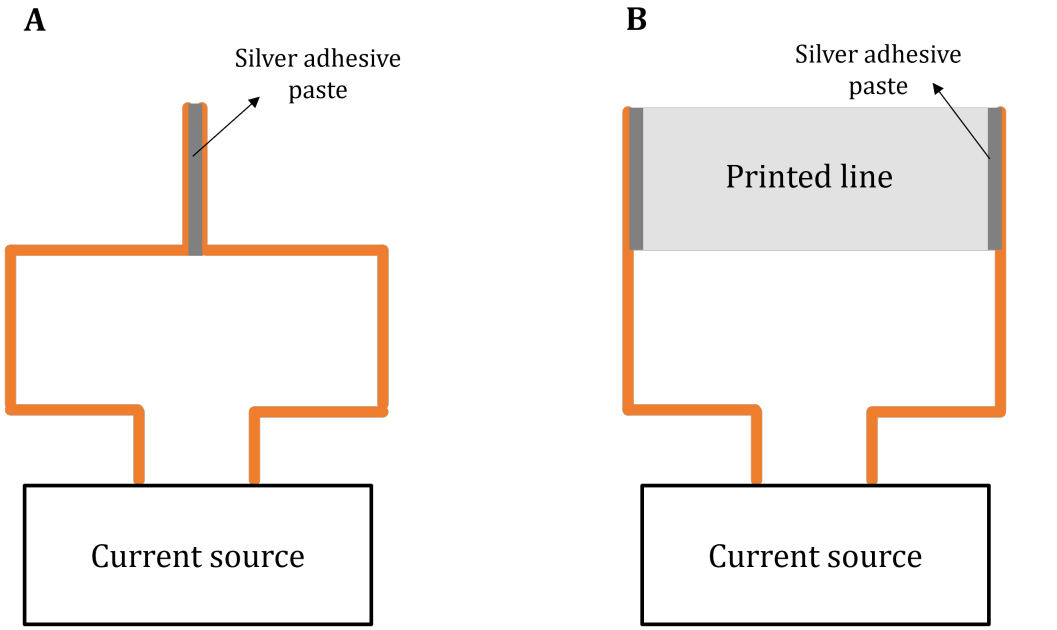

Figure 2.3: Schematics of the *in-situ* electrical characterization setup. A) The reference circuit. B) The circuit with a connected sample. The resistance of circuit B minus the resistance of circuit A results in the resistance of the printed sample.

Two copper wires of equal length were glued with conductive adhesive to the short edge of the printed lines. These copper wires were attached to the same source meter as used in the four-point measurement setup (see Figure 2.3B). In contrast to the four-point probe setup, the current and voltage determination is

not decoupled in this setup, and the contact- and wire resistances need to be taken into consideration. For each experiment a reference sample was made, existing out of two copper wires with the same length, connected with silver adhesive paste on one end, and connected to a source meter on the other end (see Figure 2.3A). The measured resistance of the reference sample was assumed to be equal to the sum of wire- and contact resistances in the printed sample setup. By subtracting the measured sample resistances from the reference resistance, the printed line resistance was obtained. Since the dimensions of the printed line are 1 by 3 cm^2, dividing the line resistance by 3 resulted in the sheet resistance. The validity of this setup was also checked by comparing the results to the sheet resistances obtained from a standard four-point probe measurement (see Table 9.1 of the Supporting Information).

2.4 Sintering of powder compacts

Sintering is the process in which a powder compact is turned into a full-density object through heating [9, 38]. The driving force is the reduction of interfacial area, which is equivalent to reducing the Gibbs free energy of the powder. The sintering process can make materials more strong, more ductile, less porous, and more conductive (in the case of metals). These changes in material properties are caused by the geometrical changes that are induced by sintering [9].

Archeological artifacts suggest that the sintering process dates back to almost 24000 BC [9]. Humans found that the firing of pottery and ceramic objects could lead to stronger materials. The first written reports on the sintering process were made in the 17^{th} century. Since then, a wide range of sintering applications have appeared over the years [7, 39–41]. Sintering played an important role in the development of the light bulb, the fabrication of hard tools for shaping artificial diamonds, the manufacturing of self-lubricating bearings [42], and manufacturing of complex parts for the automotive industry. After the Second World War, sintering was applied to electronic, dental, and medical devices.

For printed electronics, sintering is used to increase the conductivity of particle-based, printed traces [7, 8]. The conductivity of a printed trace consisting of metal particles is limited by the contact resistances among the particles [43, 44]. In order to compete with the conductivity of conductive traces in PCB technologies, these contact resistances should be strongly reduced. Sintering induces the formation of metallic connections among the particles, so-called sinter necks, which strongly reduce contact resistances [9]. This is illustrated in Figure 2.4 below.

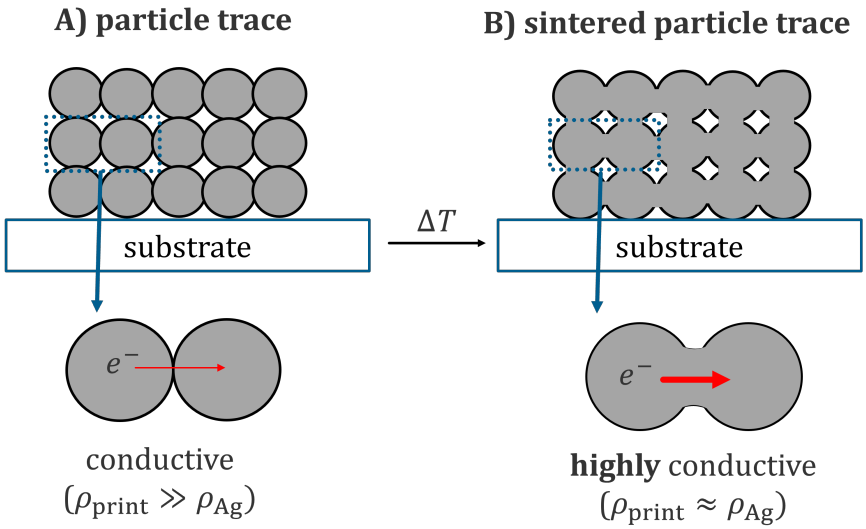

Figure 2.4: The effect of sintering on the conductivity of printed metal particle layers. A) A schematical representation of a printed trace of untreated metal particles is shown. Electrons can pass through the particle-particle interfaces, rendering the trace conductive. Contact resistances at the particle-particle interfaces limit the resistivity of the trace, resulting in orders of magnitude higher resistivity compared to the respective metal. B) Heat-induced sintering of the particles leads to the formation of sinter necks among the particles. Particle-particle resistances are diminished and a resistivity close to that of silver can be achieved.

2.4.1 Sintering stages: from powder compact to full density

The process can be divided into three stages: initial stage, intermediate stage, and final stage [9, 38]. In this section, I will use two main indicators of sintering to discuss the different stages, namely the neck size and the density of the powder compact. The neck size is typically expressed as the ratio of neck diameter to particle diameter (X/D). Figure 2.5 shows both the initial neck geometry and the geometrical changes that occur through sintering.

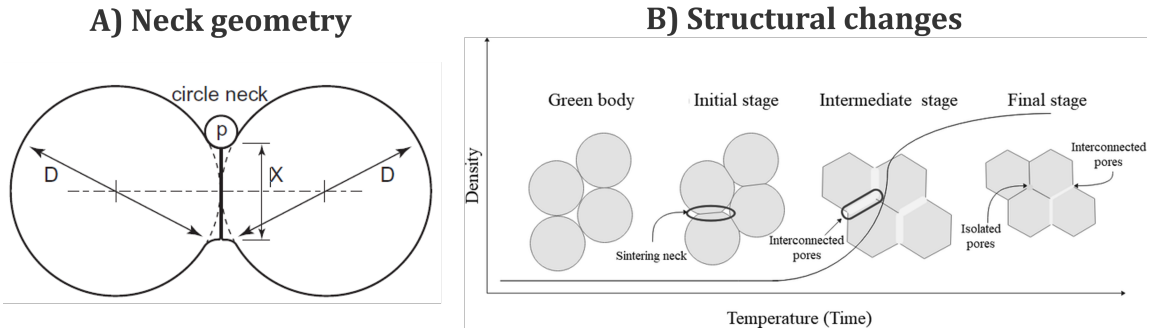

Figure 2.5: Initial neck geometry and structural changes upon sintering of a powder compact. A) Neck geometry of necks formed in the initial stage of sintering. Sintering results in the formation of saddle-shaped necks. D is the particle diameter, X the sinter neck diameter, and p the saddle neck radius. Adapted and reprinted with permission from [9]. B) Figure from: "Influence of Sintering Parameters on the Structure of Alumina Tubular Membranes Obtained by Freeze-Casting", by P. Cristh Fonseca Alves, Journal of Ceramic Science and Technology, Volume 14, Issue 2, Copyright (c) 2023. Available under Creative Commons Attribution 4.0 International (CC BY 4.0). Structural changes that the powder compact undergoes through sintering from a powder to a dense compact. The starting geometry is the green body powder compact. At the initiation of sintering necks are formed (initial stage). Necks grow, leading to interconnected tubular pores (intermediate stage). Further sintering collapses the tubular pores into closed/isolated spherical pores (final stage).

The initial density of the powder compact, the 'green body density', is determined by the packing of the particles. It affects the coordination number of each particle, which can have an effect on both the onset of sintering as well as its kinetics. The particles are connected with each other through point contacts, which are kept together by weak van der Waals forces. When the sintering is initiated upon heating, the particle contacts grow in size and form grain boundaries. Grain boundaries that connect two particles are called sinter necks. The contact growth and initial neck formation start the initial stage of sintering (Figure 2.5B, initial stage). The initially formed necks have a saddle-like shape [9] (Figure 2.5A). Necks grow independently in size and do not yet interact with neighboring necks. The surface curvature is the main driving force of initial stage sintering [9, 45, 46]. Initial stage neck growth continues until X/D exceeds a value of 0.33, which is the point at which necks lose their individuality and start to interact with neighboring necks.

In the intermediate stage, necks start to overlap, and open pores throughout the powder compact are formed (Figure 2.5B, intermediate stage). The pore sizes increase through the merging of neighboring pores. Grain growth makes the pores more round and smooth. These effects generate tubular pores throughout the powder compact. They grow longer and the diameters decrease, until the pores become unstable and collapse into spherical pores. This collapse typically occurs at a density of 90 % to 92 %,

which introduces the final stage of sintering [9] (Figure 2.5B, final stage).

In the final stage of sintering, the closed pores decrease in size until the full density of the powder compact is reached.

2.4.2 Mass transport mechanisms

Sintering a porous powder compact to a dense material occurs through diffusion-based mass transport processes [9, 38]. Multiple mass transport mechanisms can concurrently contribute to neck growth and densification during sintering. The most common ones are schematically represented in Figure 2.6 below.

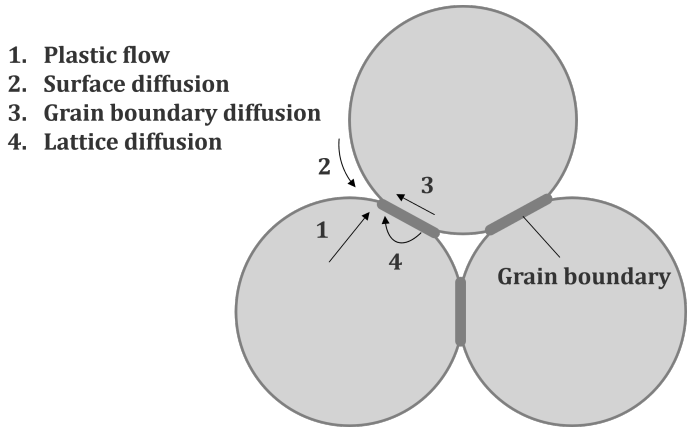

Figure 2.6: Common mass transport mechanisms in powder sintering. 1) Plastic flow, 2) surface diffusion, 3) grain boundary diffusion, 4) lattice diffusion.

One of the first models that predicted neck growth over time was provided by Frenkel [47]. Frenkel assumed the sintering of two amorphous spheres with mass transport only through viscous flow induced by capillary forces that act upon the particles (Figure 2.6, 1). These capillary forces scale with the curvature of the necks that decreases as neck sizes grow larger, hence the driving force for this transport mechanism is larger during the initial phase of sintering [9]. Experiments on initial stage sintering of glass spheres were in good agreement with Frenkel's model of neck growth by viscous flow [48, 49]. Crystalline particles exhibit other transport mechanisms and other models are required [9].

Material transport to the neck over the particle surface occurs via surface diffusion (Figure 2.6, 2). The surface of crystalline particles contains defects, such as extra atoms, vacancies, terraces, ledges, and kinks. The defects act as pathways for atom diffusion over the surface and are called material sinks, while the atoms that can move toward these sites are called material sources. A concave surface (the sinter neck) has a higher density of sinks compared to a convex surface (particle surface), which generates a gradient of material sinks towards the sinter neck [9]. This gradient is the driving force for material transport towards the neck. In the initial stage of sintering, mass transport is dominated by surface diffusion [9, 50]. As sintering progresses the curvature of necks and the driving force for surface diffusion towards the neck decreases. At a certain point, the driving force is too small, and bulk diffusion takes over.

The two most common bulk diffusion transport mechanisms are grain boundary and lattice diffusion [9, 10, 38]. A grain boundary is the interception of two adjacent grains and has a high defect density. Mass transport along these grains is called grain boundary diffusion. Atoms can also diffuse through the

lattice by vacancy hopping or movement at interstitial sites in the crystal lattice. Such diffusion is called lattice diffusion. The high defect density of grain boundaries makes material transport along the grain boundaries a process with lower activation energy compared to material transport through the lattices. Therefore, it is in most cases grain boundary diffusion that takes over from surface diffusion after the neck curvature has diminished [9, 50]. A fundamental difference between surface and bulk diffusion (grain and lattice diffusion) is that bulk diffusion leads to densification of the powder compact, while surface diffusion does not. The fact that surface diffusion dominates the initial stage of sintering therefore explains why most of the powder densification occurs in the intermediate and final stage of sintering.

2.4.3 The effect of temperature

Sintering is a thermally activated process with a defined onset temperature. It is often compared to the glass transition temperature of polymers, which marks the transition from frozen chains to liquid-like chains that have high mobility and the capability to flow [9]. An early technique to determine the sintering onset temperature was to mechanically stir a chamber filled with powder [9]. The powder was heated until the motor was no longer capable of stirring, which was determined to be the onset temperature of sintering. In this way, the 'sintering temperature' of iron in vacuum was found to be $750\,^{\circ}\mathrm{C}$, roughly $49\,\%$ of the melting temperature of iron [9]. More accurate tools are now used to quantify the sintering process which focuses mainly on neck size, densification, and specific surface area. The most common tool to determine the sintering onset temperature is the dilatometer, which can measure the shrinkage of a powder compact [9, 51].

In the initial stage of sintering the main parameter of interest is the neck size, since not much densification occurs yet. Equations that predict the rate of neck growth in the initial stage during isothermic sintering have the following form [9]:

$$(\frac{X}{D})^{\mathrm{n}} = \frac{B \cdot t}{D^{\mathrm{m}}} \tag{2.6}$$

,

where X is the neck radius, D the particle diameter, B a term of geometrical and material constants, and t the time. The integers n, and m, and the parameter B have been established for several of the material transport mechanisms described in the previous section. Figure 2.7 shows an overview of them for the different transport mechanisms.

$(X/D)^n = B\ t\ /\ D^m$

Mechanism	n	m	B
viscous flow	2	1	$3\ \gamma\ /\ (\eta)$
plastic flow	2	1	$9\ \pi\ \gamma\ b\ D_V\ /\ (R\ T)$
evaporation–condensation	3	2	$(3P\ \gamma\ /\ \rho^2)\ (\pi/2)^{1/2}\ (M\ /\ (R\ T))^{3/2}$
volume diffusion	5	3	$80\ D_V\ \gamma\ \Omega\ /\ (R\ T)$
grain boundary diffusion	6	4	$20\ \delta\ D_B\ \gamma\ \Omega\ /\ (R\ T)$
surface diffusion	7	4	$56\ D_S\ \gamma\ \Omega^{4/3}\ /\ (R\ T)$

symbols

γ = surface energy, J/m^2
η = viscosity, Pa·s
b = Burgers vector, m
R = gas constant, J/(mol K)
T = absolute temperature, K
ρ = theoretical density, kg/m^3
δ = grain boundary width, m
D_V = volume diffusivity, m^2/s
D_S = surface diffusivity, m^2/s
D_B = grain boundary diffusivity, m^2/s
P = vapor pressure, Pa
M = molecular weight, kg/mol
Ω = atomic volume, m^3/mol

Figure 2.7: Initial stage sintering equations. Adapted and reprinted with permission from [9].

The parameter B contains material properties, such as the diffusion coefficient, and depends on the temperature:

$$B = \mathrm{B}_0 \cdot \exp \frac{-Q}{RT}, \tag{2.7}$$

where B_0 is a pre-exponential factor, Q the activation energy, R the gas constant, and T the temperature. Due to this exponential dependency of the temperature, changing the sintering temperature has a stronger effect on the sintering rate than increasing the sintering time.

Surface diffusion dominates the initial stage of sintering for most crystalline materials. Figure 2.8 shows the neck-to-particle diameter ratio for 1.5 µm particles as a function of time as calculated from equation 2.1, where n, m, and B are taken from surface diffusion in Figure 2.7.

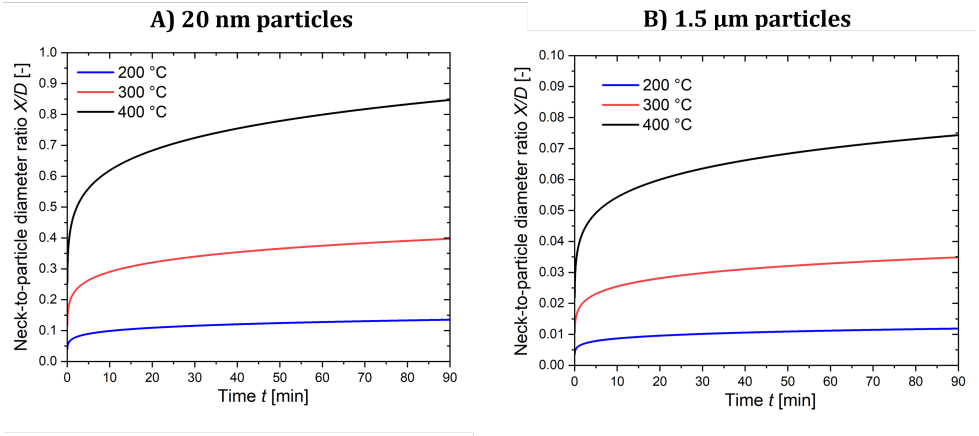

Figure 2.8: Sinter neck growth over time at different temperatures calculated by the two-particle sintering model based on the equation on surface diffusion, as provided in Figure 2.7, of A) 1.5 µm-diameter silver particles, and B) 20 nm-diameter silver particles. The ratio of neck diameter X over the particle diameter D is plotted as a function of time for sintering at 200 , 300 , and 400 °C.

For $1.5\,\mu m$ particles to form necks with a size of $X/D = 0.05$ within $90\,min$, the two-particle model predicts a required temperature of at least $400\,°C$ (Figure 2.8B). Despite this prediction, many examples of silver microparticles sintered at lower temperatures are presented in literature and alternative sinter mechanisms have been proposed. I will discuss these examples in the following section.

For $20\,nm$ particles necks with a size of $X/D = 0.1$ are formed after only $10\,min$ at $200\,°C$ (Figure 2.8A). In the following section, I will discuss the use of silver nanoparticles in printed conductors.

2.5 Silver-based printed conductors

This thesis covers printed conductors based on silver and copper microparticles. The aim is to sinter the particles at a low temperature to achieve high conductivities at a low thermal budget. The temperature should be compatible with common substrates used in printed electronics, which generally cannot withstand temperatures above $200\,°C$ [7]. Recycling and reusing the particles is an additional objective, which will be further discussed in Section 2.8.

In this section, the low-temperature sintering of silver particles and their use in printed conductors are discussed. Both silver nano and microparticles can be sintered at low temperatures [7, 11–13]. The low-temperature sintering of silver nanoparticles is usually attributed to the high surface area, which predicts a lower sintering onset temperature [7]. Low-temperature sintering of microparticles is less understood and cannot be predicted by surface and grain boundary diffusion mechanisms.

I will first discuss the state of the art in low-temperature sintering of silver nanoparticles, followed by the state of the art for silver microparticles. At last, the effect of the shape of silver microparticles on conductivity and sintering behavior will be discussed.

2.5.1 Sintering of silver nanoparticles

Silver nanoparticles (NPs) can already be found in several industrial conductive pastes on the market [52–54]. Their most attractive feature is the highly mobile nature of atoms on the particle surface [7]. NPs have a large surface area and high surface curvatures, which strongly increases diffusivity on the particle surface [9]. Since initial stage sintering is dominated by surface diffusion, sintering onset temperatures are typically much lower, and the rate of neck formation is much higher compared to micron-sized particles.

NPs require surfactants that stabilize the particles in pastes [7, 8]. They impede electron flow and need to be partially removed to achieve a high conductivity of the printed traces. Common surfactants include polymers, amines, and carboxylic acids [55]. Their decomposition temperature is often above $250\,°C$, but in certain cases, they can detach from the surface below these temperatures [7].

A common surfactant for silver NPs is polyvinylpyrrolidone (PVP) [8, 56, 57]. Mo *et al.* made pastes containing synthesized silver NPs with sizes ranging from $48\,nm$ to $176\,nm$ [57]. They could control the size distribution by varying the Ag^+ concentration in the reaction process. Interestingly, they found that increasing particle size increased the conductivity of printed traces. They proposed that PVP limited the conductivity and with increasing particle size the PVP content decreased. The best resistivity was achieved for $158\,nm$-diameter silver NPs, which at $140\,°C$ for $10\,min$ resulted in a resistivity of only 2.89 times that of bulk silver. Ding *et al.* argued that not only the size of NPs is important, but also the

width of the size distribution [56]. By using a ratio of $AgNO_3$ to PVP of 1:0.4, they obtained a broad size distribution with an average particle size of 93 nm, which resulted in a densely packed layer after screen printing. A resistivity of 2.4 times that of bulk silver was obtained after treatment at 160 °C for 75 min.

In 2010 Magdassi *et al.* introduced a strategy to remove the ligand around the particles chemically, leading to spontaneous sintering of the NPs at room temperature [58]. They found that treating NPs with electrolytes, such as NaCl, leads to the replacement of the ligands by Cl^- ions. As a result, the 11 nm-sized particles formed sintering necks, which they referred to as coalescence. The coalescence of printed traces of NPs resulted in high conductivities up to 20 % that of bulk silver. In later work of Magdassi *et al.*, they optimized the salt concentration and could achieve 41 % that of bulk silver at room temperature [59]. Additionally, they optimized the process by first inkjet printing the silver paste, followed by inkjet printing an electrolyte solution on top of the layer as a sintering treatment [60].

Conductive pastes based on silver NPs still face several challenges. Inkjet printing of silver NPs, such as in the work of Magdassi *et al.*, requires printing multilayers [58, 59]. Screen printing, as done by Ding *et al.*, yields thin layers with a thickness of only 4 µm [56]. In industrial applications, thicker prints might be required to achieve low resistance over long line distances. Furthermore, the NPs they developed require a long sintering time of 75 min. The synthesis of NPs is still usually complex and time-consuming, making it less attractive for industrial applications [61]. In the next section, low-temperature sintering of silver microparticles for their use in printed conductors will be discussed.

2.5.2 Sintering of silver microparticles

Silver microparticles currently are the industrial standard for conductive pastes used in printed electronics. They are available at large scale, synthesis routes are less complex than for NPs, and they generally have good stability in conductive pastes. The main challenge for silver microparticles is to keep the post treatment temperature low while keeping a high conductivity. Microparticles have a lower surface curvature than nanoparticles and higher expected sintering temperatures (Figure 2.8). Surprisingly, there are several examples of sinter neck formation of silver microparticles below 200 °C (Figure 2.9) [11–13].

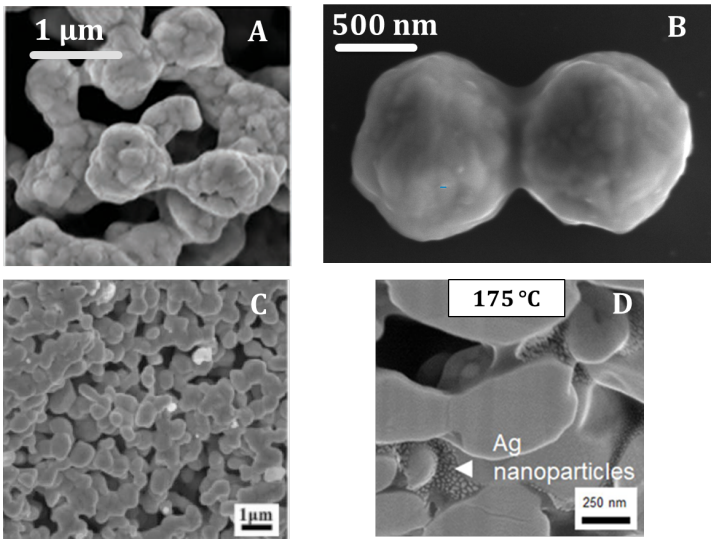

Figure 2.9: Examples of low temperature sintering of silver microparticles. Scanning electron microscope images of silver microparticles sintered at A) 150 °C [12]. Image from: "Facile and Scalable Synthesis of Ag Nano-Flowers that Can be Sintered Below 120 °C", by Zeliang Guo, Advanced Electronic Materials, Volume 9, Issue 26, Copyright (c) 2022. Available under Creative Commons Attribution 4.0 International (CC BY 4.0). B) 140 °C (our work) C) 140 °C. Adapted and reprinted with permission from [11] D) 175 °C. Adapted and reprinted with permission from [13]. In each example, the formation of sinter necks can be observed.

Guo *et al.* achieved a resistivity of $1.7 \cdot \rho_{Ag}$ by sintering 1.3 µm-diameter silver particles at 150 °C for 30 min (Figure 2.9A) [12]. They were able to synthesize microparticles composed of silver nanosheets. They attributed the low sintering temperature to the fine nanoscale surface features. Zhan *et al.* treated silver micro flakes (0.5 µm to 1.5 µm, thickness 30 nm) with $NaNO_3$ and succinic acid and found that 140 °C after 30 min led to a resistivity of $67.5 \cdot \rho_{Ag}$ [11]. They suggested that the $NaNO_3$ and succinic acid removed surfactants, etched silver, and aided sintering.

Other studies found silver nanoparticles formed *in situ*, which they linked to the low sintering temperature of silver microparticles (Figure 2.10) [13,62,63]. Yeom *et al.* observed nanoparticle formation from silver micro flakes (average diameter 8 µm, thickness 260 nm) at 250 °C and attributed this to the release of microstrains in the silver flakes (Figure 2.10) [62]. Later, the same group observed nanoparticle formation from spherical silver microparticles (Figure 2.10) [13]. They treated a bimodal micro powder (quasi-spherical with average diameters of 0.4 and 2.5 µm) at 175 °C and attributed the nanoparticle formation to the presence of a polyvinylpyrrolidone (PVP) surfactant on the surface of the particles. This surfactant was proposed to form a complex with silver ions on the surface, leading to an accumulation of ions that later precipitated to form nanoparticles. Matsuhisa *et al.* sintered silver microflakes with $\sim$ 5 µm diameter at 140 °C in a fluoroelastomer matrix and observed the formation of silver nanoparticles [63]. Additionally, they saw an increase in nanoparticle population upon adding a fluorine-based surfactant S-386 to the matrix. They proposed that Ag^+ that was formed on the silver surface diffused into the polymer where it was reduced by the fluorine surfactant to form nanoparticles. Interestingly, all the above studies observed the *in-situ* formation of nanoparticles, but they all provide different explanations. Furthermore, none of these studies clearly describe how the nanoparticle formation could contribute to low-temperature neck formation in silver microparticles.

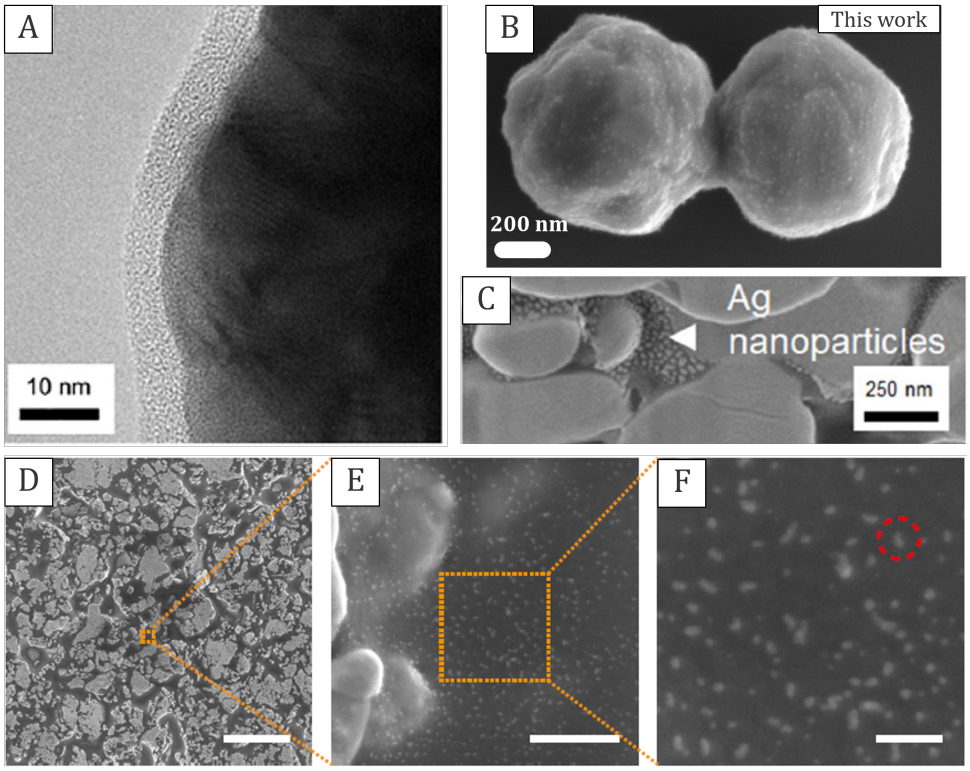

Figure 2.10: Electron microscope images of silver nanoparticles that formed *in situ* during sintering of silver microparticles. A) TEM images showing formed silver nanoparticles at the outer edge of the silver microparticle. Adapted and reprinted with permission from [62]. B) SEM image of two sintered silver microparticles with silver nanoparticles on their surface (own work). C) Silver nanoparticles that formed between the sintered microparticles. Adapted and reprinted with permission from [13]. D-F) SEM images of silver nanoparticles formed among silver microflakes during sintering. Adapted and reprinted with permission from [63].

In Chapter 3 of this thesis, I will focus on the origin of *in-situ* nanoparticle formation, how it depends on particle type and chemical environment, and especially on what role it plays in the low-temperature necking mechanism of silver microparticles. I will formulate a hypothesis that can explain the differences in sintering temperature observed for different types of silver particles and provides an explanation of why many silver particles can already form silver necks at such remarkably low temperatures.

2.5.3 Sintering of microscale silver flakes and spheres

Microscale flakes and spheres are dominating the market and are used in printing conductive traces from silver-based pastes [12, 13, 62, 64]. This section discusses the differences between flakes and spheres in sintering, conductivity, and recyclability.

The flat and elongated nature of flakes typically creates larger particle-particle contact areas than spheres [64]. The conductivity of a printed trace of particles is limited by the resistance of such particle contacts [43, 44]. They are caused by the constriction resistances at small particle-particle contacts and tunneling resistances due to insulating interlayers [33]. The larger the particle-particle contact area, the lower this resistance, and therefore the lower the resistance of the printed particle trace. It is therefore expected that prints based on flakes have a lower resistance than prints based on spheres. The formation of sinter necks

changes the picture, and the size of the necks starts to determine the particle-particle contact resistance and thus the resistance of the prints. It remains unclear whether sintered flakes or sintered spheres result in a higher conductivity.

In Chapter 4 of this thesis, I will compare flakes and spheres treated at different temperatures. I will compare conductivities at temperatures below and above the onset temperature of neck formation. Additionally, the recyclability of weakly and strongly sintered flakes and spheres will be compared. I will elaborate more on the recyclability of printed electronics in Section 2.8.

2.6 Copper-based printed conductors

The mining, refining, and processing of silver are resource-intensive processes. Silver has an embodied energy of $15\,\mathrm{MJ\,kg^{-1}}$ [14], and a CO_2 equivalent emission of $25\,000\,\mathrm{kg}$ [14]. Silver prices have been above 10 USD per ounce (353 USD per kilogram) since the year 2005. There are strong ecological and economic incentives to replace silver with a cheaper and more sustainable alternative.

Copper has a high conductivity ($\sigma = 5.96 \times 10^7\,\mathrm{S\,m^{-1}}$) [65], is cheaper than silver [66, 67], and more abundant [68, 69]. Many studies have investigated the potential of copper replacing silver [31, 70, 71]. The main challenge is that copper spontaneously forms electrically isolating native oxide layers in air, which both increases the sintering temperature and the electrical resistance of copper-based prints [19]. A common strategy is to sinter the prints in a vacuum or controlled atmosphere, but temperatures above $250\,^\circ\mathrm{C}$ are usually required [70, 71].

The two most stable oxide phases of copper are Cu_2O and CuO. A clean copper surface readily oxidizes under ambient conditions to form a native oxide layer. It is predominately Cu_2O, though some studies have also detected the presence of CuO [72, 73]. The thickness of this oxide layer depends on parameters such as humidity and temperature but is said to be a few nanometers under ambient conditions [72–74]. The native oxide layer passivates and prevents further growth. Choudhary demonstrated that the activation barrier for oxide diffusion through the native oxide layer of a $100\,\mathrm{nm}$ copper film occurred at a temperature of $150\,^\circ\mathrm{C}$ [75]. The resulting oxidation leads to a strong increase in the sheet resistance of the thin film. X-Ray diffraction analysis (XRD) revealed the formation of Cu_2O at $200\,^\circ\mathrm{C}$ and CuO at $320\,^\circ\mathrm{C}$. These observations are in line with many other literature studies that also conclude that CuO_2 is first formed, and is converted to CuO at higher temperatures [72, 76–78]. Both Cu_2O and CuO impede electron flow through copper interfaces. Their higher melting points increase the sintering temperature of the copper particles [19]. To keep treatment temperatures low and the conductivity high, it is, therefore, crucial to prevent copper oxidation during the heat treatment of printed conductors based on copper particles.

Copper pastes for printed electronics require a conductive copper filler material, an anti-oxidation strategy, and a post treatment to increase the conductivity (see Figure 2.11). The copper filler material can be divided into nano- and microparticles. Microparticles generally need a high temperature for sintering. Nanoparticles, due to their high surface curvature, can be sintered at much lower temperatures. However, they have a larger surface area and are more prone to oxidize than microparticles [78]. Common anti-oxidation strategies for nano- and microparticles include capping particles with a polymer or small organic molecules [79, 80], coating particles with metals [71, 80], and adding additives in the paste for-

mulations [81, 82] (Figure 2.11). Capped particles have polymers or molecules attached to the surface that block oxygen diffusion. Additives are present in the paste and slow down oxidation through their interaction with oxygen. Coatings on particles are dense layers, typically metals, covering the surface and preventing oxygen from reaching the particle core.

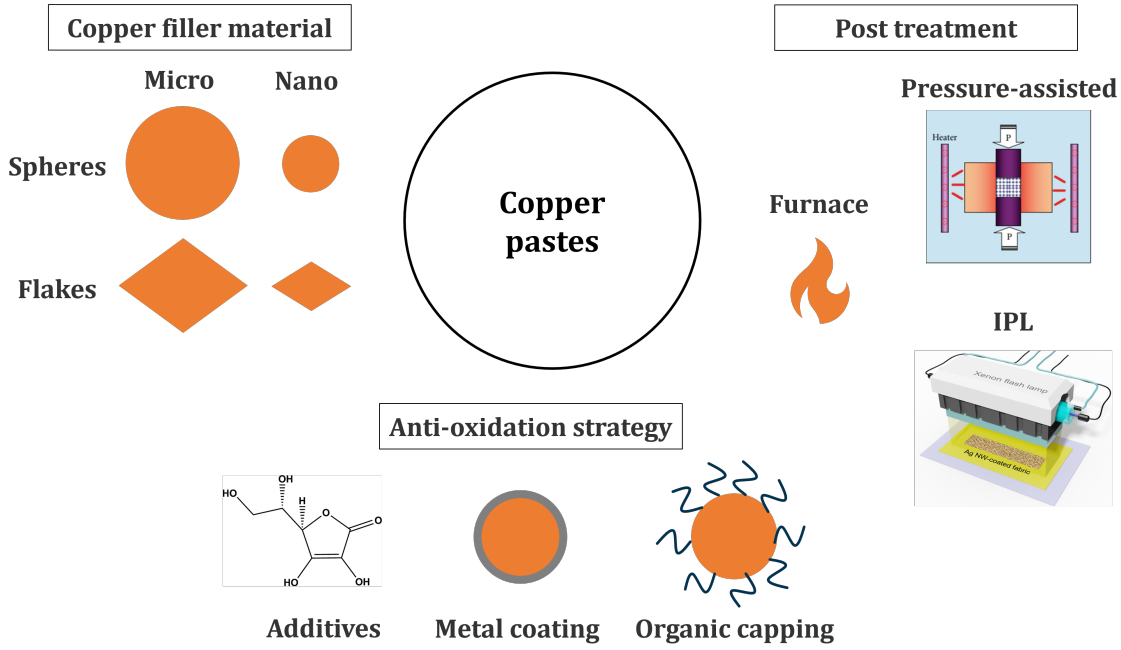

Figure 2.11: Common copper filler materials, anti-oxidation strategies, and sintering methods for copper-based pastes for printed electronics applications. The main copper filler materials are micro- and nano-sized spheres and flakes. As an anti-oxidation strategy acids are added to the pastes, particles are coated with metal shells, or particles are coated with small organic molecules or polymers. The post-treatment can be done in a furnace either in air, in vacuum, or in inert gas. Alternatively, the sintering process can be done under external pressure (adapted and reprinted with permission from [83]) or via alternative sintering strategies, such as Intensive Pulsed Light (IPL) sintering. Image from: "Rapid Pulsed Light Sintering of Silver Nanowires on Woven Polyester for personal thermal management with enhanced performance, durability and cost-effectiveness", by H. Hyun-Jun, Scientific Reports, Volume 8, Copyright (c) 2023. Available under Creative Commons Attribution 4.0 International (CC BY 4.0).

A commonly used polymer capping agent for copper nano- and microparticles is polyvinylpyrrolidone (PVP), which is also extensively used to stabilize silver particles. Cheng *et al.* synthesized copper nanoparticles with an average diameter of 140 nm coated with PVP [84]. They could achieve a resistivity of 17 $\mu\Omega \cdot$ cm at a temperature of 250 °C for 2 h under a mixed atmosphere of argon and hydrogen. Liu *et al.* pretreated 30 nm-diameter copper nanoparticles with formic acid, followed by a sintering treatment for 1 h in a nitrogen/hydrogen atmosphere at 260 °C and obtained a resistivity of 6.1 $\mu\Omega \cdot$ cm [85]. Yokuyama *et al.* investigated the influence of the PVP concentration during copper nanoparticle synthesis on the electrical performance of prints [86]. They made prints of 62 nm-sized particles and found that optimizing the PVP concentration resulted in more densely packed particle layers that adhered better to the substrate. They achieved a resistivity of 45 $\mu\Omega \cdot$ cm at 225 °C for 1 h under an argon and hydrogen flow.

Another common capping agent is citric acid. Sarwar *et al.* synthesized citrate-capped copper nanoparticles and made screen-printed traces that were treated at only 60 °C in ambient air [87]. The printed paste was sandwiched between layers of sodium alginate to further protect the printed traces from oxidation. It was said that the citrate was desorbed during the heat treatment, which was followed by the merging of the nanoparticles. As a result, they could obtain a resistivity of 74 μΩ · cm. Hong *et al.* used formate ions and dodecyl mercaptan to passivate the surface of commercial copper microflakes (80 nm thickness and 3 μm lateral size) [88]. They achieved a resistivity of 75 μΩ · cm after sintering for 10 min at 170 °C.

L-Ascorbic Acid (AA), also known as vitamin C, can be used as an environmentally friendly additive to suppress copper oxidation in conductive pastes [81, 82]. Gao *et al.* printed copper pastes of copper particles with diameters ranging from 1 to 500 nm on a copper substrate and placed a copper chip onto [81]. They sintered the paste to create a sintered joint and compared pastes with and without the addition of AA while sintering at a temperature of 350 °C in nitrogen. The AA increased bonding strength by reducing Cu_2O to Cu^0 and preventing further oxidation during sintering by scavenging oxygen. Paciono *et al.* also investigated the effect of AA on the oxidation of copper particles and found that it slows down oxidation by reducing copper ions into Cu^0 [82]. They used UV-visible and Electron Paramagnetic Resonance spectroscopy to support their claims.

It becomes evident from the examples above that despite the anti-oxidation strategies, the majority of copper-based pastes require a controlled sintering environment and high temperature to achieve good conductivities. In the next section, I discuss the state of the art in conductive pastes based on silver-coated copper particles. Such particles employ a thin coating of silver that prevents copper oxidation by forming a physical barrier between the oxygen and the copper core.

2.7 Silver-coated copper particles

Silver-coated copper particles can combine the low cost of copper with the oxidation resistance of silver. A thin silver coating blocks oxygen diffusion towards the copper core. The stability of silver-coated copper particles towards oxidation is limited by the stability of the silver coating. In ambient air, the coating remains stable for at least 6 months [71, 80]. Dewetting of the silver coating, which occurs at elevated temperatures, leads to exposure and oxidation of the underlying copper core. The dewetting of silver-coated copper particles is schematically illustrated in Figure 2.12 below.

Hai *et al.* found that dewetting occurred at a temperature of 200 °C for 2 μm-sized silver-coated copper particles with a 260 nm thick silver coating [89]. Yu *et al.* found an onset temperature of dewetting at 157 °C of 50 nm-sized silver-coated nanoparticles [90]. They used thermogravimetric analysis to show that the particles increased in mass due to oxidation above this temperature. Grouchko *et al.* observed dewetting at 250 °C for 40 nm-sized particles with a 2 nm-thick silver coating [91].

Silver-coated copper particles have been explored for their use in sinter bonding of chips in power electronics [92–96] and for printed electronics [90, 97–104]. Świerzy *et al.* developed a method to synthesize silver-coated copper particles with an average diameter of 1 μm and a silver shell thickness of 20 nm [97]. From these particles, they formulated pastes that were printed using a bar coating method. The printed layers rendered highly conductive after a heat treatment at 250 °C in nitrogen for 15 min. Dewetting at temperatures above 250 °C led to copper oxidation and decreasing conductivity as a consequence. In later

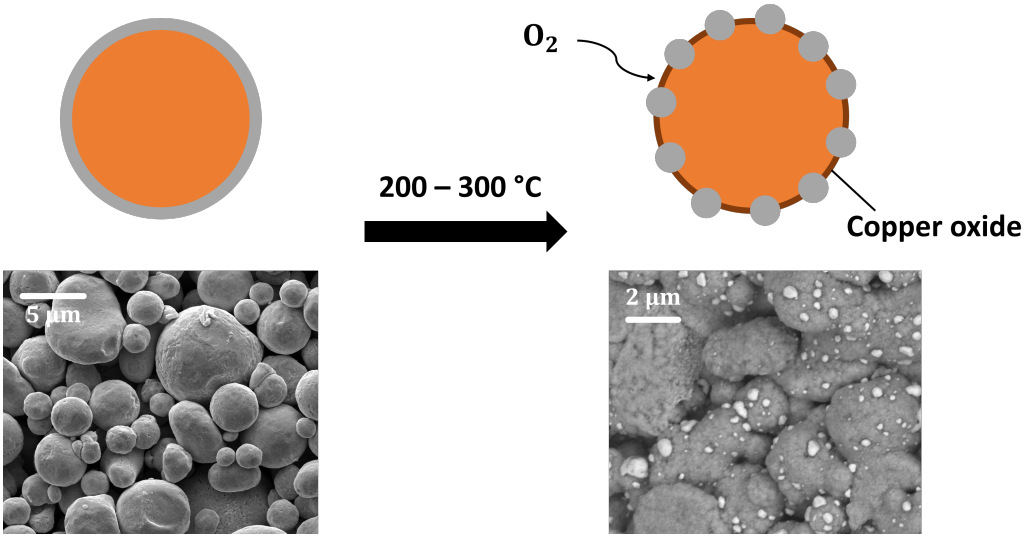

Figure 2.12: Dewetting of silver-coated copper particles at elevated temperatures. A schematic illustration and electron microscope images of particles before dewetting (on the left) and of particles after dewetting (on the right). The dewetting results in the oxidation of the exposed copper copper. The backscattered electron image (BSE) after dewetting shows the dewetted silver droplets with a bright contrast (BSE image on the right).

work, they added propionic, oxalic, citric, or oleic to the pastes and found that they chemically increased the conductivity of the prints [98]. Oleic acid was found to have the strongest enhancement effect. Kim *et al.* screen-printed a paste containing 450 nm-diameter silver-coated copper particles and achieved a resistivity at 200 °C in nitrogen for 1 h of 8.2 µΩ · cm [100]. Zhang *et al.* used an even lower temperature of 150 °C in nitrogen for 2 h using elliptic silver-coated nanoflakes and achieved 37.5 µΩ · cm [104].

The glass transition temperature (T_g) of most commonly used flexible substrates lies between 62 °C to 222 °C [7]. The post treatment temperature for flexible printed electronics should at least be kept below this T_g. Some of the examples above employ a heat treatment temperature of 200 °C or lower. Zhang *et al.* prepared their conductive traces on a flexible polyimide substrate. Nonetheless, the main drawback of all examples demonstrated so far is the fact that all heat treatments are done in nitrogen, in a vacuum, or under high pressure. This makes their use in printed electronics less attractive compared to pure silver particles, that can be sintered in ambient air conditions. In Chapter 6, I study the low-temperature sintering mechanism in ambient air of silver-coated copper particles and their use in printed conductors.

2.8 Sustainability of printed electronics

Reducing cost and increasing compatibility with flexible substrates are important to consider, but we cannot ignore the environmental aspect of manufacturing electronics by printing. Electronics continue to become more important in our society, evidently leading to more and more electronic waste. How do conventional PCB techniques compare to printing techniques when it comes to sustainability? Which aspects of printed electronics have the most environmental impacts? And most importantly, what can be done to minimize the environmental impact of printed electronics?

A straightforward way to reduce the environmental impact of printed electronics is to use a low-impact material as the substrate. Many researchers have investigated the use of paper or cardboard as a substrate for printing conductors [105–107]. Polymeric binders in conductive paste formulations can be replaced by low-impact alternatives. For example, Lv *et al.* demonstrated the fabrication of an elastomeric conductor for soft electronics applications using sustainable and recyclable vegetable oil as polymeric binder [108].

The largest sustainability gain can be achieved by changing the conductive filler material [2, 3, 109]. In the case of silver-based printed conductors, silver makes up for approximately 80 % of the global warming potential [110]. Carbon-based conductors could reduce the environmental impact, but their low conductivity limits their use. Alternatively, the silver content of printed conductors can be reduced to make them more sustainable.

Maximizing conductivity is equivalent to minimizing silver use in printed conductors. The higher the conductivity, the less silver is needed to achieve a certain conductance of the printed conductive trace. As I have discussed in Section 2.4, the sintering of the particles in the trace is crucial to maximize the conductivity of the printed trace.

A second, complementary strategy to reduce the amount of silver used in printed conductors is to recycle the used silver. Available commercial processes to recycle precious metals from electronics waste include mechanical processing, pyrometallurgical processing, and electrochemical separation processes [111–113]. Waste PCBs are shredded and the metallic fraction is magnetically separated. Pyrometallurgical processing involves heating the waste up to 500 °C to 2000 °C to burn out remaining organics and to create a molten mass of mixed metals. For further purification of the metals, electrochemical treatments are required. These processes are costly, require toxic reagents, require high temperatures, and release toxic fumes [113]. Furthermore, the recycled metal needs to be processed into a powder before it can be used in conductive pastes again. Some alternative recycling strategies of printed conductors that recycle the silver as powder have been presented in literature [22, 106].

Kang *et al.* printed reversible inkjet-printed gold nanoparticle traces, where the gold nanoparticles could be recovered after the lifetime [106]. They used a sinter-free hybrid nanoink, where the layers could be rendered conductive without sintering the printed nanoparticle traces. Kwon *et al.* recovered and reused metal powder from printed conductors without thermal treatment [22]. Silver flakes were recovered from a polycaprolactone matrix and used in new prints with similar electrical performance. These works demonstrate the possibility of recycling the silver powder from prints, nonetheless the absence of sintering results in resistivities of 3270 times (Kang *et al.*) and 3000 times (Kwon *et al.*) for that of bulk silver. Conventional sintering methods often result in dense metal layers, which would complicate the recovery of the powder. There are no studies up to date that combine the sintering of particles with a method to recycle them from the printed conductors after lifetime. In Chapter 3, I will introduce such a method for silver microparticles.

2.9 Research gaps addressed in this thesis

Whether a printed conductor is silver-, copper-, or carbon-based, they require high conductivity, low treatment temperatures, ambient air treatments, and the possibility of recycling the conductive filler material. In the previous sections, we have seen the main advances and remaining challenges for silver- and copper-based printed conductors. The main challenge remains to sinter particles at low temperatures to achieve high conductivities. Copper-based conductors require anti-oxidation strategies to prevent copper oxidation which lowers the conductivity. Lastly, recycling strategies for the metal particles are required to reduce the environmental impact of printed electronics. This thesis aims to contribute to the current state of the art:

Gap 1: Low-temperature sintering mechanisms of silver microparticles. In Section 2.5, we have seen that high conductivities have been achieved through sintering of silver microparticle traces at low temperatures (200 °C and lower) [12, 13, 63]. The formation of nanoparticles during sintering of microparticles has been observed and suggested to play a role in the low temperature sintering mechanism. However, there is no agreement on the sintering mechanism, nor is it clear how nanoparticles would aid sintering. In Chapter 3 of this thesis, I will present a mechanism that both explains the low temperature sintering of silver microparticles and the formation of nanoparticles.

Gap 2: The best of two worlds: Sintering and recycling. Recycling and reusing the conductive filler is crucial for making printed electronics more sustainable. So far, the potential of recycling and reusing metal particles from printed conductors has been demonstrated in the works of Kang *et al.* and Kwon *et al.* [22, 106]. However, achieved conductivities are not yet competing with sintered conductors. In Chapter 3, I will discuss how to combine sintering and recycling to obtain highly conductive, recyclable printed conductors. The introduced recycling method is used to demonstrate the recycling of the metal powders in Chapters 4 and 6.

Gap 3: Flakes versus spheres. Silver flakes and spheres have been discussed in the literature for their use in printed electronics, including differences in sintering kinetics and achieved conductivities. Flakes are presented as the more suitable option for obtaining high conductivities at a low temperature. Nonetheless, it is not trivial whether this is true for higher sintering temperatures as well. Neither has the recyclability of sintered flakes versus sintered spheres been studied. In Chapter 4, flakes and spheres were sintered at temperatures ranging from 110 °C to 300 °C, and their electrical conductivity at each temperature were compared. Mildly and strongly sintered flakes and spheres were recycled and their recovery percentage was compared.

Gap 4: Copper-based printed conductors. In Chapter 5, I will discuss the sintering of polymer-capped copper microparticles. Pastes were made containing 1.5 and 2.5 µm particles, ethylene glycol, and L-Ascorbic acid (AA). The polymer capping served to protect the particle surface from oxygen and the AA to scavenge oxygen during sintering through its own oxidation. The pastes were printed and sintered at temperatures ranging from 200 °C to 400 °C in ambient air and in a vacuum. In Chapter 6, I studied the low temperature sintering in ambient air and recycling of silver-coated copper spheres and flakes.

3 Recyclability-by-design of Printed Electronics by Low-Temperature Sintering of Silver Microparticles

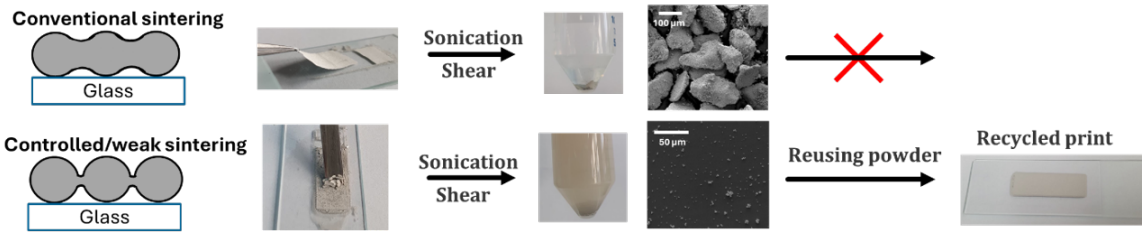

This chapter is based on the content of the article:
D. van Impelen, L. González-García, T. Kraus, *Recyclability-by-design of Printed Electronics by Low-Temperature Sintering of Silver Microparticles*, Advanced Electronic Materials 2024.
https://doi.org/10.1002/aelm.202400533

The article is licensed under a Creative Commons CC BY license. Content is reused with permission of the authors.

3.1 Abstract

A low-temperature sintering mechanism of silver microparticles is established and used to enable the design-for-recycling of printed electronics. We study the formation of necks during the initial phase sintering of precipitated and atomized silver microparticles. Temperature- and time-dependent in-situ analyses indicate the existence of a mobile silver species that provides efficient mass transport. The activation energy of neck formation identifies silver ion formation as the rate-limiting step of low-temperature silver sintering. We demonstrate that resistivities of 271 times that of bulk silver can be attained after 40 min at 150 °C. Low-temperature sintering not only reduces the energy required during thermal treatment, but it yields layers that are suitable for recycling, too. The resulting layers have conductive necks that are mechanically weak enough to be broken during recycling. We redispersed printed layers and reused the recycled silver powder without loss of the electrical performance in new prints. Their conductivities were industrially relevant, which makes this recyclability-by-design approach promising for manufacturing more sustainable printed electronics.

3.2 Introduction

Metal-based pastes are the current industry standard for conductive adhesives, conductive paints, and screen-printable conductive pastes. Their conductivity stems from metal nano- or microparticles, usually with quasi-spherical or flake-like shapes [4, 7, 8]. Polymers and solvents are added to create pastes, tune their viscosity for printing, protect the metal during further processing, and increase the adhesion and mechanical robustness of the final printed structure.

Electronics can be printed using metal-based pastes [4, 5, 7, 8] at high production rates [7, 8], low costs [4, 7, 8], good sustainability [2, 3], and for flexible electronic applications [114, 115]. The printed pastes form traces in which the metal particles conduct electronically. High conductivities usually form only after heat treatments, which increases energy requirements and limits the compatibility with flexible substrates [7]. This has motivated research in pastes that reach high conductivities at low temperatures.

Silver is an interesting material to this end. The high intrinsic conductivity of silver ($\rho_{Ag} = 1.59\,\mu\Omega\,\mathrm{cm}$) [116], its conductive oxide [117], and its stability at elevated temperatures [118, 119] make silver the standard metal in conductive metal pastes, albeit at considerable ecological and economical costs. The mining, refining, and processing of silver are resource-intensive processes. Silver has an embodied energy of $15\,\mathrm{MJ\,kg^{-1}}$ [14], and a CO_2 equivalent emission of 25 000 kg [14]. Silver prices have been above 10 USD per ounce (353 USD per kilogram) since the year 2005. There are thus considerable economic and ecological incentives to reduce the required amount of silver and to recover silver from printed electronics.

In this contribution, we study how to minimize the amount of silver used in printed conductors and the required temperatures simultaneously. We investigate whether the resulting prints can be recycled and show that while trade-offs exist between silver use, temperature, and recyclability, industrially relevant performances can be reached below 160 °C while retaining recyclability. The following sections discuss how classical sinter theory and current research on silver particle sintering contributed to this goal.

The conductivity of printed, untreated leads is initially dominated by contact resistances between the metal particles [43, 44]. Thermal annealing induces the formation of metallic sinter necks between the

particles by surface and bulk diffusion, which reduces the contact resistances and therefore increases the conductivity of the leads [9, 38]. Classical sintering theory distinguishes initial, intermediate, and final stage sintering that leads from a powder compact to a dense material [50]. Particle contacts in the original powder compact are dominated by weak Van der Waals interactions. Theory predicts that the particle contacts are converted into grain boundaries at approximately 75 % of the metal's melting temperature, the initial stage of sintering [51]. Surface diffusion, grain boundary diffusion, lattice diffusion, and evaporation-condensation-controlled mass transport then contribute to neck growth [120]. The initially high curvature of the saddle-like necks reduces and their cross-section increases. The initial stage ends when the neck diameter reaches one-third of the particle size or when the powder compact has lost more than 3 % of its volume [9, 121]. In the subsequent intermediate stage, the particles lose their individual nature and merge. Cylindrical pores are formed, and grain growth starts. The cylindrical pores shrink until they collapse at a relative density of approximately 90 % and leave spherical pores. The final stage of sintering then removes the remaining pores [9].

Research of the past decade has shown that silver nanoparticles with diameters below 200 nm fuse at a much lower temperatures, which has been exploited to create highly conductive silver prints at temperatures below 200 °C [7, 8, 122]. Such particles contain large fractions of organic stabilizers. They fuse when these stabilizers are removed from the surface, but it is difficult to use them in thicker layers without cracking. Furthermore, the synthesis route of nanoparticles is typically complex, which makes them less attractive for industrial applications.

Most commercial conductive pastes are based on silver microparticles (AgμP) that contain fewer surfactants, are cheaper to produce than nanoparticles, and are available at scale. AgμP are produced either by chemical reduction by "precipitation" or from a metal melt by "atomization" [13, 123, 124]. Precipitated nano- and microparticles carry an organic surfactant layer that is usually electrically insulating [125]. Atomization uses a stream of liquid metal that breaks into droplets in a gas or liquid jet, followed by the solidification of a powder of metal microparticles [126], and does not require surfactants.

Standard theory implies that temperatures of approximately 721 °C (75 % of the melting temperature) are required to create necks between such AgμP [51]. If the grain size of the microparticles is smaller than 100 nm, a process called triple-grain boundary diffusion dominates mass transport during neck formation [127, 128]. This mechanism enables sintering already at 20 % of the melting temperature, 240 °C for silver [51]. However, open literature shows that sinter necks already form at even lower temperatures: 1.3 µm diameter AgμP formed necks already at 150 °C after 30 min as confirmed with Scanning Electron Microscope (SEM) imaging [11, 12]. Guo *et al.*. explained this observation with nanoscale surface features that enhance surface diffusion, enable sintering, and reduce bulk resistivity to $1.7 \cdot \rho_{Ag}$ [12]. Zhan *et al.* treated silver micro flakes (0.5 µm to 1.5 µm, thickness 30 nm) with $NaNO_3$ and succinic acid and found that 140 °C after 30 min led to $67.5 \cdot \rho_{Ag}$ [11]. They suggested that $NaNO_3$ and succinic acid remove surfactants, etch silver, and aid sintering.

Several groups report the in-situ formation of silver nanoparticles (AgNP) during low-temperature sintering of AgμP [13, 62, 63]. However, there is no consensus on the origin of the AgNP. Yeom *et al.* claimed that silver micro flakes (average diameter 8 µm, thickness 260 nm) formed AgNP at 250 °C due to the release of microstrains [62]. Later, the same group studied a bimodal silver micro powder (quasi-spherical with average diameters of 0.4 and 2.5 µm) at 175 °C and attributed the formation of AgNP to a

complex of polyvinylpyrrolidone (PVP) on the particle surfaces with silver ions [13]. These ions are said to be reduced by ethylene glycol to form AgNP, which was used as a solvent in the paste formulations. Matsuhisa *et al.* sintered silver flakes ($\sim$ 5 µm diameter) at 140 °C inside a fluoroelastomer matrix and found AgNP [63] at a density that was increased when adding the fluorine-based surfactant S-386 to the matrix. The authors explained AgNP formation with the diffusion of Ag^+ into the polymer, followed by reduction by the surfactant. The link between low-temperature sintering, neck formation mechanisms, and nanoparticle formation remains unclear in all of these studies.

Low-temperature sintering can lower the cost of printed conductors and make it possible to temperature-sensitive flexible substrates. A less obvious consequence that has not been addressed in the literature is the recyclability of low-temperature sintered leads. We propose that redispersion and reuse of used silver particles is possible if the sinter necks are weak. Kwon *et al.* demonstrated the recovery and reuse of metal powder from printed conductors without thermal treatment [22]. Silver flakes were recovered from a polycaprolactone matrix and used in new prints with similar electrical performance. However, such untreated films have relatively high bulk resistivities, equivalent to $3000 \cdot \rho_{Ag}$ in the case of Kwon *et al.*. This has to be compensated with thicker films and larger silver amounts, which limits economic and ecological benefits. To our knowledge, there are no reports on recycling and reusing sintered silver particles from printed conductors.

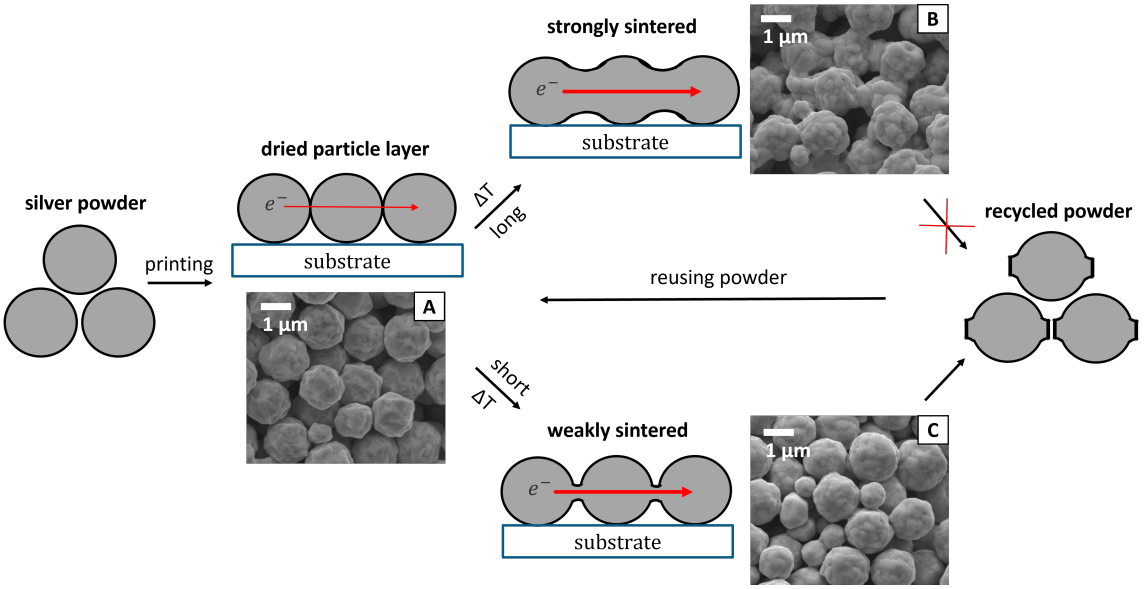

Figure 3.1: Low-temperature sintering of conductive printed silver films *designed for recycling*. Silver micro powders (micrograph A) that are sintered at 200 °C form large sinter necks (B) that prevent re-dispersion. (C) Low-temperature sintering leads to thin necks with a good electrical conductivity that can be fractured for recovery.

In this work, we demonstrate the formation of a printed silver lead with a conductivity that is on the order of currently used industrial materials. To this end, we combine a low-temperature sintering treatment of AgμP with a strategy to recycle and reuse the silver particles for new prints. The AgμP are first printed, sintered at a low temperature, and then redispersed to recover the sintered AgμP in the "recyclability-by-design" approach shown in Figure 3.1. The strategy is based on targeting to create sinter necks that are mechanically weak and can be broken up again, but still lead to a significant conductivity increase of the

printed conductor. Furthermore, we demonstrate how these recycled particles can be reused for printing a new generation of printed conductors. Additionally, we propose a low-temperature sintering mechanism based on a mobile silver ion concentration that explains both low-temperature sintering and the emergence of silver nanoparticles. We study the neck formation between AgμP experimentally and focus on the role of organic compounds on the particle surfaces. Ligand-containing, chemically precipitated- are compared with ligand-free atomized AgμP in screen-printed particle films. We analyze the changes in conductivity and microstructure during heat treatments ex-situ and in-situ as a function of particle origin, temperature, and time.

3.3 Results and discussion

3.3.1 Effective silver use through low-T sintering

The bulk resistivities of freshly printed, silver-based conductors are below the bulk resistivity of pure silver and dominated by the resistances at interfaces between particles [7]. Heat treatments reduce the contact resistances such that conductivity increases. Porosity remains, however, so that the limiting $\rho_{Ag} = 1.59\,\mu\Omega\,\mathrm{cm}$ [129] will not usually be reached.

Bulk resistivities are commonly determined by first measuring a sheet resistance

$$R_{sh} = \frac{\pi}{\ln(2)} \cdot \frac{\Delta V}{I}, \tag{3.1}$$

where ΔV and I are the potential difference and current between two points on a thin film with constant thickness. Layers with equal bulk resistivities can have different porosities and thus, contain different amounts of silver. In the following, we use a mass-normalized sheet resistance,

$$R_{m/sh} = m * R_{sh}, \tag{3.2}$$

that contains m, the mass of silver in the printed layer, and provides a material property that is independent of layer thickness (in contrast to sheet resistance). A dense layer of bulk silver has the lowest possible value of $R_{m/sh,Ag} = 0.05\ \frac{\mathrm{m\Omega}}{\mathrm{sq}} \cdot \mathrm{g}$. Minimizing $R_{m/sh}$ is equivalent to minimizing the electrical resistance at a given silver content. Our aim in this contribution is to minimize $R_{m/sh}$ while retaining recyclability.

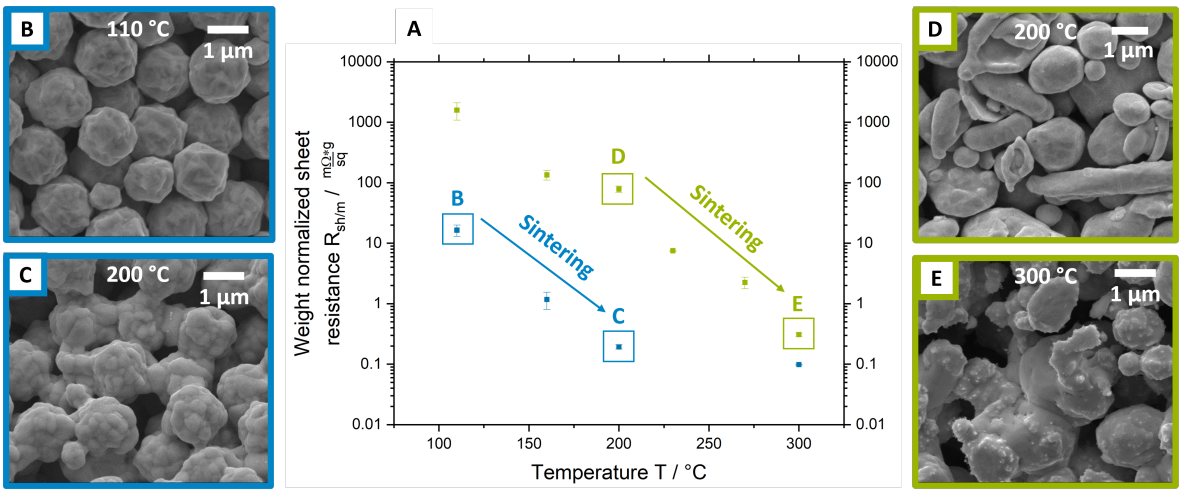

Figure 3.2: Effect of heat treatment on microstructure and conductivity of printed silver particle layers. (A) Mass-weighted sheet resistance $R_{m/sh}$ after 30 °C at temperature T. Arrows indicate the onset temperatures for precipitated (blue) and atomized (green) particles. Each point represents the average of three samples, error bars indicate +/- one standard deviation. (B) Top view SEM image of a precipitated particle layer treated at 110 °C and (C) at 200 °C. (D) Atomized particle layer treated at 200 °C and (E) at 300 °C.

We prepared pastes containing 1.5 µm precipitated (P-) or 1.7 µm atomized silver particles (A-AgμP). P-AgμP had rough, A-AgμP had smooth surfaces (see Figure S1 of the Supporting Information). Thermogravimetric analysis indicated that P-AgμP contained 0.4 wt-% of organic surfactants, while A-AgμP

did not contain any measurable surfactant (Figure S2 of the Supporting Information). Cross-sections of printed lines prepared with a Focused Ion Beam (FIB, cf. experimental section) revealed nanoporous cores for P-AgμP and dense cores for the A-AgμP (Figure S3 of the Supporting Information). X-ray Diffraction (XRD) indicated grain sizes of 36.7 nm for P-AgμP and 20.4 nm for A-AgμP (Figure S4 of the Supporting Information).

Lines with an average thickness of 21.5 µm and 37.5 µm of precipitated or atomized particles were printed on glass slides and treated at different temperatures between $110\,^{\circ}$C to $300\,^{\circ}$C for 30 min (see Figure 3.2A). The degree of sintering was assessed using Scanning Electron Microscopy (SEM) and electrical characterization. In addition, the crystal size for both particle types treated at different temperatures was estimated using XRD.

Figure 3.2B shows that printed lines of precipitated particles treated at $110\,^{\circ}$C contained separated particles without visible sinter necks. We estimate that SEM could detect any necks with diameters above 50 nm. The $R_{m/sh}$ of these lines were 2 orders of magnitude above that of bulk silver and dominated by particle-particle contact resistances [130]. Figure 3.2C shows sinter necks formed in printed lines of precipitated particles at $200\,^{\circ}$C that reduced $R_{m/sh}$ to approximately $4R_{m/sh,Ag}$.

Atomized particles did not yet form sinter necks at $200\,^{\circ}$C, (see Figure 3.2D), which explains their $R_{m/sh} = 78.5\,\frac{\mathrm{m\Omega}}{\mathrm{sq}} \cdot \mathrm{g}$, 3 orders of magnitude above $R_{m/sh,Ag}$ (Figure 3.2A). Sinter necks did form at $300\,^{\circ}$C (Figure 3.2E), and reduce $R_{m/sh}$ to $8R_{m/sh,Ag}$ (Figure 3.2A).

The change in resistance, $\Delta R_{m/sh}$, during 30 min sintering depended on temperature. It dropped between 110 and $200\,^{\circ}$C for printed P-AgμP lines and between 200 and $300\,^{\circ}$C for printed lines containing A-AgμP (see Figure 3.2A). Lower temperatures did not change $R_{m/sh}$, higher temperatures led to plateau values of $R_{m/sh}$. It appears that $R_{m/sh}$ first decreases due to neck formation between the particles, followed by further decreasing due to the growth of the sinter necks. An alternative hypothesis would be to assume that not all necks are formed at once so that $R_{m/sh}$ drops as the number of necks increases until all A-AgμP have necks connecting them to their neighbors, and $R_{m/sh}$ reaches a plateau value.

X-Ray Diffraction (XRD) revealed that crystal growth started at $110\,^{\circ}$C for P-AgμP and at $160\,^{\circ}$C for A-AgμP (Figure S5 of the Supporting Information). The onset of crystal growth at a lower temperature for P-AgμP is consistent with the decrease of $R_{m/sh}$ that already started at $110\,^{\circ}$C for P-AgμP.

The low temperature sintering of 1 µm-diameter precipitated particles was studied in pastes formulated with industry-standard polymers and additives for improved printability and adhesion to the substrate, too. The results were comparable to those shown above (details can be found in Section 6 of the Supporting Information).

The observation that P-AgμP sintering occurs at lower temperatures ($110 - 200\,^{\circ}$C) compared to A-AgμP ($200 - 300\,^{\circ}$C), demands a closer look at the sintering mechanism at play. In the next section, we indirectly followed the evolution of sintering by in-situ tracking of the conductivity of prints during heat treatments. Based on those results and the results in this section we then formulate a hypothesis explaining both the observed differences between P-AgμP and A-AgμP, and the general observation that sintering of these particles already occurs at such remarkably low temperatures.

3.3.2 Low-T sinter mechanism

We followed the evolution of the sinter necks during the heat treatment indirectly by observing electrical conductivity in-situ. Samples made from P-AgμP or A-AgμP were placed on a hotplate, heated to maximal temperatures of 130 to 160 °C (P-AgμP) or 250 to 350 °C (A-AgμP), and held there for at least 90 min. The electrical resistance was monitored (cf. experimental section). To save space we show only one trace per temperature, nonetheless all measured samples (three or more) can be found in Figure S7 (P-AgμP) and Figure S8 (A-AgμP) of the Supporting Information. The 2-point contacting scheme used in the setup shown in Figure 3.3 was validated by comparison with a 4-point probe measurement of 1.5 µm precipitated particles at 160 °C shown in Figure S9 of the Supporting Information. Large sample-to-sample variations of dried, but not sintered, prints were confirmed with 4-point measurements. The average $R_{m/sh}$ of 9 samples dried at 60 °C in vacuum for 2 h was 31 $\frac{\text{m}\Omega}{\text{sq}} \cdot \text{g}$ with a standard deviation of 20 $\frac{\text{m}\Omega}{\text{sq}} \cdot \text{g}$. Contact resistances also contributed to the variations of the initial resistances observed in Figure 3.3A but did not affect the onset times of sintering that are analyzed here.

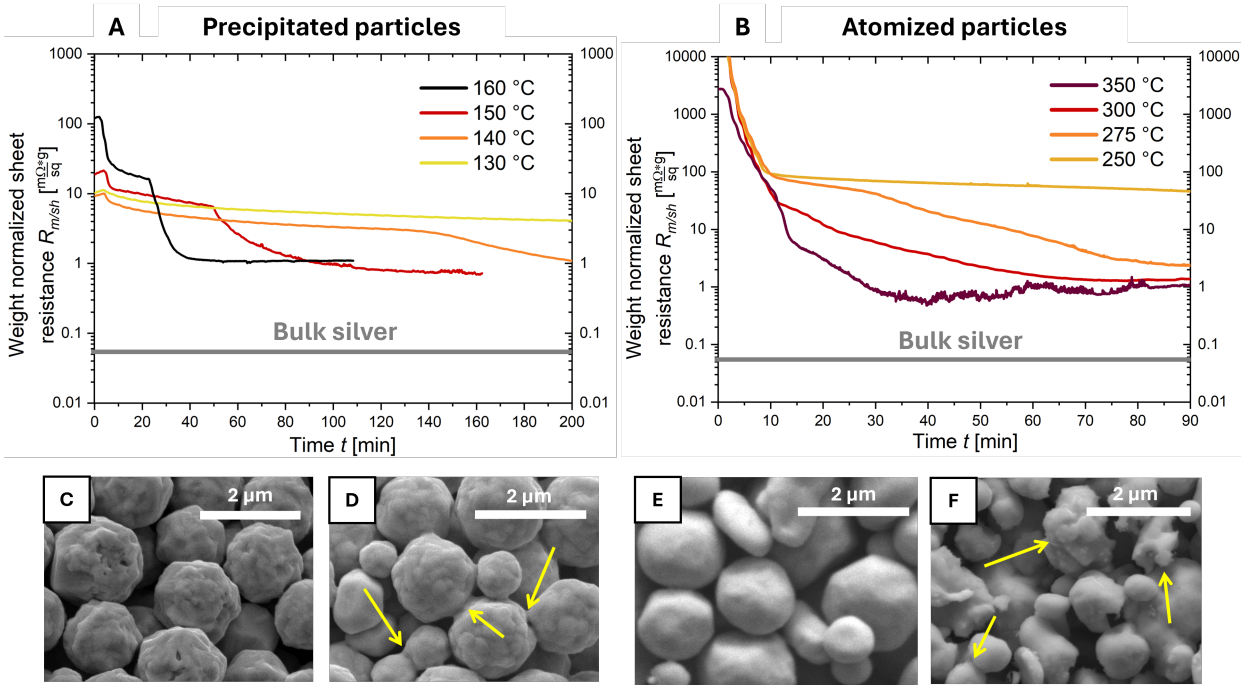

Figure 3.3: Change in resistance $R_{m/sh}$ and neck formation of layers formed from P-AgμP and A-AgμP. Layers were heated to T at a rate of 28 °C min^{-1} and kept for at least 90 min. (A) Resistance evolution for P-AgμP and (B) A-AgμP. (C-F) Scanning electron micrographs of (C) P-AgμP layers treated at 130 °C and (D) 160 °C; (E-F) A-AgμP layers treated at (E) 250 °C and (F) 275 °C. Yellow arrows indicate sinter necks.

Figure 3.3A shows the time-dependent $R_{m/sh}$ and SEM images of P-AgμP layers. Sinter necks became visible only above 130 °C (Figure 3.3C). We attribute the drop in electrical resistance below 130 °C during the first 10 min to the removal of residual Ethylene Glycol (EG) that are visible in SEM cross-sections (see Figure S10 in the Supporting Information). The dry films reached a plateau $R_{m/sh} = 10\ \frac{\text{m}\Omega}{\text{sq}} \cdot \text{g}$ that did not decrease when heating longer.

Temperatures above 130 °C consistently led to a second, remarkably sharp drop in $R_{m/sh}$. Its onset times decreased with increasing temperature (Figure 3.3A, Figure S11 of the Supporting Information).

Given the changes in electrical conductivity and the evidence of neck formation, we conclude that sinter necks formed through processes with a finite activation energy that require a time t_{onset} and a minimal temperature T_{onset}. They reduced the overall resistance drastically as soon as percolating electrical paths had formed.

Printed lines of A-AgμP exhibited the same, solvent-induced initial drop as P-AgμP. Layers treated at up to $250\,^{\circ}\text{C}$ reached plateau $R_{m/sh}$, suggesting an absence of sinter necks that was confirmed by SEM (Figure 3.3E). Higher temperatures caused drops after $15-90\,\text{min}$ that were less sharp than for P-AgμP and correlated with the formation of the necks that are visible in Figure 3.3F.

Neck formation within $30\,\text{min}$ at $160\,^{\circ}\text{C}$ for P-AgμP and $300\,^{\circ}\text{C}$ for A-AgμP exclude classical sintering mechanisms [50, 51]. Our observations are consistent with other reports on neck formation between AgμP at temperatures of 140 to $250\,^{\circ}\text{C}$[11–13, 62]. In the following, we analyze our results and propose a non-classical sintering mechanism for AgμP.

The mass-normalized sheet resistance $R_{m/sh}$ of AgμP layers sharply dropped at t_{onset} with rates $r_R = \partial R_{m/sh}/\partial T\big|_{t_{\text{onset}}}$ that depended on temperature. Decreasing T increased t_{onset} and reduced r_R. Let us assume that this temperature dependence is related to the activation energy of one step in the mechanism. We used a standard Arrhenius analysis to estimate the relevant activation energy as $140\,\text{kJ mol}^{-1}$ [131]. This is below the activation energy $170\,\text{kJ mol}^{-1}$ of silver-self diffusion at temperatures below $500\,^{\circ}\text{C}$ [132].

Low-temperature neck formation apparently involves a different mass transfer mechanism that brings silver to the particle-particle junction. We propose the existence of mobile silver species with transport mechanisms that have lower activation energies than those in conventional sintering. In the following, we will refer to the mobile silver species as

ions, without limiting the generality of the model. Mobile species may be complexed ions, atoms moving in a different phase, or clusters, for example. Given the oxidative dissolution of silver that spontaneously occurs at standard conditions [133, 134], silver ions are a likely candidate.

The existence of silver ions in printed AgμP films was confirmed by experiments that we performed on the rate of silver ion release from P-AgμP and A-AgμP. The powders were dispersed in isopropanol (IPA) at a volume fraction of 0.001 (cf. experimental section), kept at room temperature, and the ion content of the supernatant was measured after $12\,\text{h}$ using ICP-OES. The P-AgμP resulted in a released mass fraction of silver in the supernatant of $445\,\text{ppm}$, A-AgμP only $1.4\,\text{ppm}$. The difference is likely connected to the surfactants that are present on P-AgμP, complex silver ions, enhance release, and form a surface layer with increased silver content [13, 63].

Compact, atomized silver particles have clearly defined surfaces; porous, precipitated particles present additional internal interfaces. To contribute to sintering, silver has to move to junctions. Literature suggests that the chemical nature of the silver surface affects this transport. Glover *et al.* found that humidity strongly affected the transport of silver ions on the surface and hypothesized that a thin liquid film became a transport medium of generated ions [134]. Other authors suggested organic ligands as a possible medium [62, 63].

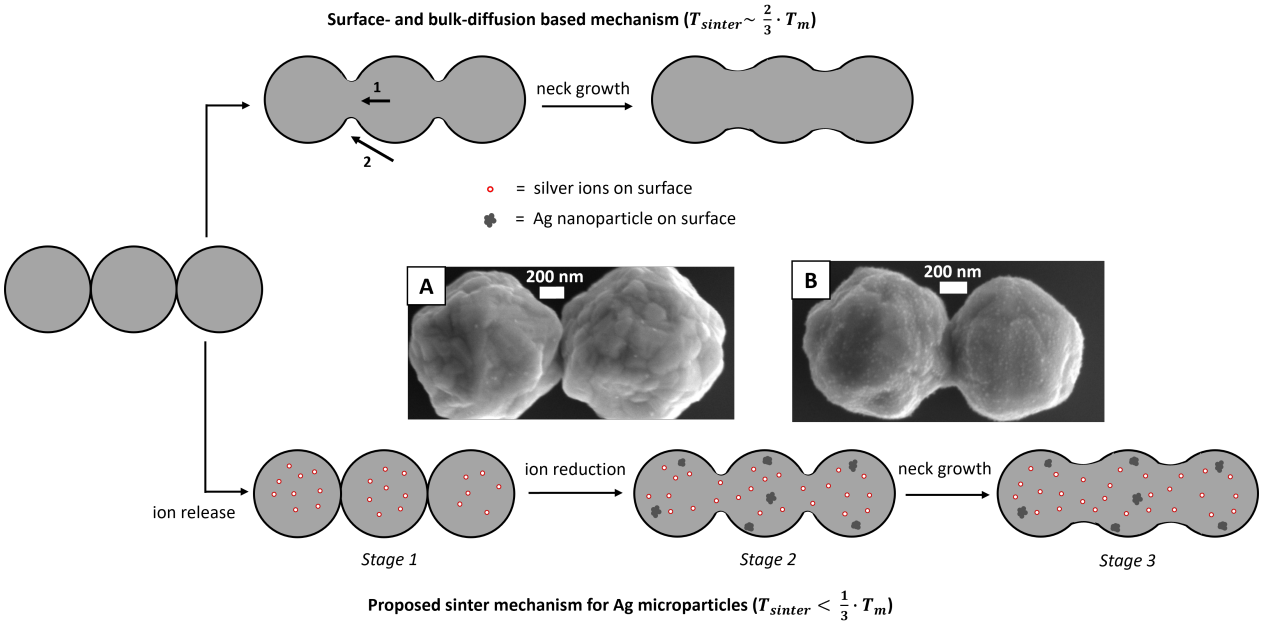

Figure 3.4: Classical surface- and bulk-diffusion (top) and low-temperature (bottom) sinter mechanisms for AgμP. (1) Bulk and (2) surface diffusion are the transport mechanisms that cause classical sintering. Silver ions (red open circles) enable low-temperature sintering and cause nanoparticle formation (bottom).

Figure 3.4 illustrates our proposed sequence of low-temperature sintering with silver ions. First, ions are released from the metal surface at a rate that increases with temperature (stage 1). They diffuse more rapidly than Ag^0, which enables larger transport rates than in classical sintering, but they must be reduced, which involves nucleation. Let us imagine the mobile species in its matrix as a solution. A reaction into a metallic solid may then occur via homogeneous or heterogeneous nucleation. Homogeneous nucleation occurs when the concentration reaches a critical supersaturation [135,136] that should cause the formation of metal particles.

Homogeneous silver nucleation has been observed by us (see Figure S12 in the Supporting Information) and reported in the literature on low-temperature sintering that report nanoparticles on the surface of the microparticles [13, 62, 63]. Nanoparticle formation has, in fact, been used as an explanation for low-temperature sintering of silver microparticles. We suggest a more indirect connection: it is difficult to believe that the nanoparticles preferentially form between particles, and unclear how they could be converted into bulk silver necks. Instead, we propose that homogeneous nucleation is a side effect of the accumulation of silver ions, but not the origin of the necks.

We propose that neck formation occurs through heterogeneous nucleation at lower concentrations and deposits Ag^0 on existing metal surfaces. Silver ions form at all interfaces, increasing the local silver concentrations depending on microscale geometry. Small gaps between adjacent silver particles lead to increased local concentrations and heterogeneous nucleation that forms an incipient neck. At positions where heterogeneous nucleation is not possible (e.g. at the outer edge of an organic surfactant shell), concentration rises until homogeneous nucleation causes the formation of nanoparticles.

The overall mechanism proposed for low-temperature neck formation is illustrated in Figure 3.4. Ions are released in stage 1 and start diffusing. When critical concentrations are reached, nanoparticles form

through homogeneous nucleation, or necks through heterogeneous nucleation, depending on the geometry (Figure 3.4, stage 2). Both necks and nanoparticles further grow through heterogeneous nucleation (Figure 3.4, stage 3).

Increasing temperature increases the rate of ion formation exponentially. The rate of the local silver ion concentration increase is thus a strong function of temperature. This explains the reduction of t_{onset} from 140 to 20 min when increasing temperature from 140 to 160 °C. In contrast, ideal diffusivities are linear in temperature, so the increase of the ion diffusivity can hardly explain the acceleration. A chemical reaction with an exponential Arrhenius-type rate dependency is consistent with the observations. Note, however, that the change in t_{onset} would be difficult to explain when assuming that the reduction reaction is the kinetically limiting step: if the ion concentration was sufficient, nucleation should not have any onset time. We conclude that silver ion formation is the limiting step of low-temperature sintering.

We never found nanoparticles, neck formation, or conductivity increases when storing the printed particle layers at ambient conditions. Oxidative dissolution of silver in an adsorbed water layer already can occur at room temperature [133, 134], but its rate is low. In the case of P-AgμP, it took 12 hours to dissolve $0.044\,\%$ of the original silver mass into isopropanol at room temperature. Liu *et al.* studied ion release kinetics of silver nanoparticles with a diameter ranging from 2 to 8 nm, and they observed a 4-fold increase of release rates when increasing the temperature from 4 to $37\,^{\circ}$C [137]. It appears that the formation of mobile species at room temperature is too slow for nucleation to occur at relevant time scales.

The sharp, temperature-dependent drops of $R_{m/sh}$ support our model. Ions are released from the surface and reduced in the matrix at an exponentially temperature-dependent rate. The onset time t_{onset} represents the moment at which the silver ion concentration exceeds the critical concentration of heterogeneous nucleation. The increase of r_R with T is an obvious consequence of the larger flux of ions.

Our model explains the difference in T_{onset} between P-AgμP ($140\,^{\circ}$C) and A-AgμP ($275\,^{\circ}$C), too. The ion formation rate for P-AgμP is larger due to the presence of surfactants and the larger specific silver surface of the P-AgμP. The concentration required for nucleation is thus reached at lower t_{onset} than for A-AgμP. We cannot exclude contributions of triple-grain boundary diffusion [51], but the observed sintering onset temperature of $140\,^{\circ}$C is too low to be explained by it alone.

3.3.3 Recycling weakly sintered silver

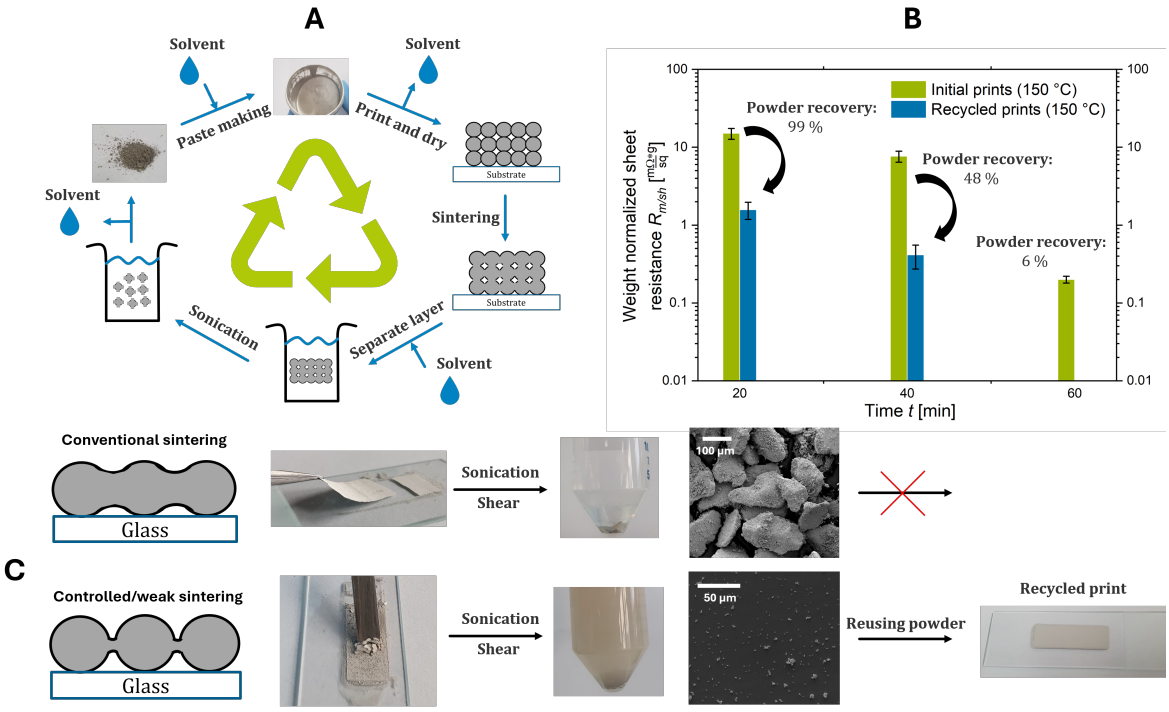

Figure 3.5: Recycling of low-T sintered silver layers. (A) Preparation, printing, and sintering of new materials and recycling of the printed layer. (B) $R_{m/sh}$ and recovery rates of silver layers treated at 150 °C for 20 , 40 and 60 minutes. Recovery became impossible after 60 min. (C) illustrates the strategy of weakly sintering the particles, breaking up weak sinter necks, and recycling and reusing silver powder for new prints.

Low-T sintering allowed us to reach resistivities of $271 \cdot \rho_{Ag}$ ($150 \cdot R_{m/sh,Ag}$) already at 150 °C for P-AgμP. This caused sinter necks with diameters below 0.8 µm. We show that they enable direct recycling of the silver as a powder, as illustrated in Figure 3.5A.

Prints containing P-AgμP were treated for 20 , 40 , and 60 min at a temperature of 150 °C and $R_{m/sh}$ was determined ('initial' in Figure 3.5B). The prints were removed from their glass substrates mechanically, submerged in IPA, ultrasonicated, and redispersed using shear to create particle suspensions (see Figure 3.5A). The particles were then separated from the solvent by centrifugation and dried. The silver fraction that could not be redispersed remained at the bottom of the centrifugation tube and was separated by decanting, dried, weighed, and recorded as a loss. The recycled powder was used again in formulating a new paste, and the cycle repeated.

Powder could be recovered from all prints, but the loss fraction increased with sintering time. Sintering at 150 °C for 20 min enabled recycling 99 % of the powder, compared to only 48 % after 40 min and 6 % after 60 min. SEM images of the redispersed and the lost fractions are shown in Figure S13 of the Supporting Information. Electron microscopy showed large, sintered agglomerates that were not redispersed by ultrasonication and caused the loss.

The size distributions of the recovered silver particles were comparable to the original powder; we successfully used them to formulate pastes and printed them again (Figure S14 of the Supporting Infor-

mation). The height profiles of recycled prints were comparable to the initial prints (Figure S15 of the Supporting Information). Heat treatments at $150\,^{\circ}\mathrm{C}$ for 20 , 40 , or $60\,\mathrm{min}$ led to the layers named 'recycled prints' in Figure 3.5B. Interestingly, recycled prints had lower $R_{m/sh}$ than fresh prints for identical heat treatments. Recycled powders contained sintered agglomerates that apparently decreased $R_{m/sh}$ by reducing the number of interfaces throughout the printed structure. We monitored the evolution of $R_{m/sh}$ during a $150\,^{\circ}\mathrm{C}$ treatment of a recycled print that contained P-AgμP already sintered at $150\,^{\circ}\mathrm{C}$ for $20\,\mathrm{min}$. The evolution of $R_{m/sh}$ was exactly as for fresh particles described above, with the same t_{onset} of $50\,\mathrm{min}$, only shifted to lower starting values (see Figure S16 in the Supporting Information). Prints made out of powders that were more strongly sintered had different shapes without a clear t_{onset}.

In summary, we demonstrated that weak sintering of silver microparticles for $20\,\mathrm{min}$ at $150\,^{\circ}\mathrm{C}$ reduced $R_{m/sh}$ to $531 \cdot \rho_{Ag}$ ($300 \cdot R_{m/sh,Ag}$) while enabling recovery and reuse of $99\,\%$ of the metal powder from the prints. Increasing the sintering time to $40\,\mathrm{min}$ reduced $R_{m/sh}$ approximately by a factor of 2 ($271 \cdot \rho_{Ag}$), but reduced the recycling yield to $48\,\%$ of the metal powder. Note that the resistivities of the recyclable and recycled printed leads are comparable to industrially applied materials. For example, silver conductive pastes from Henkel, Dycotec, and Sigma-Aldrich, have resistivities ranging from $1.8 \times 10^{-5}\,\Omega\,\mathrm{cm}$ ($11 \cdot \rho_{Ag}$) to $2.5 \times 10^{-5}\,\Omega\,\mathrm{cm}$ ($157 \cdot \rho_{Ag}$) [138–140], on the same order as our recyclable material.

3.4 Conclusion

We studied the low-temperature sintering of silver microparticles (AgμP) and used it to prepare printed layers with resistivities of $271 \cdot \rho_{Ag}$ ($150 \cdot R_{m/sh,Ag}$). The sinter necks in these layers had diameters below $0.8\,\mu$m; they were mechanically weak enough to cleave them in a subsequent recycling process and recover the silver as printable powder.

Precipitated, surfactant-coated (P-), and surfactant-free, atomized silver microparticles (A-AgμP) were sintered at temperatures of $140\,^{\circ}$C and $275\,^{\circ}$C, both below the onset of surface and grain boundary diffusion sintering. The formation of conductive necks at these temperatures implies the existence of a mobile silver species, most likely ions, that provide mass transport fostered by surfactants. An Arrhenius analysis of the temperature-dependent onset of sintering indicates an activation energy of $140\,\mathrm{kJ\,mol^{-1}}$, which suggests that the formation of silver ions at the silver surface is the rate-limiting step of low-T sintering. This leads to a characteristic, sharp drop in $R_{m/sh}$ for A-AgμP at an onset time of t_{onset}, which we link to the formation of necks. Our model explains the common observation of nanoparticles in low-T sintering of silver, too: they form due to homogeneous nucleation at locations where no necks can form.

We used these results to introduce recyclability-by-design to printed silver layers. Weakly sintered P-AgμP layers reached ρ of $531 \cdot \rho_{Ag}$ ($300 \cdot R_{m/sh,Ag}$) at $150\,^{\circ}$C after $20\,$min at an average thickness of $21.5\,\mu$m, competitive to other printed conductive silver films. We recovered powder from the films and were able to reuse $99\,\%$ of the silver in printing. The resulting prints surpassed the conductivity of the original films. We studied the trade-off between sintering time and recyclability: sintering at $40\,$min reduced ρ (and also $R_{m/sh}$) by a factor of 2, but reduced the recycling yield to $48\,\%$ of the metal powder.

3.5 Experimental section

Printing and preparation of metal pastes

Commercial precipitated (S14010-NM1 Ag powder, Ames Goldsmith, United Kingdom) and atomized (Ag-HWQ 1.5 µm, Fukuda Metal Foil and Powder Co., Ltd., Japan) silver microparticles with average diameters of 1.5 µm and 1.7 µm were used to create screen printing pastes. The respective dry silver (Ag) powder was mixed with ethylene glycol (EG, anhydrous 98 %, Sigma Aldrich) at weight ratios of 10:1 (Ag:EG, precipitated particles) or 9:1 (Ag:EG, atomized particles) using a bladeless mixer (SpeedMixer DAC 150.3 SP, Hauschild, Germany) at 2350 rpm for 3 min, resulting in a highly viscous paste.

Lines of $1 \times 3\,\mathrm{cm}^2$ were screen-printed with a manual screen printer using a mesh of 120 polyester threads per centimeter on microscopy glass slides (VWR, ground edge frosted, Germany). The thickness was determined taking the average of 3 samples, with a 3D confocal microscope MarSurf CM explorer (Mahr, Germany), and found to be 21.5 µm for the precipitated prints and 37.5 µm for the atomized prints. Directly after printing, the prints were heat treated in air inside an oven (Thermoscientific VACUtherm, Germany) at temperatures indicated in the main text for 30 min. Afterward, the samples were cooled down at room temperature. Three samples were prepared for each heat treatment unless stated otherwise.

Characterization methods

Thermogravimetric analysis (Perkin Elmer TGA 8000, Germany) was performed to determine the weight fraction of organic surfactants on the surface of both precipitated and atomized silver microparticles. 20 mg powder was heated in N_2 from 30 °C to 400 °C at 10 °C min^{-1}, then 900 °C at 30 °C min^{-1}.

The concentration of mobile silver that is released from the silver surfaces in the form of ions, complexes, or clusters was quantified by washing and elemental analysis. The particles were dispersed in isopropanol at a concentration of 1 mg mL^{-1} and the dispersion was kept overnight to let the particles sediment. The sedimented particles were then separated from the supernatant by decanting. Inductively Coupled Plasma Optical Emission Spectroscopy (ICP-OES, Ultima2, Horiba Jobin Yvon, France) indicated the concentration of free silver released from the particle surface.

The internal structure of the particles was analyzed using printed, untreated lines prepared as described above. A cross-section was prepared by etching a trench through the entire printed layer with a Focused Ion Beam (FEI Versa 3D DualBeam). The cross-section was imaged using Scanning Electron Microscopy (SEM, Quanta 400 ESEM, Thermo Fisher Scientific GmbH, Germany) using the secondary electron detector. Additional top-view SEM micrographs of other spots were used to verify the presence of sinter necks between the particles by visual inspection.

Directly after the heat treatment, the electrical conductivities of the printed lines were quantified with a four-point probe set up using a 2450 Sourcemeter (Keithley Instruments, Ohio, USA) using four in-line conical gold pins (GKS-069 201 051 A 0700, Ingun, Germany) with a pin-to-pin distance of 1 mm.

Selected samples were electrically characterized in-situ during the heat treatment using a two-point connection. The printed samples were first dried in a vacuum oven at 60 °C for 2 h. They were then mounted on a programmable hot plate using Kapton tape (Plano GmbH, Wetzlar, Germany) and connected using two 20 cm copper wires at both ends of the printed line using conductive silver paste (G3692, Plano

GmbH, Wetzlar, Germany), that led to a multichannel sourcemeter (DAQ6510 data acquisition logging multi-meter system) which was equipped with multiplexer cards (7702 40-channel differential multiplexer module with screw terminals) from Keithley Instruments GmbH (Germering, Germany). The copper wires were connected to the multichannel source meter using metallic clamps. A constant voltage bias of $0.1\,\mathrm{mV}$ was applied, and the resistance was calculated every second using Ohm's Law, and recorded.

The hotplate was heated at $28\,^{\circ}\mathrm{C\,min^{-1}}$ to set-temperature while measuring resistance every second during at least $90\,\mathrm{min}$. The clamp-to-wire and wire-to-layer contact resistances were measured first and subtracted from the resistance values of the connected sample. The sheet resistance was calculated by dividing the printed layer resistance by the layer aspect ratio $3\,\mathrm{cm}/1\,\mathrm{cm} = 3$. The sheet resistance was multiplied by the overall weight of the printed layer from gravimetry to obtain a mass-normalized sheet resistance.

3.6 Acknowledgement

We acknowledge Dominik Perius for his preparation of printed layer cross-sections via FIB-SEM and Albenc Nexha for X-ray diffraction analyses. This work was supported by the German Federal Foundation for the Environment (DBU). We thank Jochen Wahl (CEO of GSB Wahl GmbH) for his contributions to discussions on low-impact conductive pastes. Finally, we also thank Professor Eduard Arzt for fruitful discussions about sintering.

3.7 Author contributions

Tobias Kraus and Lola González-García took part in the planning, discussion, and revisions of the manuscript. David van Impelen performed the experiments, processed the data, and wrote the paper.

4 The importance of shape: flakes and spheres in recyclable conductive pastes for printed electronics

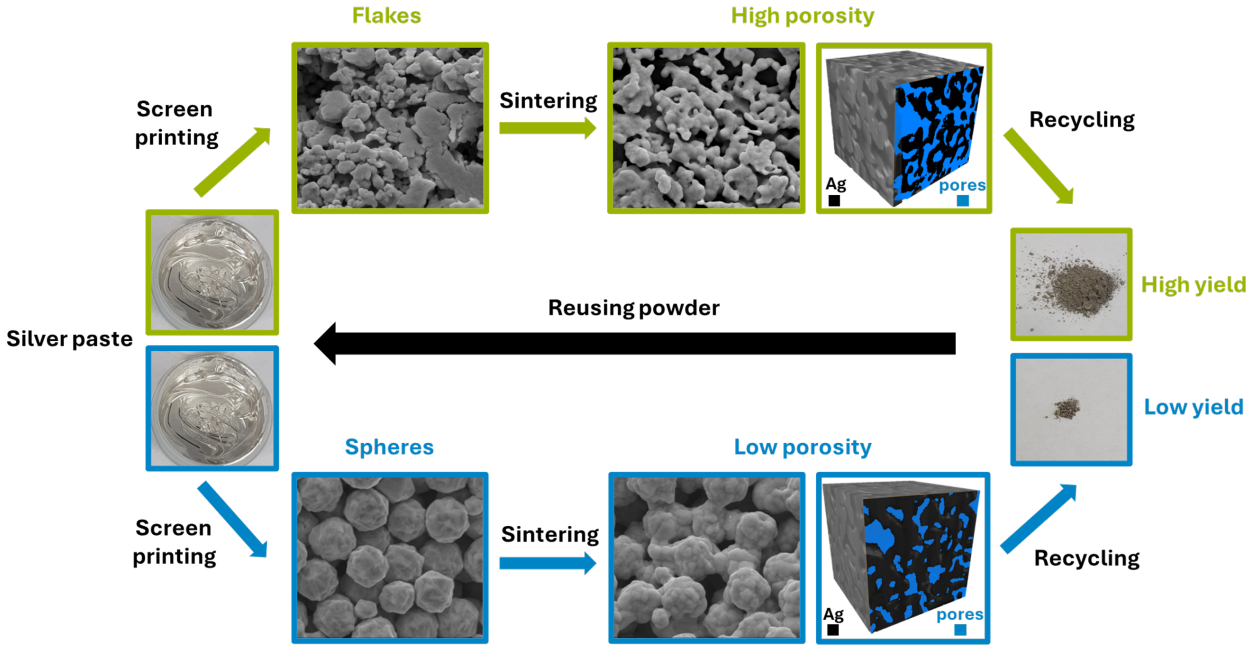

Reprinted with permission from:
D. van Impelen, D. Perius, L. González-García, T. Kraus, *The importance of shape: flakes and spheres in recyclable conductive pastes for printed electronics*, RSC Sustainability 2024.

4.1 Abstract

Silver microflakes and -spheres are common fillers for electrically conductive screen-printing pastes. Here, we report on the effects of filler shapes and sizes on conductivity, sintering, and recyclability. We printed pastes based on flakes and spheres, treated them at 110 °C to 300 °C, and evaluated the electrical conductivity of the resulting layers. The electrical conductivity of the layers treated at 110 °C was dominated by particle-particle contact resistances; flakes yielded layers that were five times more conductive than sphere-based layers due to differences in the particle-particle contact area. Increasing temperature led to a reduction of the resistivity of all layers through sintering. At 300 °C, prints based on spheres were 4 times more conductive than those from flakes. Tomography of the sintered structures showed that the difference was caused by a lower tortuosity factor for spheres. In a final study, we showed that silver flakes and spheres could be recycled after sintering and reused for a new generation of prints without losing electrical performance. The more porous structure of sintered flakes allowed for higher recycling yields compared to spheres. At 140 °C, 91.6 % of the flakes and 69.7 % of the spheres were recovered as reusable dispersions.

4.2 Introduction

Printing electronic devices and circuits with conductive paste or ink formulations makes effective use of conductive materials, enables low-temperature processing, and gives designers the possibility to use a large variety of substrates [141, 142]. Conductive paste formulations for screen printing typically contain metal particles [142], carbon materials [143, 144], or conductive polymers [145] in non-conductive polymer matrices. Silver particles dominate the market due to silver's high electrical conductivity, conductive oxide, and stability at high temperatures [146, 147]. Heat treatments after printing remove solvent and sinter the particles, and a common challenge in paste development is to reach a high conductivity at low or moderate temperatures and after short times.

Silver nanoparticles can rapidly fuse at low temperatures[148]. They have large specific surfaces that are strongly curved, and the diffusion paths between particles are short. Treatments below 200 °C thus result in highly conductive prints with a resistivity ranging from 3.45 μΩ · cm to 8.0 μΩ · cm. However, nanoparticles are expensive and prone to agglomeration. Stabilized nanoparticles carry a relatively large fraction of stabilizing organics that form pores and reduce conductivity [141, 148].

Silver microparticles are more readily available, contain lower amounts of organics, and are cheaper than nanoparticles. They are often used as conductive fillers for metal-based screen printing pastes. Experimental studies have shown that silver microparticles can be sintered at temperatures below 200 °C to obtain resistivities down to 8.33 μΩ · cm [11–13, 149]. The observed sintering times are much shorter than predicted diffusion-based sintering models [10]. Van Impelen *et al.* report that silver was not transported among microspheres with classical surface or bulk diffusion processes, but involved the creation of mobile ionic silver that rapidly diffused and precipitated to form necks. This mechanism was aided by residual organic molecules so that the onset temperature depended on the production method of the particles [149]. Surfactant-containing precipitated silver particles started sintering at 140 °C, compared to 275 °C for surfactant-free atomized silver particles.

Silver microflakes are a common alternative filler [11, 64, 150–155]. Prints based on flakes can reach low resistivities down to $284\,\mu\Omega \cdot \mathrm{cm}$ upon drying and without sintering, which has been attributed to the high particle-particle interface area caused by the alignment of flakes [156]. Some groups reported that micro flakes can be sintered at lower temperatures than microspheres [62, 150, 151] due to microstrains in flakes [62]. The release of this microstrain resulted in the formation of nanoparticles, which aided the sintering.

Silver is an expensive material and its production has a significant environmental impact. A life cycle analysis by Naji *et al.* identified the conductive metal inks as the largest environmental impact factor of printed electronic [110]. Recycling of metal powders can significantly reduce this impact. Kang *et al.* designed a recyclable gold nanoparticle ink for inkjet printing [157]. The printed ink could be separated from the substrate and the particles were redispersed by sonication to form a recovered ink formulation. Kwon *et al.* printed conductors based on silver micro flakes and were able to recycle the silver particles [22]. They formulated new pastes from the recovered silver particles and the recycled printed conductors had similar electrical performances. None of these inks were sintered, however, and their conductivities were orders of magnitude above that of silver. Van Impelen *et al.* studied weakly sintered silver microparticle structures and found that weak sinter necks could be broken to recover printable silver particles [149]. They reported a trade-off between reducing the resistance of the prints through sintering and the ease of recycling the particles. We are not aware of any reports on the recycling of prints based on silver micro flakes.

This manuscript directly compares the conductivities and the recyclabilities of silver microspheres and -flakes in printed layers after heat treatments at $110\,^{\circ}\mathrm{C}$ to $300\,^{\circ}\mathrm{C}$. We provide an explanation for the increased conductivity observed for flakes treated at lower temperatures and spheres treated at higher temperatures and show that flakes have a higher recycling efficiency. The resulting data enables a rational choice of particle geometry and sintering temperatures depending on the desired application. To our knowledge, we are the first to compare the electrical conductivity and recyclability of printed silver flakes and spheres sintered at low and high temperatures.

4.3 Materials and methods

4.3.1 Metal powders

Precipitated silver microspheres with average diameters of 1 and $1.5\,\mu\mathrm{m}$ (S14024-NM1 and S14010-NM1 Ag powder, Ames Goldsmith, United Kingdom) and precipitated micro flakes with average equivalent diameters of 2.8 and $3.2\,\mu\mathrm{m}$ (SF65 and SF91 Ag powder, Ames Goldsmith, United Kingdom) were purchased. The volume-equivalent sphere diameters of the flakes reported here were obtained from laser diffraction.

4.3.2 Printing and preparation of paste

Pastes were prepared by mixing the particles with Ethylene Glycol (EG, anhydrous $98\,\%$, Sigma Aldrich) at a weight ratio of Ag:EG of 5:1 for flakes and 10:1 for spheres. A bladeless mixer (SpeedMixer DAC 150.3 SP, Hauschild, Germany) operated at $2350\,\mathrm{rpm}$ for $3\,\mathrm{min}$ ensured the formation of homogeneous,

highly viscous pastes.

The pastes were used to screen-print rectangles of 1×3 cm^2 with a manual screen printer using a mesh of 100 polyester threads per centimeter on microscopy glass slides (VWR, ground edge frosted, Germany). The thickness of the printed layers was determined with a 3D confocal microscope MarSurf CM explorer (Mahr, Germany) by averaging three measurements on three samples. Prints containing $2.8 -$ and 3.2 µm flakes had average thicknesses of 18.9 and 18.2 µm, prints containing 1 and 1.5 µm spheres had 17.5 and 21 µm. Prints used for the experiments described in the section 'Sintering of flakes and spheres at different temperatures' were placed in a preheated oven (Thermoscientific VACUtherm, Germany) for 30 min. Prints used in experiments in Section 4.4.2 were placed on a preheated hotplate with a closed lid (PZ28-3TD, Präzitherm, Germany) coupled to a PID controller (PR5-3T, Präzitherm, Germany) for 30 min. All reported resistance values in this manuscript are an average of at least three samples.

4.3.3 Characterization methods

The weight fraction of surfactants on the particle surface was quantified with Thermogravimetric Analysis (TGA, Perkin Elmer TGA 8000, Germany). 20 mg powder was heated in N_2 from $30\,^{\circ}$C to $400\,^{\circ}$C at $10\,^{\circ}$C min^{-1}, then to $900\,^{\circ}$C at $30\,^{\circ}$C min^{-1}.

A four-point probe measurement set-up with a 2450 Sourcemeter (Keithley Instruments, Ohio, USA) using four in-line conical gold pins (GKS-069 201 051 A 0700, Ingun, Germany) with a pin-to-pin distance of 1 mm was used to measure the resistance of the printed samples. The mass-normalized sheet resistance was determined, as introduced in previous work [149],

$$R_{m/\mathrm{sh}} = m * R_{\mathrm{sh}}, \tag{4.1}$$

where m is the printed metal mass and R_{sh} the sheet resistance of the printed sample.

A dual beam electron microscope (FEI Versa 3D Dualbeam) was employed for focused ion beam scanning electron microscopy (FIB-SEM) tomography. Software (Autoslice and View G3, Thermo Scientific, USA) was used to control the microscope and automatically remove 350 slices of width $90\,nm$ at an ion current of $5\,nA$ and $30\,kV$. After every slice, a tilt-corrected secondary electron (SE) image (1536×1024 pixel, $90\,nm$ pixel size) was recorded at a magnification of 1500 and a dwell-time of $1\,\mu s$. The SE images were reconstructed using the AVIZO software (Version 2021, Thermo Scientific): the data processing included image stack alignment, shearing, and cropping before edge-preserving non-local means filtering yielded the final, 3D-reconstructed image stack. The stacks were subsequently segmented using manual grayscale histogram thresholding. For a detailed description and a review of FIB-SEM tomography, we refer the reader to the work of Holzer and Cantoni [158].

The silver phase provided good contrast against the pore space. This enabled us to set the threshold at the minimum between the two present maxima of the two-phase (pores and silver) grayscale histogram. Reconstructed volumes of size $46.8\,\mu m \times 15.6\,\mu m \times 15.6\,\mu m$ were cropped to obtain three isotropic, binary cubes of size $(15.6\,\mu m)^3$, where the silver phase voxels had a value 1 and the pore space 0. Each cube was exported to a single $.tif$ file and used as input for the MATLAB code Taufactor[159], which simulated Fickian diffusion on the silver phase voxels. The diffusional tortuosity (tortuosity factors) was calculated by simulating the diffusional flux against a concentration gradient for the silver phase and a

homogeneous representative volume element (REV)[160] in every direction and dividing their resulting fluxes to yield the tortuosity factors $\tau_{d,x}$, $\tau_{d,y}$ and $\tau_{d,z}$. The individual directions were summarized in $\tau_{d,3D}$ as the root-mean-square of the individual directions. In total three cubes for each sample were computed to obtain the mean $\overline{\tau_{g,3D}}$. Geometrical tortuosity was calculated using the MATLAB code "Tort3D" from Cecen *et.al.*[161]. This code calculates the distribution of geometrical tortuosities from the binary volume in the z-direction only. We rotated the cubes twice to obtain the distributions for all spatial directions. The root-mean-squares of the average $\tau_{g,x}$, $\tau_{g,y}$ and $\tau_{g,z}$ were calculated for each cube to obtain the three-dimensional equivalent $\tau_{g,3D}$ of the geometrical tortuosity, and again from three cubes the mean $\overline{\tau_{g,3D}}$ was used to compare flakes and spheres.

4.4 Results and discussion

4.4.1 Sintering of flakes and spheres at different temperatures

We prepared pastes containing silver flakes and spheres. Silver flakes (Ag-F) had average diameters (of the volume-equivalent spheres) of 2.8 and 3.2 µm and the spheres (Ag-S) of 1 and 1.5 µm. Spheres had monomodal size distributions, while flakes had bimodal size distributions with a peak at 1 µm and a peak between 3 and 4 µm. Flakes had higher specific surface areas: 1.11 and 0.71 $\frac{\mathrm{m}^2}{\mathrm{g}}$ for 2.8 and 3.2 µm Ag-F compared to 0.37 and 0.26 $\frac{\mathrm{m}^2}{\mathrm{g}}$ for 1 and 1.5 µm Ag-S.

The spheres were produced by chemical precipitation and contained 0.41 and 0.33 wt-% of surfactants. The flakes were made by mechanical milling of precipitated spheres and contained 0.5 and 0.4 wt-% of surfactants. The pastes were screen printed on glass and treated in the oven at $110\,^{\circ}\mathrm{C}$ to $300\,^{\circ}\mathrm{C}$ for 30 min. We used the mass-normalized sheet resistances ($R_{m/\mathrm{sh}}$) introduced in previous work [149] to electrically characterize the prints (see Section 4.3.3).

Figure 4.1 illustrates the decreasing mass-normalized sheet resistances after thermal annealing for all prints. At $110\,^{\circ}\mathrm{C}$, the prints containing silver flakes reached $R_{m/\mathrm{sh}} \approx 3.0\,\frac{\mathrm{m}\Omega}{\mathrm{sq}} \cdot \mathrm{g}$, considerably below that of spheres at $R_{m/\mathrm{sh}} \approx 14.9\,\frac{\mathrm{m}\Omega}{\mathrm{sq}} \cdot \mathrm{g}$. Both spheres and flakes largely retained their original sizes and shapes (see Figure S1 in the Supporting Information), and SEM imaging did not reveal the formation of sinter necks (see Figure 4.1C and D).

Literature agrees that the resistance of dried metal particle prints is dominated by the particle-particle contact resistances [33–35]. They are caused by the constriction resistances due to the small particle-particle contacts and tunneling resistances due to insulating interlayers [33]. We propose that layers treated at $110\,^{\circ}\mathrm{C}$ are still dominated by contact resistances. Flakes have larger overall particle-particle contact areas, which (at comparable particle sizes and surface states) reduces the overall contact resistances and thus, $R_{m/\mathrm{sh}}$ [64].

Annealing at higher temperatures changed the picture. For silver flakes, $R_{m/\mathrm{sh}}$ decreased with increasing temperature and reached $R_{m/\mathrm{sh}} \approx 0.4\,\frac{\mathrm{m}\Omega}{\mathrm{sq}} \cdot \mathrm{g}$ at 160 and $200\,^{\circ}\mathrm{C}$ and $R_{m/\mathrm{sh}} \approx 0.2\,\frac{\mathrm{m}\Omega}{\mathrm{sq}} \cdot \mathrm{g}$ at $300\,^{\circ}\mathrm{C}$. Layers made from silver spheres became more conductive at elevated temperatures: their resistances reached $R_{m/\mathrm{sh}} \approx 1.2\,\frac{\mathrm{m}\Omega}{\mathrm{sq}} \cdot \mathrm{g}$ at $160\,^{\circ}\mathrm{C}$, but dropped to $R_{m/\mathrm{sh}} \approx 0.1\,\frac{\mathrm{m}\Omega}{\mathrm{sq}} \cdot \mathrm{g}$ at 200 and $300\,^{\circ}\mathrm{C}$. This is approximately twice that of bulk silver ($R_{m/\mathrm{sh,\,Ag}} = 0.05\,\frac{\mathrm{m}\Omega}{\mathrm{sq}} \cdot \mathrm{g}$).

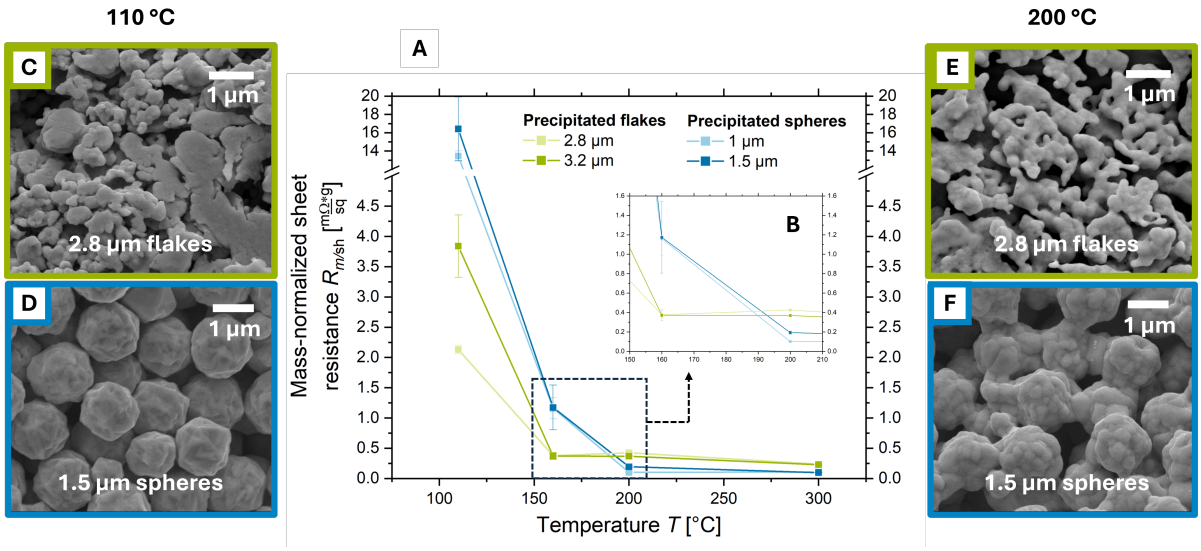

Figure 4.1: Electrical conductivities and microstructures of prints containing silver flakes and spheres after thermal annealing for 30 min. (A) Mass-normalized sheet resistances $R_{m/\mathrm{sh}}$ as a function of temperature T for prints containing 2.8 or 3.2 µm flakes (green lines), and 1 or 1.5 µm spheres (blue lines). (B) Inset: resistance changes at 150 °C to 200 °C, where sphere become more conductive than flake prints. (C) Top-view scanning electron micrographs of prints containing 2.8 µm flakes and (D) 1.5 µm spheres treated at 110 °C. (E-F) The same for flake and sphere prints after treatment at 200 °C.

Figures 4.1E and F illustrate the sinter necks that formed at 200 °C for flakes and spheres, respectively. After the formation of such necks, conducting electrons no longer need to tunnel from particle to particle, since the particles are now interconnected. The contact resistances decrease and become dominated by the constriction resistance, which strongly depends on neck size [9, 33].

We propose that the necks are responsible for the drop in $R_{m/\mathrm{sh}}$ that we observed for both flakes and spheres above 110 °C. At first, the tunneling contacts are converted into sinter necks, leading to a sharp decrease in $R_{m/\mathrm{sh}}$. The growth of initially formed necks more slowly reduces $R_{m/\mathrm{sh}}$ through the reduction of the restriction resistance [33]. The drop in $R_{m/\mathrm{sh}}$ strongly slowed down above 160 °C for flakes and above 200 °C for spheres. At 300 °C, large necks had formed and converted the printed structures into a porous metal (see Figure S2 of the Supporting Information).

The $R_{m/\mathrm{sh}}$ of the porous metal formed at 300 °C was 4 times that of bulk polycrystalline silver [116] for flakes and 2 times that for spheres. Multiple studies have shown that nanocrystalline metals have higher resistivities than polycrystalline metals due to the large numbers of grain boundaries [162–164]. We measured the grain size of the porous metal formed from silver flakes and spheres sintered at 300 °C using X-Ray Diffraction (XRD) and found sizes of 46 and 48 nm, respectively (see Figure S3 of the supporting information). This difference is too small to explain the bulk conductivity differences: Qin *et al.* measured a resistivity of 2.4 µΩ · cm for nanocrystalline silver with an average grain size of 25 nm and 1.6 µΩ · cm for micron-sized grains [162]. We thus attribute the increased $R_{m/\mathrm{sh}}$ to the remaining porosity.

The thicknesses and weights of prints containing 2.8 µm-sized flakes (Figure 4.2A) and 1.5 µm-sized spheres (Figure 4.2B) treated at 110 and 300 °C indicate minimal shrinkage for both, in agreement with initial stage sintering [9]. Interestingly, the average thicknesses of flake- and spherical-based prints were comparable, but the average weight per area of the sphere-based prints was almost twice that of flake-based prints. This suggests a higher porosity of flake-based prints.

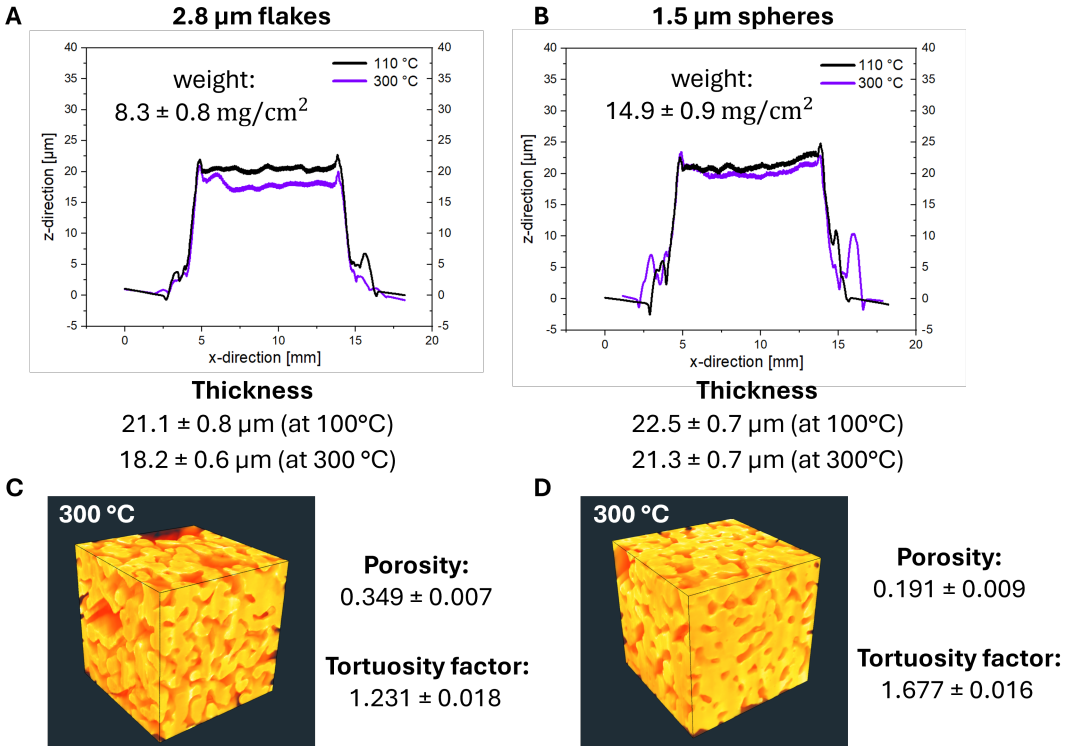

Figure 4.2: Structures of sintered prints of flakes and spheres. Surface profiles of prints treated at 110 and 300 °C containing (A) 2.8 µm flakes and (B) 1.5 µm spheres from confocal microscopy. 3D reconstructions from FIB-SEM tomography of (C) prints based on 2.8 µm flakes treated at 300 °C and (D) prints based on 1.5 µm spheres treated at 300 °C.

We determined the porosities of sintered prints treated at 300 °C by cutting microscopic volumes of size $46.8\,\mu m \times 15.6\,\mu m \times 15.6\,\mu m$ with a focused ion beam from the samples, removing slices from it and recording 175 electron micrographs (Figure 4.2, see Materials and Methods). Porosities and the geometrical and diffusional tortuosities of the silver phase were then calculated for three subvolumes as described in the Methods section and averaged.

The average porosity of flake-based prints was found to be 0.349 compared to only 0.191 of sphere-based prints. One might expect that flakes can pack efficiently in a tile-like fashion, but Yoshinaga *et al.* already noticed that metal microspheres pack more densely than flakes of comparable sizes [165]. They studied packing in compressed powder electrodes; we propose that screen-printing of viscous pastes also leads to porous flake arrangements.

The higher porosity of the sintered flake structures explains the difference in $R_{m/\mathrm{sh}}$. Random porosity causes constrictions and extends the lengths of conductive paths, increasing macroscopic electrical resistance. The geometrical tortuosity of our printed structures can be quantified using the geometrical tortuosity

$$\tau_g = \frac{L_g}{L}, \tag{4.2}$$

where L_g is the length of the transport path and L the Euclidean distance between the start- and endpoint of the path [166]. Large τ_g imply longer transport paths that can indicate larger overall resistances, but τ_g does not describe constrictions. The diffusional tortuosity has been defined to consider the effect of passages with small cross-sections:

$$\tau_d = \frac{D \cdot \varepsilon}{D_{eff}}, \tag{4.3}$$

where D_{eff} is the diffusivity through a porous volume with impenetrable walls, D is the intrinsic diffusivity, and ε the porosity. τ can be used as a measure of electrical conductivity because electron transport in a potential gradient follows the same functional form as diffusion in a concentration gradient[167].

We calculated geometrical and diffusional tortuosity factors of our samples from their reconstructed geometries using the open-source MATLAB codes "Tort3D"[161] and "TauFactor"[159], respectively. Voxelized binary data from segmented 3D reconstructions of the silver phase of the prints were used as input. The average τ was $1.164\,\mathrm{pm}0.001$ for the sintered flakes, compared to $1.069\,\mathrm{pm}0.003$ for the sintered spheres. The differences are small and both values close to 1, indicating that the different porosities did not perceptibly increase the average path length of conducting electrons.

The diffusional tortuosities τ_d, however, were clearly different at 1.231 ± 0.007 for sintered flakes and 1.677 ± 0.016 for sintered spheres. The conductive paths in sphere-based metal layers had more constrictions that locally increased the electrical resistance. They explain the higher $R_{m/\mathrm{sh}}$ of layers made by sintering flakes even when the silver content was identical to that of spheres. In summary, the flake prints electrically outperformed sphere prints after a treatment at $110\,^{\circ}\mathrm{C}$ for $30\,\mathrm{min}$. We propose that this difference stems from larger particle-particle contact areas between the flakes that reduce $R_{m/\mathrm{sh}}$. Increasing temperature led to a cross-over at $200\,^{\circ}\mathrm{C}$ because spheres yielded denser layers that provided conductive paths with less geometrical constrictions.

4.4.2 Recycling of flakes and spheres

The different contact geometries suggest that the recyclability of weakly sintered films differs for spheres and flakes. To test this, pastes containing $2.8\,\mu\mathrm{m}$ flakes and $1.5\,\mu\mathrm{m}$ spheres were printed, treated at different temperatures, recycled, and used for new prints. The results are shown in Figure 4.3.

Figure 4.3A shows the circular process of printing and recycling. Pastes containing spheres or flakes were printed and treated at 120 , 140 , and $160\,^{\circ}\mathrm{C}$. The resistances of the prints are given in Figure 4.3B as 'initial'. The printed metal was then mechanically removed from the substrate to obtain "recovered powder" (see Figure 4.3A). The recovered powder contained individual particles and sintered aggregates. The size of sinter necks increased with increasing treatment temperature, leading to more strongly sintered aggregates in the recovered powder (see Figure S4 of the Supporting Information). To avoid clogging during screen-printing, we fragmented aggregates by probe sonication in isopropanol (IPA). The sonicated

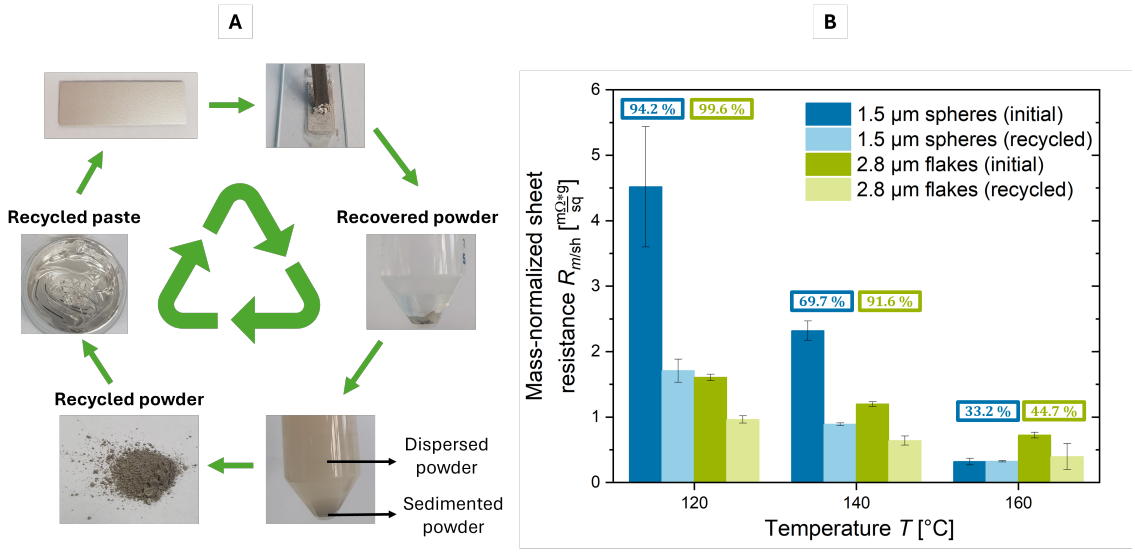

Figure 4.3: The recycling of sintered prints of flakes and spheres followed the process shown in (A). Weight-normalized sheet resistances $R_{m/\mathrm{sh}}$ of prints of new ('initial') and recycled particles are shown in (B) as a function of sintering temperature T for 1.5 µm spheres (blue) and 2.8 µm flakes (green) treated for 30 min. The weight fractions indicate how much powder was recycled from the initial prints.

suspension was kept at rest for 2 min so that it formed two phases: sedimented powder at the bottom and dispersion in the supernatant (see Figure 4.3A). The sediment contained large aggregates, the dispersion smaller aggregates or individual particles. The supernatant was decanted, centrifuged, and dried to obtain the recycled powder. The sediment that could not be dispersed was removed and considered as loss. The recycling yields indicated in Figure 4.3B were determined by dividing the weight of recycled powder by the total weight of the recovered powder. The recycled powder was then reused to create a new paste, printed, and treated at the same temperature as the initial prints. $R_{m/\mathrm{sh}}$ of the recycled prints are shown in Figure 4.3B.

At 120 °C, 99.6 % of the flakes and 94.2 % of the spheres were recycled. At 140 °C, 91.6 % of the flakes were recycled but only 69.7 % of the spheres; at 160 °C, recycling yields were 44.7 % for flakes and 33.2 % for spheres.

The results are consistent with the evolution of sinter necks. No necks had formed at 120 °C (see Figure S4 of the Supporting Information), minimizing the loss fraction and maximizing the recycling percentage both of flakes and spheres. The situation changed at 140 °C. Flakes and spheres formed visible sinter necks (see Figure S4 of the Supporting Information) that yielded sintered aggregates in the recovered powder. Consequently, the loss fraction increased and the recycling yield decreased. The yield decreased more rapidly with temperature for spheres than for flakes. Printed flakes were 1.8 times more porous than printed spheres. We propose that the higher porosity made the flake layers mechanically weaker and eased the breakup of aggregates in the recovered powder. The improved redispersibility reduced the loss fraction and aided recycling (see Figure 4.4). This is consistent with the results of Wakamoto *et al.*, who compared the mechanical properties of sintered silver films at porosities of 5 , 6 , 14 , and 25 %[168]. They used tensile testing to show that their ultimate tensile strength decreased with porosity, while brittle fracture occurred at lower strains.

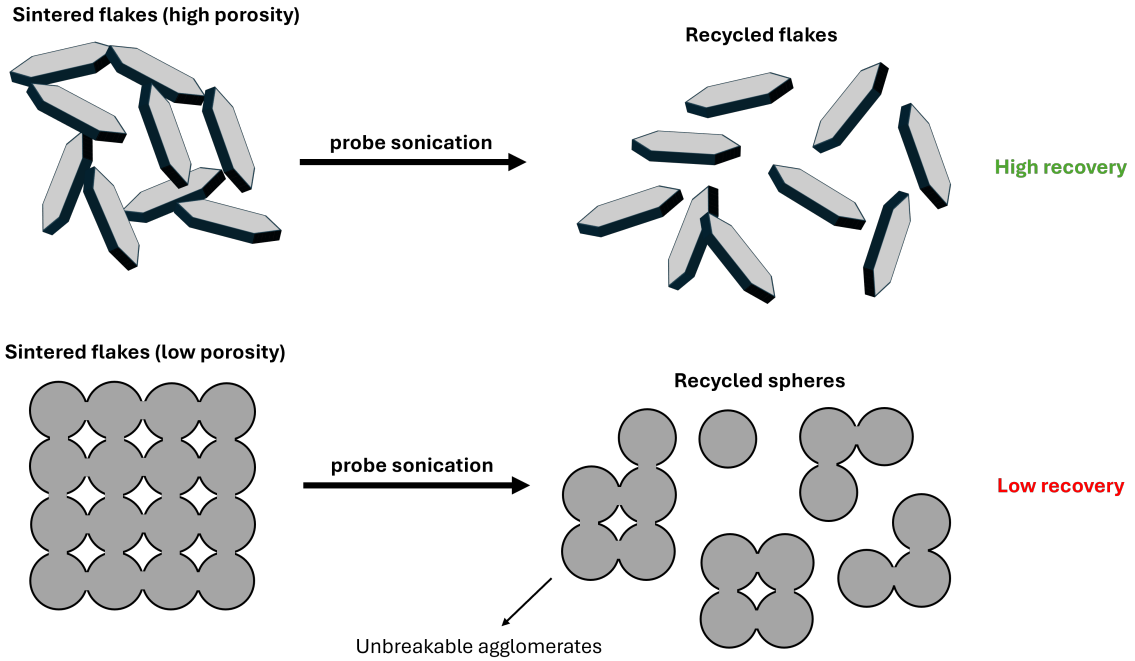

Figure 4.4: Aggregates of sintered flakes were mechanically weaker and more easily dispersed by probe sonication. Aggregates of sintered spheres were stronger, increasing the powder loss fraction.

The sinter necks at 160 °C were larger, making the aggregates more difficult to break (see Figure S4 of the Supporting Information). Consequently, a larger amount ended up in the loss fraction, leading to lower recycling yields both for flakes and spheres (see Figure 4.4B).

The $R_{m/\mathrm{sh}}$ of the initial prints decreases with increasing temperature for spheres and flakes, consistent with the formation of sinter necks. Initial prints consistently had greater $R_{m/\mathrm{sh}}$ than recycled prints. We found small aggregates with visible sinter necks in electron micrographs of the recycled powders (Figure S5 of the Supporting Information). We propose that they are small enough to fit through the screen-printing mesh, which has a mesh opening size of 60 µm, get embedded in the recycled prints, and lower $R_{m/\mathrm{sh}}$ through reducing the sum of particle-particle contact resistances.

4.5 Conclusions

We compared microscale silver flakes and spheres in metal-based printed conductors. Conductivities, sintering mechanisms, and recyclabilities of prints with different particles at the same silver mass loading per unit area were compared.

Conductive prints were obtained after 30 min at 110 °C for both flake- and sphere-based prints. Neither flakes nor spheres sintered under these conditions, but tunnel barriers were removed. Flakes clearly outperformed spheres in conductivity, they had only a quarter of the mass-normalized sheet resistance $R_{m/\mathrm{sh}}$ of spheres. We attribute this advantage to the larger overall particle-particle contact area of flakes in prints.

Temperatures above 110 °C reduced $R_{m/\mathrm{sh}}$ through the formation of sinter necks. The conductivity of sphere prints exceeded that of flake prints when sintering at 200 °C and above. $R_{m/\mathrm{sh}}$ of spheres dropped

to half of that of flakes and remained at this level when increasing temperature. Layers of sintered spheres were less porous and had lower tortuosity factors than flake-based prints, explaining this difference.

The recycling of printed flakes yielded larger yields than that of spheres. The higher porosity of sintered flake layers aided the mechanical breakup of aggregates and minimized the sedimented loss fraction. At $140\,^{\circ}\mathrm{C}$, $91.6\,\%$ of the flakes but only $69.7\,\%$ of the spheres were recycled.

Overall, silver flakes are more suited for low thermal budget, highly conductive, and recyclable printed conductors. Silver spheres enable reaching the lowest possible resistivity. Sintering the spheres at $200\,^{\circ}\mathrm{C}$ for $30\,\mathrm{min}$ resulted in a $R_{m/\mathrm{sh}}$ of only twice that of bulk silver.

Author contributions

David van Impelen wrote the original draft of the manuscript and performed the majority of the experiments. Dominik Perius performed FIB-SEM tomography, made the 3D reconstructions, and wrote the section on tortuosities and 3D reconstructions. All authors took part in the conceptualization, reviewing, and editing of the manuscript. Tobias Kraus and Lola González-García were leading the supervision. Tobias Kraus was responsible for the funding acquisition and resources.

Conflicts of interest

There are no conflicts of interest to declare.

Data availability

The data supporting this article have been included as part of the Supplementary Information.

Acknowledgements

We acknowledge Albenc Nexha for the X-ray diffraction analyses. This work was supported by the German Federal Foundation for the Environment (DBU). We thank Jochen Wahl (CEO of GSB Wahl GmbH) for his contributions to discussions on low-impact conductive pastes.

5 Copper particles for printed electronics

5.1 Introduction

There is a growing interest in replacing silver-based pastes with cheaper, more sustainable, and readily available alternatives. Copper has a high conductivity [65], is cheaper than silver [66, 67], and more abundant [68, 69]. Therefore, many attempts have been made to replace silver with copper particles in conductive pastes [70, 71]. Challenges include copper's tendency to form electrically insulating oxides in air [75, 76, 82] and the fact that copper particles typically require a higher sintering temperature than silver despite the comparable melting points [70, 71]. Printed copper conductors are usually treated at temperatures above $250\,°C$ in nitrogen or reducing atmosphere, which increases cost.

Copper has two stable oxide phases, namely Cu_2O and CuO. A clean copper surface oxidizes readily in air at ambient conditions to form a thin native oxide layer with a thickness of a couple of nanometers [72–74]. This native oxide layer passivates the copper surfaces, preventing further growth. There is consensus in the literature that the main component of the native oxide is Cu_2O [72]; some groups claim the presence of CuO [73, 74]. Since copper oxides are electrically insulating, the native oxide layer affects the conduction across interfaces. The electrical conductivities of copper thin films degrade when the temperature is increased in air such that the self-limiting diffusion barrier of the native oxide layer fails [75]. Choudhary *et al.* found that films with thicknesses between 100 and $1000\,nm$ [75] formed an amorphous Cu_2O phase on top of the native oxide layer at $150\,°C$ that strongly increased their sheet resistances.

Conductive films of printed copper particles suffer more severely from the native oxide layer. The high specific surface area of copper powders renders them non-conductive after printing. Sintering can increase conductivity by forming metallic necks between particles, but the native oxide hinders efficient sintering below $400\,°C$ [81]. Strategies to reduce the sintering temperature include polymer surfactants [79, 80], coating particles with metals [71, 80], and additives in paste formulations [81, 82].

The addition of L-ascorbic acid (AA, vitamin C) to copper-based paste formulations can suppress the oxidation of copper[81, 82]. Gao *et al.* investigated this effect of AA addition on the sintering of copper microparticles. Firstly, they printed a paste of copper particles with diameters from several nanometers to $500\,nm$ on a copper substrate, placed a copper chip onto it, and sintered the paste to create sintered joints. They found that copper oxides that formed during sintering blocked diffusion at the particle-particle and particle-substrate interfaces and hindered sintering. Incomplete sintering and weak bonds were the result at $350\,°C$ in nitrogen. The addition of AA increased bonding strength[81] by reducing Cu_2O to Cu^0 and preventing further oxidation during sintering by scavenging oxygen. Pacioni *et al.* used UV-visible and Electron Paramagnetic Resonance (EPR) spectroscopy to demonstrate that AA slows down oxidation by reducing copper ions to Cu^0. Gao *et al.* reports that AA is scavenging oxygen through its own oxidation [82].

In this chapter, we prepare printed conductors based on commercially available copper microparticles that were made via a polyol reduction process. In the polyol methods, a metal precursor is precipitated in a glycol solvent to obtain the respective metal nano- or microparticles. This method yields particles

that contain polymer on the surface, which renders the particles more resistant to oxidation [169, 170]. We exploited AA's capability to further suppress copper oxidation.

5.2 Materials and Methods

5.2.1 Preparation and printing of pastes

Commercial precipitated copper particles (C1-1000 and C1-2000, Ames Goldsmith, United Kingdom) with average diameters of 1.5 or 2.5 µm were used to formulate screen printing pastes. The respective dry powder was mixed with ethylene glycol (EG, anhydrous 98 %, Sigma Aldrich) at a weight ratio of 7.5:1 (powder:EG) using a bladeless mixer (SpeedMixer DAC 150.3 SP, Hauschild, Germany) at 2350 rpm for 3 min, resulting in a highly viscous paste.

Lines of $1 \times 3\,\mathrm{cm}^2$ were screen-printed with a manual screen printer using a mesh of 100 polyester threads per centimeter on microscopy glass slides (VWR, ground edge frosted, Germany). The film thicknesses (average of 3 samples) were measured with a 3D confocal microscope MarSurf CM explorer (Mahr, Germany), and found to be 23.9 µm and 24.0 µm for the $1.5-$ and 2.5 µm particles, respectively. The printed samples were heat-treated at $200\,^{\circ}\mathrm{C}$ in air or in vacuum inside an oven (Thermoscientific VACUtherm, Germany). For higher temperature treatments in vacuum, a high temperature tubular oven (D-7521, Gero, Neuheusen, Germany) connected to a vacuum pump (HiCube 80 Eco, D-35614, Pfeiffer Vacuum, Asslar, Germany) was used. After the heat treatments, the samples were stored in laboratory air where the temperature was kept around $20\,^{\circ}\mathrm{C}$ and humidity below $50\,\%$.

5.2.2 Characterization methods

The weight fraction of organic surfactants on the particle surface was determined via Thermogravimetric analysis (Perkin Elmer TGA 8000, Germany). 20 mg powder was heated in N_2 from $30\,^{\circ}\mathrm{C}$ to $400\,^{\circ}\mathrm{C}$ at $10\,^{\circ}\mathrm{C\,min^{-1}}$, then $900\,^{\circ}\mathrm{C}$ at $30\,^{\circ}\mathrm{C\,min^{-1}}$.

The electrical resistance of the printed lines was measured immediately after the samples had cooled down with a four-point probe set up using a 2450 Sourcemeter (Keithley Instruments, Ohio, USA) using four in-line conical gold pins (GKS-069 201 051 A 0700, Ingun, Germany) with pin-to-pin distances of 1 mm. The resistances in Figure 5.1, treated in a Thermoscientific VACUtherm oven, are an average of three samples, and the resistances in Figure 5.2, treated in a high temperature tubular vacuum oven, are an average of at least two samples. Scanning Electron Microscope (SEM) imaging was used from the topside of the prints to analyze the structure of the particles. Energy-dispersive X-ray spectroscopy was performed using Noran System 7 X-ray Microanalysis System (Thermo Scientific, Germany) mounted inside an SEM (same SEM as described before). Three particles per sample were chosen from top-view SEM images at a magnification of 20000X. X-ray spectra were recorded with a zoom-in on the chosen particles at a magnification of 400000X, at a spot size of 5, and an acceleration voltage of 15 kV, and the ratio of the K_α Oxygen: K_α Copper was determined. We report average ratios calculated from the three particles to assess the amount of copper oxide formed during heat treatments.

5.3 Air versus vacuum-annealing of copper-based prints

We printed lines of 1.5 and 2.5 µm precipitated copper particles. The 1.5 and 2.5 µm particles contained 0.75 and 0.6 weight percentage of surfactants on the surface (Figure S1 of the Supporting Information). The prints were treated at 200 °C for 2.5 h in air and vacuum. The conductivity was determined using a 4-point probe measurement, and the oxidation of particles was assessed with Energy Dispersive X-ray (EDX) measurements (see Experimental section). A structural analysis of the treated particles was done by Scanning Electron Microscope (SEM) imaging. The results are shown in Figure 5.1 below.

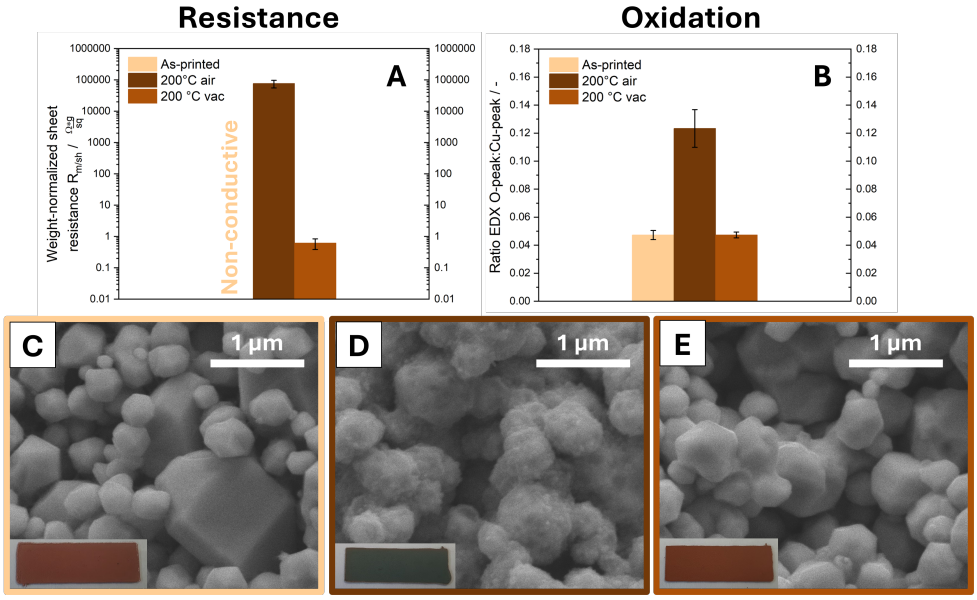

Figure 5.1: Electrical, chemical, and structural analysis of 1.5 µm-diameter copper particles and particles treated at 200 °C in air and in vacuum for 2.5 h. (A) $R_{m/\mathrm{sh}}$ as a function of post treatment. (B) The ratio of the K_α oxygen to the K_α copper reflex intensities in EDX as a function of post-treatment. (C-E) Top view SEM images of untreated prints (C), and prints treated at 200 °C in air (D) and in vacuum (E) for 2.5 h. The left bottom corners of each SEM image show a picture of the respective print.

Figure 5.1A shows the resulting $R_{m/\mathrm{sh}}$ of the prints. The untreated prints were non-conductive, the air-treated prints had a high $R_{m/\mathrm{sh}}$, and the vacuum prints had a low $R_{m/\mathrm{sh}}$. Figure 5.1B shows the ratio of the K_α oxygen to the K_α copper reflex intensities. A higher ratio indicates oxidation of the copper particles in the prints. The ratio for untreated particles was on average 0.04 We propose that the oxygen signal is a result of native oxide on the particles, from oxygen of the surfactants, or of the glass substrate. Treatments in air caused a three-fold increase in this ratio, which strongly suggests oxide formation during the post-treatment. The vacuum treatments, on the other hand, did not increase the oxygen-to-copper ratio compared to the untreated particles. This indicates that the vacuum successfully suppressed oxide growth. A five-fold decrease in $R_{m/\mathrm{sh}}$ for the vacuum treatment compared to the air treatment further supports that the oxide formation during the post-treatment was successfully suppressed.

We also made pictures of the treated prints, shown in Figure 5.1C-E in the left bottom corner. Both the untreated and vacuum-treated prints show the brown characteristic color of copper. The air-treated prints, however, turned black, indicating the formation of CuO. The high resistivity of this copper oxide explains

the five-fold higher $R_{m/\mathrm{sh}}$ of air-treated prints compared to vacuum-treated prints.

Figure 5.1C-E shows top-view SEM images of the treated prints. The untreated particles have a smooth surface with sharp edges (Figure 5.1C). The air-treated particles became rough (Figure 5.1D) and particles lost their individual nature, likely caused by the oxidation on the particle surface. Vacuum-treated particles remained smooth on the surface (Figure 5.1E). Multiple particles were connected through clearly visible sinter necks. Both the absence of copper oxide and the presence of sinter necks can explain the five-fold decrease in $R_{m/\mathrm{sh}}$ of vacuum-treated prints versus air-treated prints.

In the next section, we discuss the effect of the temperature of prints treated in a vacuum on the conductivity of the prints.

5.4 The effect of temperature on the resistivity of printed copper particles

Both prints containing 1.5 and 2.5 µm copper particles were treated in a vacuum for 1 h at temperatures ranging from 200 °C to 400 °C. $R_{m/\mathrm{sh}}$ of the prints were determined and top-view SEM images were made. The results are shown in Figure 5.2 below.

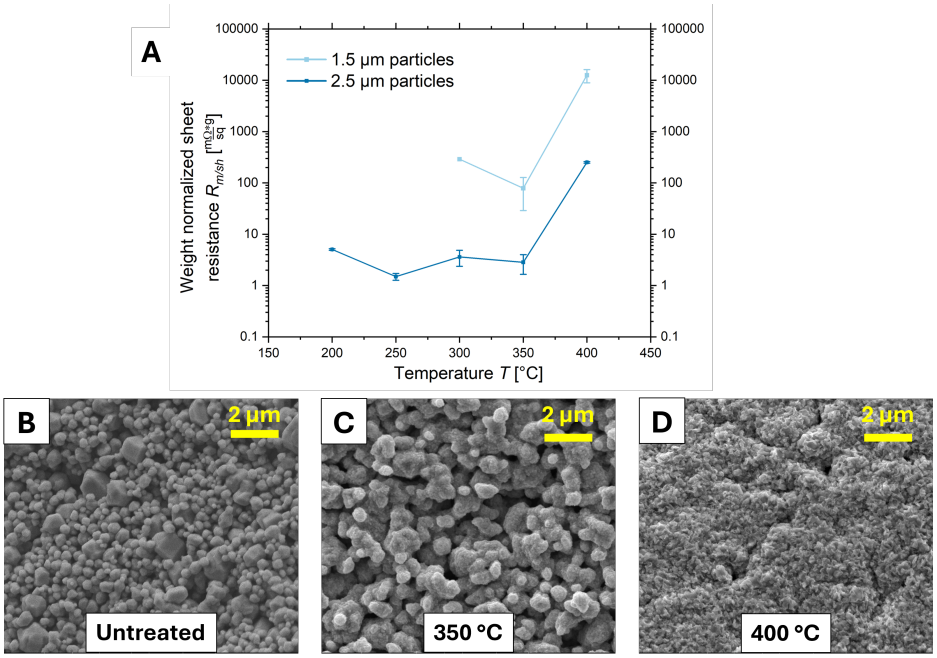

Figure 5.2: Electrical and structural analysis of copper-based prints treated at different temperatures in vacuum. Prints containing 1.5 , and 2.5 µm particles were treated in vacuum at temperatures ranging from 200 °C to 400 °C for 1 h. (A) $R_{m/\mathrm{sh}}$ as a function of temperature. Top-view SEM images of (B) untreated prints, (C) prints treated at 350 , and (D) 400 °C, containing 1.5 µm particles.

The prints containing 2.5 µm copper particles treated at 200 °C to 350 °C showed $R_{m/\mathrm{sh}}$ of 1 $\frac{\mathrm{m}\Omega}{\mathrm{sq}} \cdot \mathrm{g}$ to 10 $\frac{\mathrm{m}\Omega}{\mathrm{sq}} \cdot \mathrm{g}$. Increasing the temperature to 400 °C led to a clear increase by approximately 2 orders of magnitude.

Figure 5.2B shows a top-view SEM image of an untreated print containing 1.5 µm copper particles. The particles had smooth surfaces with clearly defined edges. Particles treated at 350 °C (see Figure 5.2C)

had rougher particle surfaces and sinter necks. The $400\,°C$ treatment strongly changed the structure of the particles (see Figure 5.2D). The particles lost their individual nature and the printed layer turned into a fully dense structure. The rough surface morphology points towards strong oxidation. It appears that at this high temperature, the small oxygen content present in the vacuum oven was sufficient to cause severe oxidation. This severe oxidation explains the large increase in resistance of these prints.

Figure 5.2A shows lower resistances for $2.5\,\mu m$ copper particles at all temperatures. The conductivity of particle-based conductors is usually limited by particle-particle contact resistances [43, 44]. Larger particles have fewer particle-particle contacts, increasing macroscopic conductivity. The $1.5\,\mu m$ particles had an average specific surface area of $1.15\,\frac{m^2}{g}$ compared to $0.55\,\frac{m^2}{g}$ for $2.5\,\mu m$ particles. A consequence of the higher specific surface area of the $1.5\,\mu m$ particles is the increased copper surface that is in contact with air. This can lead to more severe oxidation, increasing individual contact resistances.

In summary, increasing the treatment temperature in vacuum led both to sintering and oxidation of the copper particles. Sintering lowered the resistance, while oxidation increased the resistance. Below $350\,°C$ $R_{m/sh}$ remained stable and above $350\,°C$ the oxidation of copper particles dominated, leading to a strongly increasing $R_{m/sh}$. Larger particles seem to lead to lower resistances due to their lower specific surface area.

5.5 Conclusions

Printed lines of 1.5 and $2.5\,\mu m$ polymer-coated copper particles were treated at elevated temperatures to create conductive prints. Color changes of the samples, EDX, and SEM imaging strongly suggested that the air treatments led to severe oxidation and therefore high resistances of the prints. Treating the samples in a vacuum suppressed oxidation. Increasing the temperature in the temperature range of $200\,°C$ to $350\,°C$ leads to increased sintering, but also to increased oxidation of the particles. As a result, $R_{m/sh}$ stayed between 1 to 10 $\frac{m\Omega}{sq} \cdot g$. The lowest $R_{m/sh}$ of $R_{m/sh} = 1.5\,\frac{m\Omega}{sq} \cdot g$ ($33 \cdot R_{m/sh,Cu}$) was obtained for prints containing $2.5\,\mu m$ copper particles treated at $250\,°C$ in a vacuum for $1\,h$.

Sintering of silver microparticles resulted in $R_{m/sh}$ that were of a factor 8 lower than the best-performing copper-based prints of this chapter. Furthermore, a higher temperature and a vacuum were required for sintering and controlling oxidation, which are both undesirable for industrial applications. Therefore, despite copper's lower price, they cannot yet compete with silver.

In the next chapter, I will discuss the use of silver-coated copper particles in printed conductors and their potential to replace pure silver particles. Silver-coated copper particles need only a small amount of silver, are commercially available, and are approximately a factor 3 cheaper than their pure silver counterpart.

6 Low-temperature sintering of Cu@Ag microparticles in air for recyclable printed electronics

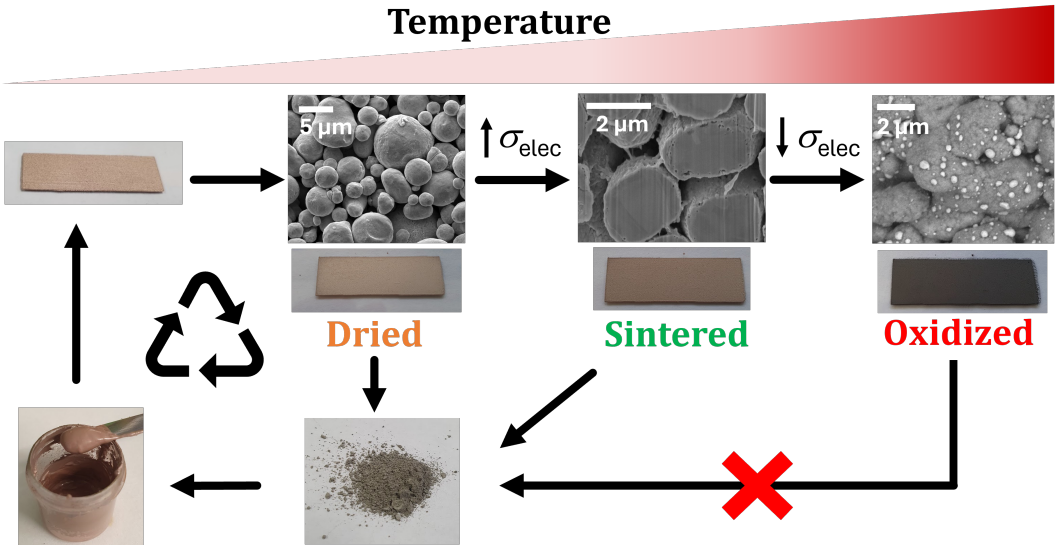

This chapter is based on the content of the article:
D. van Impelen, L. González-García, T. Kraus, Recyclability-by-design of Printed Electronics by Low-Temperature Sintering of Silver Microparticles, Advanced Electronic Materials 2024.
https://doi.org/10.1002/aelm.202400533

The article is licensed under a Creative Commons Attribution 3.0 Unported Licence. Content is reused with permission of the authors.

6.1 Abstract

Silver-coated copper microparticles combine the oxidation resistance of silver with the low cost of copper. They are interesting components for printed conductive structures. We studied whether printed films of such particles can be printed and sintered at low temperatures in air to create highly conductive films and whether it is possible to recover the particles from them for recycling. Pastes containing 1.5 µm to 5 µm spheres and 3 µm flakes with L-ascorbic acid were prepared, screen-printed, and treated at temperatures of 110 °C to 300 °C in air. The bulk resistance of films treated below 160 °C were two orders of magnitude higher than that of bulk copper, ρ_{Cu}, and limited by particle-particle contact resistances. They were reduced by treating the prints at 160 °C to 250 °C, leading to bulk film resistances down to $41\rho_{Cu}$. We demonstrate that the high mobility of silver enables the formation of necks that bridge the copper cores and reduce resistivity in this temperature window. The sintered prints retained their conductivity for at least 6 months. Treatments at higher temperatures in air were detrimental: resistances increased above 250 °C. These temperatures led to dewetting of the silver coating and fast copper oxidation, resulting in a continuously increasing resistance. In a final study, we demonstrated that films treated below 200 °C can be recycled by recovering the metal powder from the printed conductors and that the powder can be printed again.

6.2 Introduction

Copper particle oxidation can be prevented with thin silver coatings. They suppress oxidation at room temperature in air for at least 6 months [71,80]. Choi *et al.* performed thermogravimetry on 2 µm diameter pure copper and silver-coated copper particles in air at 10 °C min^{-1} and found an increase in the onset of oxidation from 148 to 220 °C[171]. Yu *et al.* found an increase for 50 nm diameter copper nanoparticles with and without silver shell from 85 to 157 °C [90]. Dewetting limits the protective effect of silver: Hai *et al.* studied 2 µm diameter silver-coated copper particles with a 260 nm thick silver coating and found that dewetting ensued at 200 °C [89]. The oxidation of the copper core was a result of dewetting, which exposed the copper surface and immediately oxidized in air. Kim *et al.* showed that oxidation can even set in before dewetting [172]. A 100 nm thick copper film coated with a 10 nm silver layer exposed to air at 250 °C formed a Cu_2O phase on top of the silver coating, as revealed by cross-sectional Transmission Electron Microscope (TEM) imaging. Copper atoms diffused through the thin silver layer to form Cu_2O at the air-exposed surface.

Silver-coated copper particles have been used in printed conductive layers [90, 97–104] and to achieve sinter bonding of integrated circuits for power electronics applications [92–96]. Świerzy *et al.* synthesized 1 µm-diameter microparticles with copper cores and 20 nm-thick silver shells [97]. Pastes were formulated, printed, and treated at 250 °C in nitrogen for 15 min to create conductive prints. In later work, the authors used propionic, oxalic, citric, or oleic acid to chemically increase the conductivity of the prints [98]. Kim *et al.* prepared Cu@Ag nanoparticles with diameters ranging from 200 to 900 nm (average diameter of 450 nm) [100]. Pastes containing these particles were screen printed and treated at 200 °C in nitrogen for 60 min to reach 8.2 µΩ · cm. Zhang *et al.* screen-printed elliptic silver-coated nanoflakes that were treated at 150 °C in nitrogen for 2 h and reached 37.5 µΩ · cm [104].

The sintering of silver-coated copper particles has been studied, too. It affects the conductivity of printed layers. Yu *et al.* synthesized 50 nm-sized silver-coated copper particles and sintered them in nitrogen at 350 °C [90]. Dewetting set in at 156 °C, sintering of the silver coating at 200 °C, and sintering of the copper cores at 250 °C. Kim *et al.* sintered 351 nm diameter silver-coated copper particles under isostatic pressure at 350 °C and 10 MPa [173]. The particles formed silver necks before the copper cores started to sinter.

Previous work on printed conductive layers of silver-coated copper particles relied on nitrogen, high temperatures, and/or high isostatic pressures applied on the prints. In this manuscript, we show that low-temperature treatments of such particles can yield relevant conductivities even in ambient air. We used L-ascorbic acid to suppress the oxidation of copper and avoided silver dewetting. We discuss the low-temperature sintering mechanisms that formed conductive silver necks bridging the copper cores. Furthermore, we demonstrate that the weakly sintered particles can be recovered from prints and the recovered powder directly reused.

6.3 Materials and methods

6.3.1 Preparation and printing of pastes

Commercial atomized silver-coated copper spheres (10 % Ag coated Cu-HWQ, Fukuda Metal Foil and Powder Co., Ltd., Japan) with average diameters of 1.5 , 3 , and 5 µm, and commercial atomized silver-coated copper flakes (AgCu 0204C-12 Flake, Ames Goldsmith, United Kingdom) with an average diameter of 3 µm were used to formulate screen printing pastes. The diameter of the flakes was calculated by the manufacturer from laser diffraction results assuming the particles to be spherical. We will refer to this diameter in the remainder of this manuscript as equivalent diameter. The respective dry powder was mixed with ethylene glycol (EG, anhydrous 98 %, Sigma Aldrich) at a weight ratio of 8:1 (Cu@Ag:EG, 1.5 , 3 µm spheres, and flakes) or 8.5:1 (Cu@Ag:EG, 5 µm spheres) using a bladeless mixer (SpeedMixer DAC 150.3 SP, Hauschild, Germany) at 2350 rpm for 3 min, resulting in a highly viscous paste.

Lines of 1×3 cm^2 were screen-printed with a manual screen printer using a mesh of 120 polyester threads per centimeter on microscopy glass slides (VWR, ground edge frosted, Germany). The film thicknesses (average of 3 samples) were measured with a 3D confocal microscope MarSurf CM explorer (Mahr, Germany), and found to be 24.5 ± 1.5 , 38.6 ± 5.3 , and 74.0 ± 7.8 µm (mean $\pm$ standard deviation) for prints containing 1.5 , 3 , and 5 µm diameter coated spheres, and 24.9 ± 0.6 µm for prints of coated flakes. After printing, the samples were immediately placed on a hotplate with closed lit (PZ28-3TD, Präzitherm, Germany) coupled to a PID controller (PR5-3T, Präzitherm, Germany) for 30 min set to the temperatures given in the main text and then cooled down in ambient air. The specified 'spread of temperature' across the hotplate is ± 2 °C, and the lid suppresses convection and ensures minimal surface-normal temperature gradients. Three samples were prepared for each heat treatment. After the heat treatments, the samples were stored in laboratory air where the temperature was kept around 20 °C and humidity below 50 %.

6.3.2 Characterization methods

The internal structures of particles and prints were analyzed using cross sections prepared by creating a trench in prints using a Focused Ion Beam (FEI Versa 3D DualBeam) and imaging using Scanning Electron Microscopy (SEM, Quanta 400 ESEM, Thermo Fisher Scientific GmbH, Germany) with the secondary electron detector.

The electrical conductivities of the printed lines were quantified immediately after the samples had cooled down with a four-point probe set up using a 2450 Sourcemeter (Keithley Instruments, Ohio, USA) using four in-line conical gold pins (GKS-069 201 051 A 0700, Ingun, Germany) with pin-to-pin distances of 1 mm.

Certain samples were electrically characterized *in situ* during the heat treatment using a two-point connection. The printed samples were dried for at least 2 days in vacuum at room temperature and then connected using copper wires at both ends of the printed line using conductive silver paste (G3692, Plano GmbH, Wetzlar, Germany) for the 90 , and $110\,^{\circ}\mathrm{C}$ treatments and conductive epoxy (Duralco 124, high temperature stable conductive silver epoxy from Polytec PT, Karlsbad, Germany) for all other temperature treatments. The epoxy glue was treated in a vacuum for 30 min before the start of the experiment. The samples were connected to a multichannel sourcemeter (DAQ6510 data acquisition logging multi-meter system) equipped with multiplexer cards (7702 40-channel differential multiplexer module with screw terminals) from Keithley Instruments GmbH (Germering, Germany) and mounted on a preheated programmable hot plate using Kapton tape (Plano GmbH, Wetzlar, Germany). A constant voltage bias of 0.1 mV was applied, the current was measured every second, and the resistance from Ohm's Law was recorded for 90 min. We calculated mass-normalized sheet resistances by calculating sheet resistances and multiplying them with the weight of the prints from gravimetry. More details on the mass-normalized sheet resistance are given in the beginning of Section 6.4.1.

X-ray Diffraction (XRD) measurements were performed on either 50 mg of fresh powder or the equivalent of powder scraped off from 3 heat-treated samples using a D8 Advance diffractometer (Bruker, Germany) equipped with a copper source that emitted CuK_α radiation ($\lambda = 1.540\,60$ Å, 40 kV, 40 mA) that we recorded within the 2θ range from 10° to 80°.

Energy-dispersive X-ray spectroscopy was performed using Noran System 7 X-ray Microanalysis System (Thermo Scientific, Germany) mounted inside an SEM (same SEM as described at the start of this section). Three particles per sample were chosen from top-view SEM images at a magnification of 15000X. X-ray spectra were recorded with a zoom-in on the chosen particles at a magnification of 400000X, at a spot size of 4, and an acceleration voltage of 15 kV, and the ratio of the K_α Oxygen: K_α Copper was determined. We report average ratios calculated from the three particles to assess the amount of copper oxide formed during heat treatments.

6.4 Results and discussion

6.4.1 Sintering silver-coated copper particles

We studied the sintering of printed layers of commercial, silver-coated copper microparticles. Electrical characterization of prints is typically done by first determining the sheet resistance,

$$R_{\text{sh}} = \frac{\pi}{\ln(2)} \cdot \frac{\Delta V}{I}, \tag{6.1}$$

where ΔV and I are the potential difference and current between two points of a thin sheet with constant thickness. The sheet resistance is then commonly used to obtain the effective resistivity,

$$\rho = R_{\text{sh}} \cdot t, \tag{6.2}$$

where t is the printed film thickness. The resulting resistivity ρ is an apparent, average value that treats the sheet as a homogeneous conductor.

Note that ρ obtained in this way contains little information on the amount of silver in the sheet. A printed metal layer with a porosity of $10\,\%$ (layer A) can have the same resistivity as a layer with a porosity of $40\,\%$ (layer B) although it contains 1.5 times more metal. This makes it more difficult to compare the amount of metal that has been used and its ecological and economical implications.

A suitable way to directly consider the metal content is to use a mass-normalized sheet resistance,

$$R_{m/\text{sh}} = m * R_{\text{sh}}, \tag{6.3}$$

with m the metal mass of the printed layer. Just like ρ, $R_{m/\text{sh}}$ is a material property that is independent of the layer thickness. Its lowest possible value, $R_{m/\text{sh,Cu}} = 0.045\ \frac{\text{m}\Omega}{\text{sq}} \cdot \text{g}$, is reached when the layer reaches the conductivity of bulk copper. In the following, we provide $R_{m/\text{sh}}$ throughout because it directly shows how to minimize the required amount of metal to obtain maximal conductivities at low temperatures in ambient air.

We used spherical particles (Cu@Ag-S) with average diameters of 1.5 , 3 , and $5\,\mu\text{m}$, and flake-like particles (Cu@Ag-F) with an average diameter of $3\,\mu\text{m}$. Their copper cores were coated with 10 weight percent of silver per total powder mass via electroless plating during production: Cu@Ag-S with 1.5 , 3 , and $5\,\mu\text{m}$ diameter had silver shell thicknesses of 40.8 , 50.5 , and $63.7\,\text{nm}$, Cu@Ag-F had a thickness of $31.3\,\text{nm}$ (see Figure S1 in the supporting information). We added L-Ascorbic Acid (AA) to all paste formulations to suppress copper oxidation during heat treatments of the prints (for more details on the suppressing effect of AA see Figure S2 in the supporting information) [81, 82].

Pastes containing Cu@Ag-S or Cu@Ag-F, Ethylene Glycol (EG), and AA were screen-printed on glass slides into lines and treated at 110 , 160 , 200 , 250 , and $300\,^{\circ}\text{C}$ for $30\,\text{min}$ in air (see Figure 6.1A). The degree of sintering was assessed using Scanning Electron Microscopy (SEM) and electrical characterization.

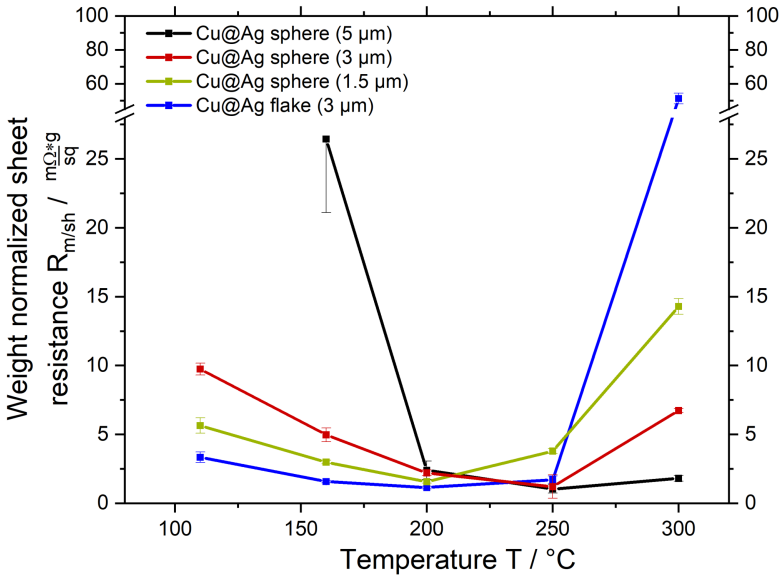

Figure 6.1: Weight-normalized sheet resistances $R_{m/\mathrm{sh}}$ of printed films of silver-copper core-shell particles after 30 min in air at temperature T. All particles contained 10 wt-% of silver as shells. Spherical particles had average diameters of 1.5 , 2.5 , 5 µm. Flakes had an equivalent average diameter of 3 µm.

Figure 6.1A shows that all sheet resistances $R_{m/\mathrm{sh}}$ reached minima at $T_{R,\mathrm{min}}$ that depended on particle diameter and type: $T_{R,\mathrm{min}} \approx 200\,^{\circ}\mathrm{C}$ for 1.5 µm diameter Cu@Ag-S and 3 µm Cu@Ag-F, and $T_{R,\mathrm{min}} \approx 250\,^{\circ}\mathrm{C}$ for 3 and 5 µm Cu@Ag-S. The existence of an optimal sintering temperature is in stark contrast to pure silver particles, where increasing temperature at constant treatment time reduces resistance at least until 300 °C, and no resistance increase is observed when further increasing the temperature.

The decrease of $R_{m/\mathrm{sh}}$ at 110 to 200 °C, below $T_{R,\mathrm{min}}$, is likely caused by silver that is mobile at low temperatures. The observation is consistent with many reports on the necking of pure silver microparticles at 150 °C or below (cf. introduction). We argue that a similar necking occurs between the shells of silver-coated copper particles [90, 173, 174], with the expected reduction of electrical resistance.

The increasing $R_{m/\mathrm{sh}}$ at $T > T_{R,\mathrm{min}}$ is most likely caused by the oxidation of copper. Literature reports that the silver films on copper start dewetting above 200 °C and expose copper surface [89, 91, 172]. Unprotected copper immediately reacts with ambient oxygen to form a native oxide layer even at room temperature. Above 150 °C, oxygen can diffuse through this native oxide, making the oxide layer thicker (cf. introduction). Copper oxides are insulating and likely increase $R_{m/\mathrm{sh}}$.

We evaluated this hypothesis and studied the formation of copper oxides at $T > T_{R,\mathrm{min}}$ using X-ray Diffraction (XRD) and Energy Dispersive X-ray spectroscopy (EDX) in the following.

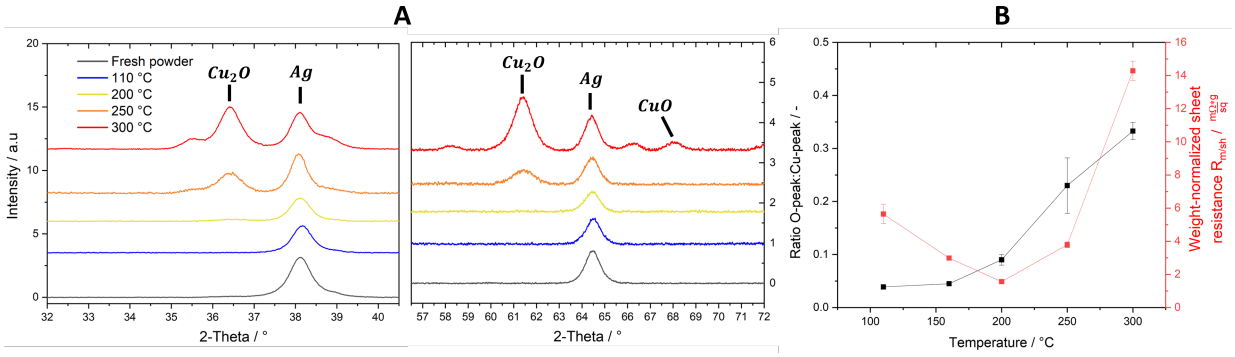

Figure 6.2: Oxidation of silver-coated copper particles after heat treatments in air quantified by (A) X-Ray Diffraction (XRD) and (B) Energy Dispersive X-ray spectroscopy (EDX). (A) Prints containing 1.5 µm Cu@Ag-S treated at 110 , 200 , and 300 °C. Characteristic peaks of Cu, Ag CuO, and Cu_2O are indicated in the graph. (B) The temperature-dependent ratio of the K_α oxygen to the K_α copper reflex intensities (black line) and the normalized resistances $R_{m/\text{sh}}$ (red line) from EDX are shown for prints of 1.5 µm Cu@Ag-S.

6.4.2 Oxidation and dewetting effects

We recorded X-ray Diffraction (XRD) patterns of fresh powders and prints containing 1.5 µm Cu@Ag-S treated at 110 , 200 , 250 , and 300 °C (Figure 6.2A). Silver has characteristic diffraction reflexes at 38 and 64.5° [172], hence the maxima observed at these positions were assigned to the silver coating of the particles.

Copper oxide peaks only formed at 250 °C and above, where Cu_2O caused reflexes at $2-Theta = 36.4°$ and 61.5° [175]. They increased in intensity at 300 °C, and new peaks appeared indicating the formation of a CuO phase ($2-Theta = 66.2°$ and 68°). This oxidation sequence is in line with literature on copper particle oxidation in air [72, 75].

Additional Energy-Dispersive X-ray analysis (EDX) was used to detect oxides. The ratio of the K_α emission of oxygen and L_α emission of copper (details in the experimental section) are shown in Figure 6.2B. The oxide fraction clearly correlated with the corresponding $R_{m/\text{sh}}$ at higher temperatures. It increased at 200 °C, already before XRD indicated a crystalline copper phase, suggesting the formation of amorphous oxide layers and consistent with literature [176]. The strong increase of the EDX ratio at 250 °C is consistent with the oxide seen by XRD.

The stability of silver-coated copper particles towards oxidation at elevated temperatures is limited by the dewetting of the silver coating (cf. introduction). We observed dewetting in electron microscopy by exploiting the Backscattered Electron (BSE) contrast caused by the atomic number difference between Ag and Cu. Figure 6.3 shows top-view BSE images of prints containing Cu@Ag-F treated for 30 min at 200 , 250 , and 300 °C.

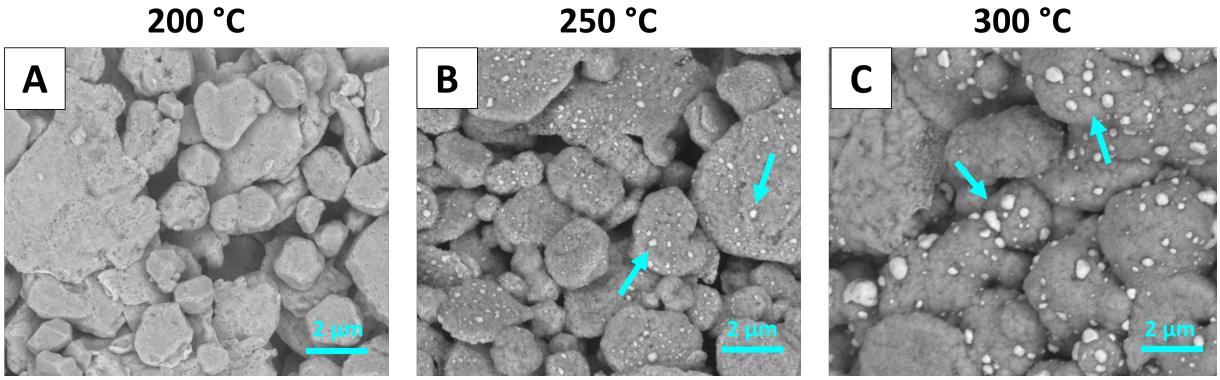

Figure 6.3: Dewetting of silver coatings on core-shell copper particles. Top-view BSE images of prints containing Cu@Ag-F treated at (A) 200 , (B) 250 , and (C) 300 °C. Silver droplets that formed by dewetting are indicated with the blue arrows in (B) and (C).

The Cu@Ag-F in Figure 6.3A that were treated at 200 °C had no visible contrast on their surfaces, indicating homogeneous silver coatings. Treatment at 250 °C caused dewetting and clearly contrasting silver droplets visible in Figure 6.3B. They coincided with the formation of Cu_2O detected by XRD, suggesting that dewetting preceded oxidation, as reported in literature [75]. The silver droplets were larger at 300 °C (Figure 6.3C), exposing more copper, and causing stronger oxidation as detected by XRD and EDX (see above).

Having established that dewetting leads to oxidation at temperatures above $T_{R,\mathrm{min}}$, we now analyze in detail how different treatment temperatures (below, at, and above $T_{R,\mathrm{min}}$) affect $R_{m/\mathrm{sh}}$ over time and propose a mechanism for the low-temperature sintering of silver-coated particles.

6.4.3 Sintering mechanism of silver-coated copper particles

We followed the evolution of $R_{m/\mathrm{sh}}$ *in situ* while sintering 3 µm Cu@Ag-S. Layers with a thickness of 38.6 ± 5.3 µm were printed and dried in vacuum at room temperature for 24 h. The evolution of $R_{m/\mathrm{sh}}$ was then followed via two electrical contacts during 90 min at 90 , 110 , 160 , 200 , or 300 °C. Figure 6.4A shows the results.

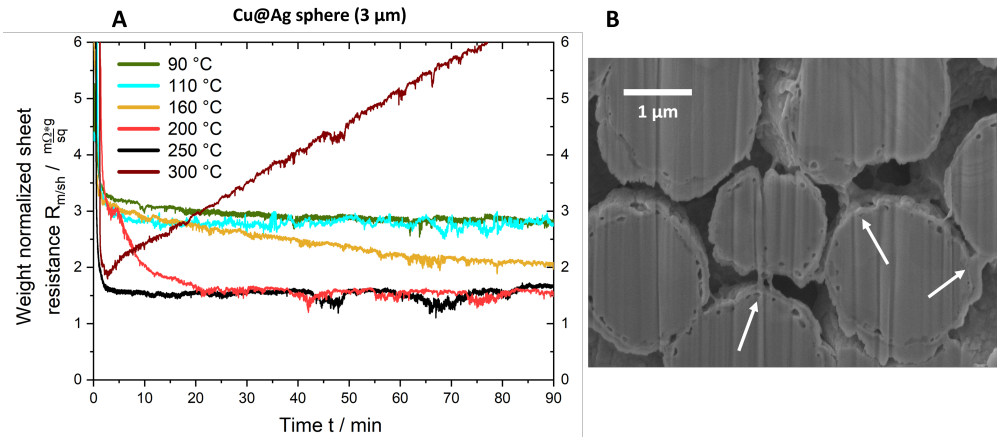

Figure 6.4: (A) Resistance evolution of prints and (B) micro-structural changes at 200 °C. (A) $R_{m/\mathrm{sh}}$ as measured *in situ* while treating different prints of 3 µm-sized Cu@Ag-S treated at 90 °C to 300 °C for 90 min. The measurement started at 0 min when placing the sample on a preheated hot plate. (B) Electron microscopy of a cross-section prepared from a sample treated at 200 °C indicated silver necks (white arrows).

Resistances dropped to a plateau value of 3 $\frac{\mathrm{m\Omega}}{\mathrm{sq}} \cdot \mathrm{g}$ in the first 5 min for90 and 110 °C and remained there for the remainder of the experiment. Higher temperatures led to lower plateau values that decreased from 2 $\frac{\mathrm{m\Omega}}{\mathrm{sq}} \cdot \mathrm{g}$ at 160 °C to 1.5 $\frac{\mathrm{m\Omega}}{\mathrm{sq}} \cdot \mathrm{g}$ at 200 and 250 °C. At 300 °C, above $T_{R,\mathrm{min}}$, $R_{m/\mathrm{sh}}$ reached a minimum after 3 min and then increased linearly during the entire temperature treatment.

The reduction of $R_{m/\mathrm{sh}}$ in the range of 110 °C to 250 °C suggests the formation of silver necks that are connecting the particles. Scanning Electron Microscopy (SEM) images of a cross-section taken after 90 min at 200 °C (Figure 6.4B) confirmed the existence of such necks. Note that the silver shell remained continuous: no dewetting was visible at a temperature of 200 °C (see Figure 6.3A).

The continuous increase of $R_{m/\mathrm{sh}}$ observed at $T = 300\,^{\circ}\mathrm{C}$ is related to silver dewetting and copper oxidation. The onset of dewetting at 250 °C leads to the formation of Cu_2O (cf. oxidation and dewetting effects), but not necessarily to an increase of $R_{m/\mathrm{sh}}$, as the trace for 250 °C Figure 6.4A shows. The constant $R_{m/\mathrm{sh}} = 1.5\,\frac{\mathrm{m\Omega}}{\mathrm{sq}} \cdot \mathrm{g}$ is likely caused by silver necks that keep the copper cores electrically contacted and are not affected by oxide formation at other, exposed parts of the spheres. This mechanism fails at 300 °C, where both copper oxidation and dewetting are more rapid. The copper cores expand upon oxidation, inducing stresses and mechanical fracture of silver necks. Concurrently, the copper-silver interface within the particles becomes insulating, reducing the conductive pathways. Other mechanisms are likely to contribute: Hai *et al.* demonstrated that the diffusion of copper through the silver coating of particles leads to the formation of pores at the copper-silver interface that reduces conductivity. Such pores formed at and above 250 °C, too (see Figure S3 of the supporting information).

Figure 6.5 summarizes the proposed sintering processes of silver-coated copper particles in air. Temperatures below 160 °C did not lend silver sufficient mobility to form sinter necks, and $R_{m/\mathrm{sh}}$ remained limited by the particle-particle contact resistances to 3 $\frac{\mathrm{m\Omega}}{\mathrm{sq}} \cdot \mathrm{g}$ to 6 $\frac{\mathrm{m\Omega}}{\mathrm{sq}} \cdot \mathrm{g}$. Temperatures of $160 - 250\,^{\circ}\mathrm{C}$ mobilized the silver sufficiently to form necks connecting the particles, but retained the continuity of the shells that protect the copper from oxidation. They reduced $R_{m/\mathrm{sh}}$ to 1 $\frac{\mathrm{m\Omega}}{\mathrm{sq}} \cdot \mathrm{g}$ to 1.5 $\frac{\mathrm{m\Omega}}{\mathrm{sq}} \cdot \mathrm{g}$ ($6.9 \times 10^{-5}\,\Omega \cdot \mathrm{cm}$ to $9.1 \times 10^{-5}\,\Omega \cdot \mathrm{cm}$). A combination of dewetting and rapid copper oxidation at temperatures above 250 °C led to a continuously increasing $R_{m/\mathrm{sh}}$.

The mechanisms illustrated in Figure 6.5 explain the optimal sintering temperature $T_{R,\mathrm{min}}$ for the core-shell particles that does not exist for homogeneous silver spheres.

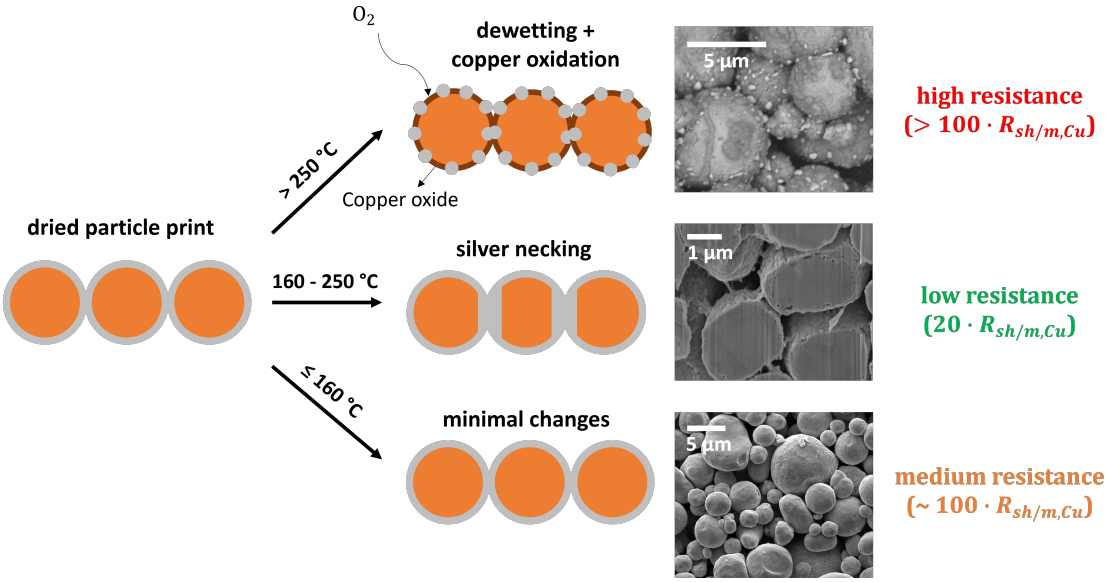

Figure 6.5: Proposed sintering mechanisms of silver-coated copper particles in air. Temperatures below 160 °C hardly affected the silver coating, sheet resistances remained at $R_{m/\mathrm{sh}} \approx 10^2 \cdot R_{m/\mathrm{sh,Cu}}$, and the particles appeared unchanged in electron microscopy (shown here: 5 µm Cu@Ag-S at 110 °C). Temperatures between 160 and 250 °C reduced $R_{m/\mathrm{sh}}$ to $\approx 20 \cdot R_{m/\mathrm{sh,Cu}}$ and caused neck formation (shown here: 3 µm Cu@Ag-S treated at 200 °C). Temperatures above 250 °C increased $R_{m/\mathrm{sh}}$ to above $10^2 \cdot R_{m/\mathrm{sh,Cu}}$ and caused dewetting and oxidation (shown here: 5 µm Cu@Ag-S treated at 300 °C).

We assessed the stability of prints by storing them under ambient conditions for 6 months. Figure 6.6 illustrates that the $R_{m/\mathrm{sh}}$ of prints of 3 µm Cu@Ag-S underwent no significant changes, indicating that the samples were stable.

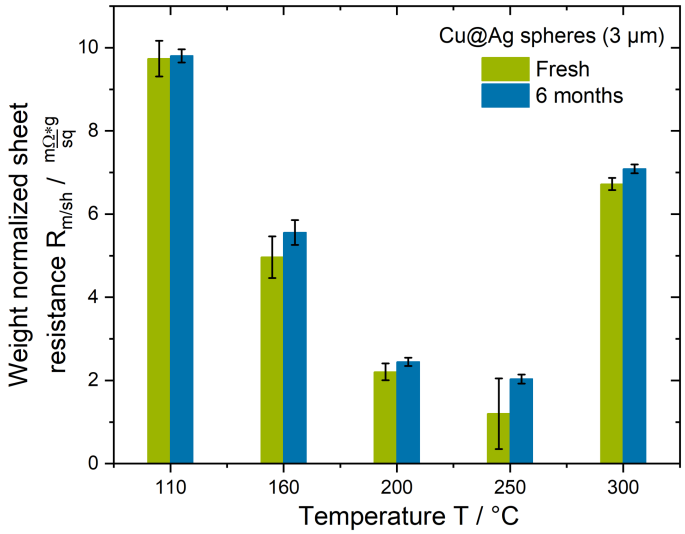

Figure 6.6: Stability of weakly sintered prints under ambient conditions. $R_{m/\mathrm{sh}}$ of prints containing 3 µm-sized Cu@Ag-S after sintering ('fresh') and after 6 months storage in laboratory air at standard conditions (cf. Preparation and printing of pastes.)

6.4.4 Recyclability

We demonstrated that prints of silver-coated copper spheres and flakes consistently decrease in electrical resistance $R_{m/\mathrm{sh}}$ with increasing temperature until a certain temperature. Treatments at higher temperatures increased the resistance. Prints containing Cu@Ag-F resulted in the lowest $R_{m/\mathrm{sh}}$ for treatments below 200 °C. We chose these films to study the recovery of metal powders from the prints. The redispersion of the particles could simplify the recovery and recycling of metal particles from printed electronics (cf. Introduction).

The cycle of making paste, printing, and recycling of metal powder is shown in Figure 6.7A. We prepared prints containing Cu@Ag-F that were treated at three different temperatures. Pastes were printed on glass slides, put in a vacuum at room temperature for 2 days, 80 °C for 30 min, or 160 °C for 30 min. The $R_{m/\mathrm{sh}}$ of these prints are shown as 'first generation' in the green bars in Figure 6.7B. The prints were then mechanically removed, powder was collected, and new pastes were made from them. Lines were printed on glass slides and treated identically to the first-generation prints that they came from. The $R_{m/\mathrm{sh}}$ for these 'second generation' prints are shown as blue bars in Figure 6.7B.

The $R_{m/\mathrm{sh}}$ of first-generation prints decreased with increasing temperature as discussed in the preceding sections. The $R_{m/\mathrm{sh}}$ of all second-generation prints were larger than the respective first-generation prints. We propose that this degradation reflects copper exposure or thinning of the silver coating due to fracturing particle-particle contacts. Exposed and thinned silver coating causes native oxide growth at room temperature [72–74]. Second-generation prints contain more particle-particle contacts with an oxide layer that cause large contact resistances, leading to larger overall $R_{m/\mathrm{sh}}$. This is consistent with the small increase in $R_{m/\mathrm{sh}}$ for second-generation prints that were treated in a vacuum at room temperature. The mobility of silver at room temperature is too low for silver to migrate much, leading to a silver

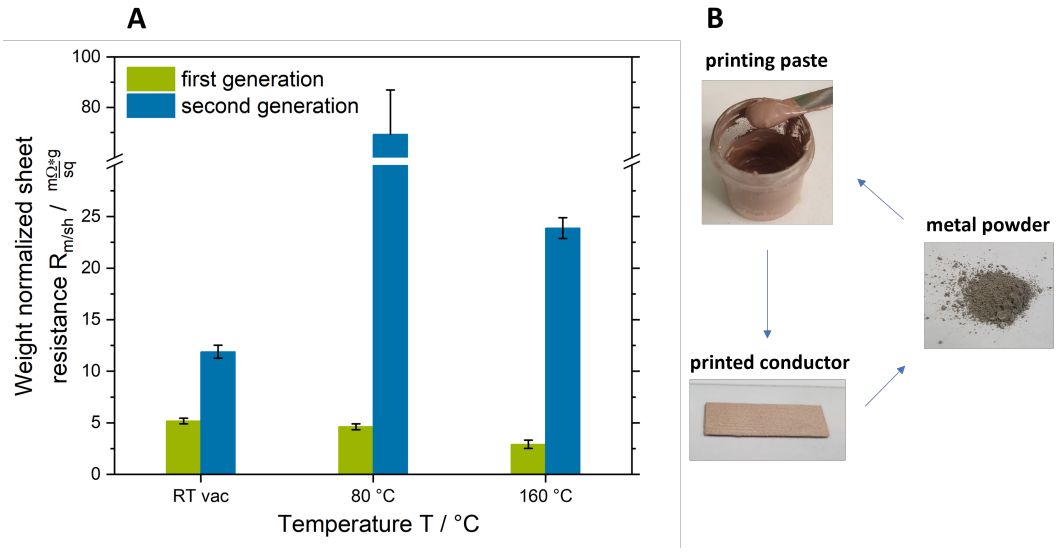

Figure 6.7: Recyclability of prints of silver-copper core-shell particles after three different heat treatments. (A) Circular paste preparation, printing, and recycling. (B) Electrical performance of freshly printed Cu@Ag-F compared to prints made from recycled Cu@Ag-F after vacuum drying at room temperature for 2 days, thermal treatment at 80 °C for 30 min, and sintering at 160 °C for 30 min. Green bars indicate fresh prints and blue bars indicate recycled prints.

coating that stays intact even after recycling of the particles.

In summary, it was possible to recycle weakly sintered Cu@Ag-F from prints, but the performance of the material degraded. Heat treatments at 160 °C reduced $R_{m/\text{sh}}$ of the first generation to 2.9 $\frac{\text{m}\Omega}{\text{sq}} \cdot \text{g}$ ($1.46 \times 10^{-4}\,\Omega \cdot \text{cm}$) but increased $R_{m/\text{sh}}$ of the second generation of prints by a factor of 8. Limiting the first-generation treatment to room temperature increased $R_{m/\text{sh}}$ to 5.2 $\frac{\text{m}\Omega}{\text{sq}} \cdot \text{g}$ ($2.72 \times 10^{-4}\,\Omega \cdot \text{cm}$) for the first generation but limited the increase in the second generation to a factor of 2.

6.5 Conclusion

We prepared conductive films from silver-coated copper spheres (Cu@Ag-S) and flakes (Cu@Ag-F) and treated them at low temperatures in air. The mass-normalized sheet resistances $R_{m/\text{sh}}$ of all prints decreased with increasing temperatures below $T_{R,\text{min}}$ that depended on the particle type and reached a minimal $R_{m/\text{sh}}$ of 1 $\frac{\text{m}\Omega}{\text{sq}} \cdot \text{g}$ to 1.5 $\frac{\text{m}\Omega}{\text{sq}} \cdot \text{g}$ ($6.9 \times 10^{-5}\,\Omega \cdot \text{cm}$ to $9.1 \times 10^{-5}\,\Omega \cdot \text{cm}$). Treatments at $T > T_{R,min}$ increased $R_{m/\text{sh}}$.

A combination of in-situ electrical characterization and cross-section SEM imaging revealed that the dropping $R_{m/\text{sh}}$ below $T_{R,\text{min}}$ is a result of low-temperature silver sintering. A pronounced drop in $R_{m/\text{sh}}$ appeared only above 160 °C. This characteristic drop was linked to the formation of silver necks that were identified by cross-sectional SEM imaging.

Dewetting and oxidation were identified as the mechanisms increasing $R_{m/\text{sh}}$ at $T > T_{R,min}$. BSE imaging revealed the onset of silver dewetting at 250 °C. Exposed copper areas and locally thinning silver coatings enabled the formation of Cu_2O as confirmed by XRD. The combination of rapid oxidation of exposed copper and the dewetting of particles led to a continuously increasing $R_{m/\text{sh}}$ at and above 250 °C.

The choice of sintering temperature is crucial to obtaining highly conductive prints of silver-coated copper particles. Temperatures below $160\,^{\circ}\mathrm{C}$ do not lead to sintering and limit $R_{m/\mathrm{sh}}$ to $3\,\frac{\mathrm{m}\Omega}{\mathrm{sq}}\cdot\mathrm{g}$ to $6\,\frac{\mathrm{m}\Omega}{\mathrm{sq}}\cdot\mathrm{g}$. Temperatures above $250\,^{\circ}\mathrm{C}$ increase $R_{m/\mathrm{sh}}$ by oxidation and reduced silver necking. Sintering at $160\,^{\circ}\mathrm{C}$ to $250\,^{\circ}\mathrm{C}$ minimizes $R_{m/\mathrm{sh}}$ to minimal values in the range of $1\,\frac{\mathrm{m}\Omega}{\mathrm{sq}}\cdot\mathrm{g}$ to $1.5\,\frac{\mathrm{m}\Omega}{\mathrm{sq}}\cdot\mathrm{g}$ ($6.9\times10^{-5}\,\Omega\cdot\mathrm{cm}$ to $9.1\times10^{-5}\,\Omega\cdot\mathrm{cm}$).

We tested the recovery of weakly sintered prints of silver-coated copper particles. The first-generation prints were treated and removed from the substrate to recover powders that were formulated as second-generation pastes. The second-generation prints consistently had a higher $R_{m/\mathrm{sh}}$ than the respective first-generation prints. We found a trade-off: room temperature drying of prints limited electrical degradation after recycling to a factor of 2 while $160\,^{\circ}\mathrm{C}$ let to a factor of 8. Depending on the application, it is possible to enable recycling by minimizing sintering temperature at the cost of conductivity.

Author Contributions

David van Impelen wrote the original draft of the manuscript and performed all experiments. All authors took part in the conceptualization, reviewing and editing of the manuscript. Tobias Kraus and Lola González-García were leading the supervision. Tobias Kraus was responsible for the funding acquisition and resources.

Conflicts of interest

There are no conflicts of interest to declare.

Acknowledgements

We acknowledge Dominik Perius for his preparation of printed layer cross-sections via FIB-SEM and Albenc Nexha for X-ray diffraction analyses. This work was supported by the German Federal Foundation for the Environment (DBU). We thank Jochen Wahl (CEO of GSB Wahl GmbH) for his contributions to discussions on low-impact conductive pastes.

7 Summary and conclusions

In Section 2.9, I presented four knowledge gaps in the state of the art of metal-based, printed conductors. In this section, I will discuss in detail how we contributed to closing these knowledge gaps through the work presented in Chapters 3 to 6 of this thesis.

7.1 Gap 1: Low-temperature sintering mechanisms of silver microparticles

To formulate a hypothesis on the low-temperature sintering mechanism of silver microparticles, we studied the sintering and its effect on the conductivity of two different types of silver microparticles: surfactant-containing precipitated- and surfactant-free atomized particles. The results are described in Chapter 3 of this thesis. In the following, I sum up our major findings of this chapter regarding the low temperature sintering of silver microparticles, which in the end led to our current understanding of the mechanism:

- **Sintering of silver microparticles involves ion formation and precipitation, which occurs at lower temperatures than classical sintering.** We demonstrated that silver microparticles release ions and the ion concentration in printed pastes increases upon heating until a critical concentration for nucleation is reached. At this concentration, heterogeneous nucleation results in sinter neck formation and homogeneous nucleation in nanoparticle formation.
- **Precipitated particles sinter at a lower temperature than atomized particles.** The resistance of prints was tracked *in situ* at temperatures ranging from 110 °C to 300 °C. Above a certain minimum temperature, we could identify a drop in resistance, with a defined onset time, which we linked to the sintering of the particles. We defined this temperature as the onset temperature of sintering. Precipitated particles had an onset temperature of 140 °C, compared to 275 °C for atomized particles. We demonstrated with inductively coupled plasma (ICP) measurements that this was related to the increased ionic silver release during the sintering of precipitated particles.

Our hypothesis on the low-temperature sintering of silver microparticles explains the *in-situ* formation of silver nanoparticles during sintering, which has been observed in multiple studies in literature [13, 62–64]. Unlike these studies have suggested, our mechanism proposes that the nanoparticles are not aiding the sintering. Instead, heterogeneous nucleation causes the formation of necks at low temperatures. Furthermore, we could link our hypothesis to differences that were observed for sintering different particle types (atomized versus precipitated).

7.2 Gap 2: The best of two worlds: Sintering and recycling

Chapter 3 introduced a recyclability-by-design method that allowed for the recycling and reusing of weakly sintered silver microparticles. In Chapter 4, I used this method to compare the differences in the recycling of flakes versus spheres. In the points below I highlight our findings on the recycling of weakly sintered particles and their contribution to the current state of the art.

- **There is a trade-off between sintering and recycling of silver microparticles.** In Chapter 3, silver microparticles were sintered at $150\,^{\circ}\mathrm{C}$ for 20 , 40 , and $60\,\mathrm{min}$. $R_{m/\mathrm{sh}}$ of the prints decreased with increasing sintering time. The powder was recovered from the prints and sintered agglomerates were broken up through tip-sonication. With increasing sintering time, the recovery percentage of powder decreased from $99\,\%$ to $48\,\%$, and finally to $6\,\%$. SEM imaging revealed that the neck sizes increased with increasing sintering time, which led to unbreakable necks and a decreased recovery percentage. We found a trade-off: increasing the sintering time leads to an increased conductivity, but lowers the recyclability of the particles.
- **Prints made from recycled particles consistently resulted in a lower resistance than prints made from untreated particles.** For example, initial prints treated for $40\,\mathrm{min}$ at $150\,^{\circ}\mathrm{C}$ resulted in a $R_{m/\mathrm{sh}} = 7.7\,\frac{\mathrm{m}\Omega}{\mathrm{sq}} \cdot \mathrm{g}$. After recycling and reusing the particles from these prints, new prints were made and again treated for $40\,\mathrm{min}$ at $150\,^{\circ}\mathrm{C}$. These recycled prints had a $R_{m/\mathrm{sh}} = 0.4\,\frac{\mathrm{m}\Omega}{\mathrm{sq}} \cdot \mathrm{g}$, a factor 19 lower than the initial prints. We propose that this difference comes from the presence of small sintered agglomerates present in the recycled powder. They are small enough to not cause problems with clogging during screen-printing, but large enough to enhance the conductivity of recycled prints. SEM imaging revealed the presence of such agglomerates in the recycled powder.
- **The trade-off between sintering and recycling is less pronounced for flakes than for spheres.** In Chapter 4, I compared flakes and spheres. The reusable fraction of recovered powder was consistently higher for flakes than it was for spheres. For example, after a heat treatment $140\,^{\circ}\mathrm{C}$ for $30\,\mathrm{min}$, $91.6\,\%$ of the recovered flakes could be reused for a new generation of prints, while for spheres this was only $69.7\,\%$. Increasing the temperature to $160\,^{\circ}\mathrm{C}$ decreased these percentages to $44.7\,\%$ and $33.2\,\%$ for flakes and spheres, respectively. We propose that the higher porosity of prints based on flakes resulted in an easier breakup of agglomerates and thus higher recovery percentages.

Before, recycling and reusing of silver particles from printed conductors was only demonstrated for printed conductors with relatively high resistances due to the absence of particle sintering [22, 106]. To our knowledge, we are the first to demonstrate the recycling and reusing of sintered silver particles. This approach combines the high conductivity and recyclability of silver-based printed conductors and contributes to the development of more sustainable printed electronics.

7.3 Gap 3: Flakes versus spheres

To make a comparison between flakes and spheres, we considered three main aspects: the sintering, the conductivity at different treatment temperatures, and the recyclability at different treatment temperatures. In the previous section, we already saw that flakes had a better recyclability compared to spheres. In this section, I will discuss the differences observed in terms of sintering and conductivity at different treatment temperatures. These were the main findings:

- **At treatment temperatures below $160\,^{\circ}\mathrm{C}$, flakes result in a lower $R_{m/\mathrm{sh}}$ than spheres.** At $110\,^{\circ}\mathrm{C}$, both the flakes and the spheres don´t yet form sinter necks, and conductivity stems from a percolating path of particles in contact with eachother. The resistance of such prints is dominated by the particle-particle contact resistances [33–35]. Flakes have larger overall particle-particle contact areas, which reduces the overall contact resistances and thus, $R_{m/\mathrm{sh}}$ [64].
- **At $200\,^{\circ}\mathrm{C}$ and above, $R_{m/\mathrm{sh}}$ of spheres is a factor 2 lower than the flakes.** Increasing the temperature changes the picture. At $200\,^{\circ}\mathrm{C}$ the prints based on spheres become more conductive, and they remained more conductive at higher temperatures, as well. At $300\,^{\circ}\mathrm{C}$, $R_{m/\mathrm{sh}}$ of prints based on flakes and spheres was a factor 4 and 2 higher than that of bulk silver. We propose that both the small grain size (below $50\,\mathrm{nm}$) and internal morphology of the printed structures explain the higher $R_{m/\mathrm{sh}}$ compared to the bulk silver reference. However, the higher $R_{m/\mathrm{sh}}$ of flake-based prints must stem from differences in the internal structure, since the grain sizes of sintered flakes and spheres are comparable. We made 3D reconstructions of prints based on flakes and spheres treated at $300\,^{\circ}\mathrm{C}$ for $30\,\mathrm{min}$ and determined tortuosity factors. A higher tortuosity factor indicates higher constriction resistances, thus higher $R_{m/\mathrm{sh}}$ of the prints. The sintered flakes had a higher tortuosity factor, which can explain their higher $R_{m/\mathrm{sh}}$.

In summary, sintered flakes result in higher recycling yields than sintered spheres. Sintered sphere prints, however, have a lower porosity and therefore a factor 2 lower mass-normalized sheet resistance than sintered flake prints.

7.4 Gap 4: Copper-based printed conductors

In this thesis, I discussed two strategies for making copper-based printed conductors. The first strategy involved a combination of polymer-coated copper particles with L-Ascorbic Acid to suppress copper oxidation. Chapter 5 is dedicated to this strategy. The second strategy involved exploiting both the oxidation resistance of silver and the low cost of copper by making use of silver-coated copper particles. This strategy was combined with the use of L-Ascorbic Acid and the results were discussed in Chapter 6. Below we list the most important findings of Chapter 5.

- **Sintering polymer-coated copper particles at $200\,^{\circ}\mathrm{C}$ in ambient air leads to high resistances due to oxidation.** We treated printed pastes containing polymer-coated copper particles and L-ascorbic acid at a temperature of $200\,^{\circ}\mathrm{C}$ for $2.5\,\mathrm{h}$. With Energy Dispersive X-ray (EDX) analysis, we compared the ratio of K_α oxygen to K_α copper reflex intensities of both untreated particles and the heat-treated particles. The ratio was about a factor of 3 higher for the heat-treated particles, indicating that the treatment resulted in copper oxidation. The prints also turned black, which is the color of CuO, indicating that oxidation occurred. As a result, $R_{m/\mathrm{sh}}$ was high (about 9 orders of magnitude larger than $R_{m/\mathrm{sh,Cu}}$).
- **Sintering the particles in vacuum at $200\,^{\circ}\mathrm{C}$ suppresses oxidation and reduces $R_{m/\mathrm{sh}}$ by 5 orders of magnitude.** In an attempt to suppress the oxidation of copper, we did the same treatment in vacuum. This time, the ratio of K_α oxygen to K_α copper reflex intensities did not change after the heat treatment, nor did the color change. These results indicated that we could successfully suppress the oxidation in this case. Consequently, $R_{m/\mathrm{sh}}$ decreased 5 orders of magnitude.
- **Larger copper particles are more resistant to oxidation than smaller particles.** I prepared prints containing $1.5-$ and $2.5\,\mu\mathrm{m}$ copper particles and treated the prints at temperatures ranging from $200\,^{\circ}\mathrm{C}$ to $400\,^{\circ}\mathrm{C}$ in vacuum. $R_{m/\mathrm{sh}}$ of prints containing $2.5\,\mu\mathrm{m}$ particles were consistently lower. We propose that the lower specific surface area leads to lower particle-particle contact resistances and therefore to a lower $R_{m/\mathrm{sh}}$. Additionally, the lower specific surface area means less copper-air interface area and hence less oxidation.

The results above demonstrate that printed conductors based on polymer-coated copper, even when L-ascorbic acid is used for oxidation suppression, require the heat treatments to be in vacuum. The necessity of using a vacuum strongly decreases the appeal of such printed conductors, which motivated us to switch to an alternative copper-based printed conductor that can be treated in ambient air. For this purpose, we investigated the use of silver-coated copper particles, which has been presented in Chapter 6. The main findings are listed below:

- **Silver-coated copper particles have an optimum treatment temperature ($T_{R,\mathrm{min}}$) at which $R_{m/\mathrm{sh}}$ is the lowest.** We prepared prints of silver-coated copper flakes (average diameter $3\,\mu\mathrm{m}$ and spheres (average diameters of 1.5 , 3 , and $5\,\mu\mathrm{m}$), and treated them in air at temperatures ranging from $110\,^{\circ}\mathrm{C}$ to $300\,^{\circ}\mathrm{C}$ for $30\,\mathrm{min}$. Interestingly, the prints had an optimum treatment temperature at which $R_{m/\mathrm{sh}}$ was the lowest. Above this temperature, $R_{m/\mathrm{sh}}$ of prints increased. This is in stark contrast to what we have seen for silver particles, where $R_{m/\mathrm{sh}}$ either decreases or remains the same upon increasing the treatment temperature. Aditional, we found that $T_{R,\mathrm{min}}$ was the highest

for the particles with the lowest specific surface area (3 , and 5 µm spheres). We propose this is related to the silver shell, which was thicker for these particles.

- **Increasing the treatment temperature from $110\,^{\circ}\mathrm{C}$ to $T_{R,\mathrm{min}}$ leads to a continuously decreasing $R_{m/\mathrm{sh}}$ due to the formation of silver sinter necks.** In Chapter 3, we have seen that the onset temperature of sintering of silver microparticles was around $140\,^{\circ}\mathrm{C}$. This demonstrated that silver can form necks at such low temperatures. It is therefore likely that the silver coating of silver-coated copper particles is highly mobile and can form necks with adjacent particles. We attribute the decreasing of $R_{m/\mathrm{sh}}$ until $T_{R,\mathrm{min}}$ to the sinter neck formation of the coated particles. For particles treated at $200\,^{\circ}\mathrm{C}$ we confirmed the formation of silver necks by means of cross-sectional SEM imaging.
- **Temperatures above $T_{R,\mathrm{min}}$ increased $R_{m/\mathrm{sh}}$ caused by dewetting of the silver shell, followed by oxidation of the copper cores.** To explain why $R_{m/\mathrm{sh}}$ increases above $T_{R,\mathrm{min}}$, we performed EDX, XRD, and BSE imaging of the heat-treated particles. The EDX analysis confirmed that oxide started to form at $200\,^{\circ}\mathrm{C}$, while XRD first detected a $\mathrm{Cu_2O}$ phase at $250\,^{\circ}\mathrm{C}$. BSE imaging of coated flakes revealed that the onset temperature of dewetting occurred at $250\,^{\circ}\mathrm{C}$.
- **Silver-coated copper particles can be recycled and reused for a new generation of prints.** We used the recycling approach introduced in Chapter 3 to assess the recyclability of silver-coated copper particles. Prints of silver-coated copper flakes that we only dried in vacuum, treated at $80\,^{\circ}\mathrm{C}$, and treated at $160\,^{\circ}\mathrm{C}$ could all be recycled and reused for a new generation of prints. Unlike the prints from recycled silver particles, these recycled prints resulted in a higher $R_{m/\mathrm{sh}}$ compared to the initial prints. This increase could be minimized by keeping the treatment temperature low (or even only vacuum), however, this was at the cost of the conductivity of the initial prints. Hence, there is a choice to be made: high conductivity of initial prints at the cost of losing conductivity for recycled prints or minimizing conductivity loss of recycled prints by accepting a lower conductivity of the initial prints.

Most literature studies that fabricated printed conductors based on silver-coated copper particles made use of inert gas or vacuum during the sintering procedure [90, 97–104]. We demonstrated that in combination with L-ascorbic acid, silver-coated copper particles can also reach high conductivities at moderate temperatures in ambient air conditions. Furthermore, we found that silver-coated copper particles have an optimal treatment temperature at which the resistivity is minimal. At this temperature, dewetting does not occur and silver necks bridging the copper cores result in high conductivities. The lower cost and low silver content of these particles make them a potential candidate to replace silver particles for the manufacturing of printed electronics.

8 Outlook

I have formulated silver- and copper-based pastes to make printed conductors and demonstrated that high conductivities can be achieved at low treatment temperatures. The particles could be recycled and reused after the lifetime of the prints. In this chapter, I will give an outlook on possible future investigations that can help further improve these materials and make them ready for industrial applications.

In this thesis, I kept the paste formulations simple: metal particles dispersed in ethylene glycol. The purpose of these simple pastes was to assess the effect of particle sintering on the conductivity of printed pastes, without having to consider external effects on conductivity stemming from additives in the pastes. Commercial pastes do contain additives, such as added polymers and additional solvents, to tune the viscosity and optimize the adhesion and mechanical robustness of the final printed structures.

The effect of these additives on the conductivity, sintering mechanism, sintering onset temperatures, and the recycling of particles should be investigated. The comparison between precipitated and atomized particles, as done in Chapter 3, should also be made for these pastes. Another difference that should be taken into consideration is the metal loading of the industrially relevant pastes. The printed simple pastes contain only metal particles after sintering. The industrially relevant printed pastes will have a lower metal content. To minimize the cost and ecological impact, the metal content should be as low as possible, without affecting the conductivity of the prints.

After creating industrially relevant pastes, mechanical testing of printed structures would be required. Pastes could be printed on a variety of flexible substrates and electrically characterized upon bending and stretching. Another important parameter to be addressed is the adhesion to the substrate, which is of great importance in many industrial applications. Such investigations explore their potential use in applications, such as flexible and stretchable conductors or strain sensors.

Another aspect of the printed conductors that would benefit further investigations is the recycling procedure. The procedure presented in this thesis involves the recovery of the powder through the manual removal of the printed structure followed by the breaking of sinter necks through tip-sonication. Industrially relevant prints still contain additives after the sintering procedure, complicating the recycling. An extra separation step needs to be implemented to separate the metal particles from the additives. A more automated recycling route could be investigated where printed pastes can be removed upon applying an external trigger. The work of Kwon *et al.* can be taken as inspiration, where the printed layers were released upon submerging them in hot water [22].

I hope that this thesis, and potential follow-ups, will contribute to more sustainable, and cheaper printed electronics solutions in the future.

BIBLIOGRAPHY

[1] C. Susskind, *My Life With the Printed Circuit*, illus. ed. Bethlehem, PA: Lehigh University Press, 1989, vol. 247, no. 4945, distributor, Associated University Presses, Cranbury, NJ.

[2] A. Sudheshwar, N. Malinverno, R. Hischier, B. Nowack, and C. Som, "The need for design-for-recycling of paper-based printed electronics â€“ a prospective comparison with printed circuit boards," *Resources, Conservation and Recycling*, vol. 189, p. 106757, 2023. [Online]. Available: https://www.sciencedirect.com/science/article/pii/S0921344922005894

[3] M. Naji, I. Deviatkin, V. Leminen, and M. Horttanainen, "Alternative materials for printed circuit board production: An environmental perspective," *Sustainability*, vol. 13, p. 12126, 11 2021.

[4] C. Cano-Raya, Z. Denchev, S. Cruz, and J. Viana, "Chemistry of solid metal-based inks and pastes for printed electronics – a review," *Applied Materials Today*, vol. 15, pp. 416–430, 06 2019.

[5] P. Martins, N. Pereira, A. C. Lima, A. Garcia, C. Mendes-Filipe, R. Policia, V. Correia, and S. Lanceros-Mendez, "Advances in printing and electronics: From engagement to commitment," *Advanced Functional Materials*, vol. 33, no. 16, p. 2213744, 2023. [Online]. Available: https://onlinelibrary.wiley.com/doi/abs/10.1002/adfm.202213744

[6] J. Lemarchand, N. Bridonneau, N. Battaglini, F. Carn, G. Mattana, B. Piro, S. Zrig, and N. Vincent, "Challenges, prospects, and emerging applications of inkjet□printed electronics: A chemist's point of view," *Angewandte Chemie International Edition*, vol. 61, 03 2022.

[7] S. Wünscher, R. Abbel, J. Perelaer, and U. S. Schubert, "Progress of alternative sintering approaches of inkjet-printed metal inks and their application for manufacturing of flexible electronic devices," *J. Mater. Chem. C*, vol. 2, pp. 10 232–10 261, 2014. [Online]. Available: http://dx.doi.org/10.1039/C4TC01820F

[8] L. Mo, Z. Guo, L. Yang, Q. Zhang, Y. Fang, Z. Xin, Z. Chen, K. Hu, L. Han, and L. Li, "Silver nanoparticles based ink with moderate sintering in flexible and printed electronics," *International Journal of Molecular Sciences*, vol. 20, p. 2124, 04 2019.

[9] R. M. German, "Sintering: from empirical observations to scientific principles," in *Sintering: from Empirical Observations to Scientific Principles*, R. M. German, Ed. Boston: Butterworth-Heinemann, 2014. [Online]. Available: https://www.sciencedirect.com/science/article/pii/B9780124016828000094

[10] X. Wang and L. Benabou, "Numerical modeling of low-temperature and low-pressure sintering of silver microparticles based on surface and grain boundary diffusion mechanisms," *Mechanics of Advanced Materials and Structures*, vol. 29, no. 11, pp. 1601–1613, 2022.

[11] H. Zhan, J. Guo, X. Yang, B. Guo, W. Liu, H. Shen, X. Wang, W. Tang, and F. Chen, *Journal of Materials Science: Materials in Electronics*, vol. 30, p. 21343–21354, 2019.

[12] Z. Guo, J. Lang, H. Zhang, C. Yang, S. Lin, and H. Wu, "Facile and scalable synthesis of ag nano□flowers that can be sintered below 120 °c," *Advanced Materials Interfaces*, vol. 9, 08 2022.

[13] Y. Jeyun, Z. Hao, L. Cai-Fu, and S. Katsuaki, *Journal of Materials Science: Materials in Electronics*, vol. 30, p. 18080–18087, 2019.

[14] I. R. P. United Nations Environment Programme, "Environmental risks and challenges of anthropogenic metals flows and cycles," 2013. [Online]. Available: https://wedocs.unep.org/20.500.11822/8451

[15] DuPont, "Molykote® cu-7439 plus paste," https://www.dupont.com/products/molykote-cu-7439-plus-paste-v1.html, accessed: 2024-05-31.

[16] Heraeus, "Thick copper conductor pastes," https://www.heraeus.com/media/media/het/doc_het/products_and_solutions_het_documents/thick_film/Brochure_Heraeus_Thick_Copper_Conductor_Pastes.pdf, accessed: 2024-05-31.

[17] NovaCentrix, "Ci-004 copper nanoparticles," https://www.novacentrix.com/product/ci-004-copper-nanoparticles/, accessed: 2024-05-31.

[18] Dycotec Materials, "Dm-cup-5056 copper paste," https://www.dycotecmaterials.com/product/dm-cup-5056/, accessed: 2024-05-31.

[19] X. Zeng, P. He, M. Hu, W. Zhao, H. Chen, L. Liu, J. Sun, and J. Yang, "Copper inks for printed electronics: a review," *Nanoscale*, vol. 14, pp. 16 003–16 032, 2022. [Online]. Available: http://dx.doi.org/10.1039/D2NR03990G

[20] D. Tomotoshi and H. Kawasaki, "Surface and interface designs in copper-based conductive inks for printed/flexible electronics," *Nanomaterials*, vol. 10, p. 1689, 08 2020.

[21] G. Bidini, F. Fantozzi, P. Bartocci, B. D'Alessandro, M.D'Amico, P. Laranci, E.Scozza, and M.Zagaroli, "Recovery of precious metals from scrap printed circuit boards through pyrolysis," *Journal of Analytical and Applied Pyrolysis*, vol. 111, pp. 140–147, 12 2014.

[22] J. Kwon, C. DelRe, P. Kang, A. Hall, D. Arnold, I. Jayapurna, L. Ma, M. Michalek, R. Ritchie, and T. Xu, "Conductive ink with circular life cycle for printed electronics," *Advanced Materials*, vol. 34, p. 2202177, 07 2022.

[23] C. Xu and N. Willenbacher, "How rheological properties affect fine-line screen printing of pastes: a combined rheological and high-speed video imaging study," *Journal of Coatings Technology and Research*, vol. 15, 08 2018.

[24] K. Q. Yan, S. Tam, K. Fung, and K. Ng, "Product design: Formulation of a screen□printable sintering□type conductive paste," *AIChE Journal*, vol. 66, 06 2020.

[25] A. Ostfeld, I. Deckman, A. Gaikwad, C. Lochner, and A. Arias, "Screen printed passive components for flexible power electronics," *Scientific Reports*, vol. 5, 10 2015.

[26] R. SÃ¸ndergaard, M. HÃ¶sel, D. Angmo, T. T. Larsen-Olsen, and F. C. Krebs, "Roll-to-roll fabrication of polymer solar cells," *Materials Today*, vol. 15, no. 1, pp. 36–49, 2012. [Online]. Available: https://www.sciencedirect.com/science/article/pii/S1369702112700196

[27] A. Kamyshny and S. Magdassi, “Conductive nanomaterials for printed electronics,” *Small*, vol. 10, no. 17, pp. 3515–3535, 2014. [Online]. Available: https://onlinelibrary.wiley.com/doi/abs/10.1002/smll.201303000

[28] R. Rathanasamy, S. Sahoo, J. Lee, A. Das, M. Somasundaram, S. Palaniappan, and S. Sivaraj, “Carbon-based multi-layered films for electronic application: A review,” *Journal of Electronic Materials*, vol. 50, 02 2021.

[29] D. Li, W.-Y. Lai, Y.-Z. Zhang, and W. Huang, “Printable transparent conductive films for flexible electronics,” *Advanced Materials*, vol. 30, no. 10, p. 1704738, 2018. [Online]. Available: https://onlinelibrary.wiley.com/doi/abs/10.1002/adma.201704738

[30] A. Pajor-Świerzy, K. Szczepanowicz, A. Kamyshny, and S. Magdassi, “Metallic core-shell nanoparticles for conductive coatings and printing,” *Advances in Colloid and Interface Science*, vol. 299, p. 102578, 11 2021.

[31] M. Shlomo, G. Michael, and K. Alexander, “Copper nanoparticles for printed electronics: Routes towards achieving oxidation stability,” *Materials*, vol. 3, 09 2010.

[32] L. Zhang, T. Song, L. Shi, N. Wen, Z. Wu, C. Sun, D. Jiang, and Z. Guo, “Recent progress for silver nanowires conducting film for flexible electronics,” *Journal of Nanostructure in Chemistry*, vol. 11, 07 2021.

[33] E. Sancaktar and Y. Wei, “The effect of pressure on the initial establishment of conductive paths in electronically conductive adhesives,” *Journal of Adhesion Science and Technology*, vol. 10, no. 11, pp. 1221–1235, 1996. [Online]. Available: https://doi.org/10.1163/156856196X00201

[34] Y. Mamunya, H. Zois, L. Apekis, and E. Lebedev, “Influence of pressure on the electrical conductivity of metal powders used as fillers in polymer composites,” *Powder Technology*, vol. 140, p. 49â€“55, 02 2004.

[35] S. Shenogin, L. Ferguson, and A. K. Roy, “The effect of contact resistance on electrical conductivity in filled elastomer materials,” *Polymer*, vol. 198, p. 122502, 2020. [Online]. Available: https://www.sciencedirect.com/science/article/pii/S0032386120303347

[36] I. Miccoli, F. Edler, H. PfnÃ¼r, and C. Tegenkamp, “The 100th anniversary of the four-point probe technique: The role of probe geometries in isotropic and anisotropic systems,” *Journal of Physics Condensed Matter*, vol. 27, 05 2015.

[37] H. Topsoe, “Geometric factors in four point resistivity measurement,” *Semiconductor division*, p. 63, 1996.

[38] L. Suk-Joong, 2005.

[39] Z. Xiao, S. Yu, Y. Li, S. Ruan, L. B. Kong, Q. Huang, Z. Huang, K. Zhou, H. Su, Z. Yao, W. Que, Y. Liu, T. Zhang, J. Wang, P. Liu, D. Shen, M. Allix, J. Zhang, and D. Tang, “Materials development and potential applications of transparent ceramics: A review,” *Materials Science and Engineering: R: Reports*, vol. 139, p. 100518, 2020. [Online]. Available: https://www.sciencedirect.com/science/article/pii/S0927796X19301111

[40] W. Han, L. Kong, and M. Xu, “Advances in selective laser sintering of polymers,” *International Journal of Extreme Manufacturing*, vol. 4, no. 4, p. 042002, sep 2022. [Online]. Available: https://dx.doi.org/10.1088/2631-7990/ac9096

[41] X. Kaikai, G. Yadong, and Z. Qiang, “Comparison of traditional processing and additive manufacturing technologies in various performance aspects: a review,” *Archives of Civil and Mechanical Engineering*, vol. 23, 07 2023.

[42] S. Gwynn, “Improved composition of matter called metaline for journal bearings etc.” Patent 101,866, April 12, 1870, u. S. Patent.

[43] Y. Mamunya, H. Zois, L. Apekis, and E. Lebedev, “Influence of pressure on the electrical conductivity of metal powders used as fillers in polymer composites,” *Powder Technology*, vol. 140, p. 49–55, 02 2004.

[44] S. Shenogin, L. Ferguson, and A. K. Roy, “The effect of contact resistance on electrical conductivity in filled elastomer materials,” *Polymer*, vol. 198, p. 122502, 2020. [Online]. Available: https://www.sciencedirect.com/science/article/pii/S0032386120303347

[45] P. Schwed, “Surface diffusion in sintering of spheres on planes,” *The Journal of The Minerals, Metals & Materials Society (TMS)*, vol. 3, pp. 245–246, 1950.

[46] H. Djohari, J. I. MartÃnez-Herrera, and J. J. Derby, “Transport mechanisms and densification during sintering: I. viscous flow versus vacancy diffusion,” *Chemical Engineering Science*, vol. 64, no. 17, pp. 3799–3809, 2009. [Online]. Available: https://www.sciencedirect.com/science/article/pii/S0009250909003418

[47] J. Frenkel, “Viscous flow of crystalline bodies under the action of surface tension,” 1945. [Online]. Available: https://api.semanticscholar.org/CorpusID:222414710

[48] A. R. Boccaccini and R. N. Kramer, “Experimental verification of a stereology-based equation for the shrinkage of glass powder compacts during sintering,” *Glass Technology*, vol. 36, pp. 95–97, 1995. [Online]. Available: https://api.semanticscholar.org/CorpusID:137910476

[49] M. Jr, E. Longo, E. Leite, and R. Aguiar, “In situ observation of glass particle sintering,” *Journal of Chemical Education - J CHEM EDUC*, vol. 83, 03 2006.

[50] F. Thümmler and W. Thomma, “The sintering process,” *Metallurgical Reviews*, vol. 12, no. 1, pp. 69–108, 1967. [Online]. Available: https://doi.org/10.1179/mtlr.1967.12.1.69

[51] Y. Naunheim and C. A. Schuh, “A challenge to the sintering of nanocrystalline metals: Organic burnout and oxide reduction compete with powder consolidation,” *Acta Materialia*, vol. 247, p. 118743, 2023. [Online]. Available: https://www.sciencedirect.com/science/article/pii/S1359645423000757

[52] UT Dots, Inc., “UTDAg Conductive Silver Nanoinks,” https://product.statnano.com/product/9071/utdag-conductive-silver-nanoinks, 2017, accessed: 2024-06-13.

[53] D. M. Ltd., “Dycotec dm-sia-3301 datasheet,” https://www.dycotecmaterials.com/wp-content/uploads/2022/03/Dycotec-DM-SIA-3301-Datasheet.pdf, 2022, accessed: 2024-06-13.

[54] Sigma-Aldrich, “Silver nanoparticles ink for screen printing,” https://www.sigmaaldrich.com/DE/de/product/aldrich/901090, accessed: 2024-06-13.

[55] S. P. Douglas, S. Mrig, and C. E. Knapp, “Mods vs. nps: Vying for the future of printed electronics,” *Chemistry â€“ A European Journal*, vol. 27, no. 31, pp. 8062–8081, 2021. [Online]. Available: https://chemistry-europe.onlinelibrary.wiley.com/doi/abs/10.1002/chem.202004860

[56] J. Ding, J. Liu, Q. Tian, Z. Wu, W. Yao, Z. Dai, L. Liu, and W. Wu, “Preparing of highly conductive patterns on flexible substrates by screen printing of silver nanoparticles with different size distribution,” *Nanoscale Research Letters*, vol. 11, 09 2016.

[57] L. Mo, Z. Guo, Z. Wang, L. Yang, Y. Fang, Z. Xin, X. Li, C. Yinjie, M. Cao, Q. Zhang, and L. Li, “Nano-silver ink of high conductivity and low sintering temperature for paper electronics,” *Nanoscale Research Letters*, vol. 14, p. 197, 06 2019.

[58] S. Magdassi, M. Grouchko, O. Berezin, and A. Kamyshny, “Triggering the sintering of silver nanoparticles at room temperature,” *ACS nano*, vol. 4, pp. 1943–8, 04 2010.

[59] M. Layani, M. Grouchko, S. Shemesh, and S. Magdassi, “Conductive patterns on plastic substrates by sequential inkjet printing of silver nanoparticles and electrolyte sintering solutions,” *J. Mater. Chem.*, vol. 22, pp. 14 349–14 352, 07 2012.

[60] ——, “Conductive patterns on plastic substrates by sequential inkjet printing of silver nanoparticles and electrolyte sintering solutions,” *J. Mater. Chem.*, vol. 22, pp. 14 349–14 352, 07 2012.

[61] N. Ibrahim, J. O. Akindoyo, and M. Mariatti, “Recent development in silver-based ink for flexible electronics,” *Journal of Science: Advanced Materials and Devices*, vol. 7, no. 1, p. 100395, 2022. [Online]. Available: https://www.sciencedirect.com/science/article/pii/S2468217921000770

[62] Y. Jeyun, N. Shijo, C. Chuantong, S. Tohru, Z. Hao, C. Chanyang, L. Cai-Fu, and S. Katsuaki, *Applied physics letters*, vol. 114, 2019.

[63] N. Matsuhisa, D. Inoue, P. Zalar, H. Jin, Y. Matsuba, A. Itoh, T. Yokota, D. Hashizume, and T. Someya, “Printable elastic conductors by in situ formation of silver nanoparticles from silver flakes,” *Nature materials*, vol. 16, 05 2017.

[64] W. Li, X. Xu, W. Li, Y. Zhao, and M. Chen, “Green synthesis of micron-sized silver flakes and their application in conductive ink,” *Journal of Materials Science*, vol. 53, 05 2018.

[65] W. M. Haynes, *CRC Handbook of Chemistry and Physics*, 2016, no. 97.

[66] Daily Metal Price, “Daily metal price,” 2022. [Online]. Available: https://www.dailymetalprice.com/metalprices.php?c=cu&u=oz&d=10

[67] USGS (United States Geological Survey), “Silver in june 2021,” 2022. [Online]. Available: https://www.usgs.gov/centers/nmic/minerals-information-silver

[68] International Copper Study Group (ICSG), “Long Term Availability of Copper,” 2022. [Online]. Available: https://icsg.org/long-term-availability-of-copper/

[69] Silver Institute, “Silver Market Interim Report 2023,” 2023. [Online]. Available: https://www.silverinstitute.org/wp-content/uploads/2023/11/SilverMarket2023_interim-report.pdf

[70] D. Tomotoshi and H. Kawasaki, “Surface and interface designs in copper-based conductive inks for printed/flexible electronics,” *Nanomaterials*, vol. 10, no. 9, 2020. [Online]. Available: https://www.mdpi.com/2079-4991/10/9/1689

[71] M. Nishimoto, R. Tokura, M. T. Nguyen, and T. Yonezawa, “Copper materials for low temperature sintering,” *MATERIALS TRANSACTIONS*, vol. 63, no. 5, pp. 663–675, 2022.

[72] C. Gattinoni and A. Michaelides, “Atomistic details of oxide surfaces and surface oxidation: the example of copper and its oxides,” *Surface Science Reports*, vol. 70, no. 3, pp. 424–447, 2015. [Online]. Available: https://www.sciencedirect.com/science/article/pii/S0167572915000217

[73] P. Keil, D. Luetzenkirchen-Hecht, and R. Frahm, “Investigation of room temperature oxidation of cu in air by yoneda-xafs,” *AIP Conference Proceedings*, vol. 882, pp. 490 – 492, 02 2007.

[74] J. J. D. León, D. M. Fryauf, R. D. Cormia, and N. P. Kobayashi, “Study of the formation of native oxide on copper at room temperature,” in *Low-Dimensional Materials and Devices 2016*, N. P. Kobayashi, A. A. Talin, M. S. Islam, and A. V. Davydov, Eds., vol. 9924, International Society for Optics and Photonics. SPIE, 2016, p. 99240O. [Online]. Available: https://doi.org/10.1117/12.2238745

[75] S. Choudhary, J. V. N. Sarma, S. Pande, S. Ababou-Girard, P. Turban, B. Lepine, and S. Gangopadhyay, “Oxidation mechanism of thin Cu films: A gateway towards the formation of single oxide phase,” *AIP Advances*, vol. 8, no. 5, p. 055114, 05 2018. [Online]. Available: https://doi.org/10.1063/1.5028407

[76] H. Wieder and A. W. Czanderna, “The oxidation of copper films to cuo0.67,” *The Journal of Physical Chemistry*, vol. 66, no. 5, pp. 816–821, 1962. [Online]. Available: https://doi.org/10.1021/j100811a010

[77] J. Aromaa, M. Kekkonen, M. Mousapour, A. Jokilaakso, and M. Lundström, “The oxidation of copper in air at temperatures up to 100 °c,” *Corrosion and Materials Degradation*, vol. 2, no. 4, pp. 625–640, 2021. [Online]. Available: https://www.mdpi.com/2624-5558/2/4/33

[78] N. Eisenreich, O. Schulz, A. Koleczko, and S. Knapp, “Comparison of kinetics, oxide crystal growth and diffusivities of nano- and micrometer-sized copper particles on oxidation in air,” *Thermochimica Acta*, vol. 654, pp. 93–100, 2017. [Online]. Available: https://www.sciencedirect.com/science/article/pii/S0040603117301272

[79] Y. Zhang, P. Zhu, G. Li, T. Zhao, X. Fu, R. Sun, F. Zhou, and C.-p. Wong, “Facile preparation of monodisperse, impurity-free, and antioxidation copper nanoparticles on a large scale for application in conductive ink,” *ACS Applied Materials & Interfaces*, vol. 6, no. 1, pp. 560–567, 2014. [Online]. Available: https://doi.org/10.1021/am404620y

[80] M. Shlomo, G. Michael, and K. Alexander, “Copper nanoparticles for printed electronics: Routes towards achieving oxidation stability,” *Materials*, vol. 3, 09 2010.

[81] Y. Gao, W. Li, C. Chen, H. Zhang, J. Jiu, C.-F. Li, S. Nagao, and K. Suganuma, “Novel copper particle paste with self-reduction and self-protection characteristics for die attachment of power semiconductor under a nitrogen atmosphere,” *Materials Design*, vol. 160, pp. 1265–1272, 2018. [Online]. Available: https://www.sciencedirect.com/science/article/pii/S0264127518308098

[82] N. L. Pacioni, V. Filippenko, N. Presseau, and J. C. Scaiano, “Oxidation of copper nanoparticles in water: mechanistic insights revealed by oxygen uptake and spectroscopic methods,” *Dalton Trans.*, vol. 42, pp. 5832–5838, 2013. [Online]. Available: http://dx.doi.org/10.1039/C3DT32836H

[83] P. Cavaliere, B. Sadeghi, and A. Shabani, *Spark Plasma Sintering: Process Fundamentals*. Cham: Springer International Publishing, 2019, pp. 3–20. [Online]. Available: https://doi.org/10.1007/978-3-030-05327-7_1

[84] C. Cheng, J. Li, T. Shi, X. Yu, J. Fan, G. Liao, X. Li, S. Cheng, Y. Zhong, and Z. Tang, “A novel method of synthesizing antioxidative copper nanoparticles for high performance conductive ink,” *Journal of Materials Science: Materials in Electronics*, vol. 28, pp. 1–9, 09 2017.

[85] J. Liu, H. Chen, H. Ji, and M. Li, “Highly conductive cu-cu joint formation by low-temperature sintering of formic acid-treated cu nanoparticles,” *ACS Applied Materials Interfaces*, vol. 8, 11 2016.

[86] S. Yokoyama, J. Nozaki, K. Motomiya, N. Tsukahara, and H. Takahashi, “Strong adhesion of polyvinylpyrrolidone-coated copper nanoparticles on various substrates fabricated from well-dispersed copper nanoparticle inks,” *Colloids and Surfaces A: Physicochemical and Engineering Aspects*, vol. 591, p. 124567, 02 2020.

[87] N. Sarwar, “Synthesis of citrate-capped copper nanoparticles: A low temperature sintering approach for the fabrication of oxidation stable flexible conductive film,” *Applied Surface Science*, vol. 542, 11 2020.

[88] S. Hong, C. Liu, S. Hao, W. Fu, J. Peng, B. Wu, and N. Zheng, “Antioxidant high-conductivity copper paste for low-cost flexible printed electronics,” *npj Flexible Electronics*, vol. 6, p. 17, 03 2022.

[89] H. T. Hai, H. Takamura, and J. Koike, “Oxidation behavior of cu–ag core–shell particles for solar cell applications,” *Journal of Alloys and Compounds*, vol. 564, pp. 71–77, 2013. [Online]. Available: https://www.sciencedirect.com/science/article/pii/S0925838813003472

[90] X. Yu, J. Li, T. Shi, C. Cheng, G. Liao, J. Fan, T. Li, and Z. Tang, “A green approach of synthesizing of cu-ag core-shell nanoparticles and their sintering behavior for printed electronics,” *Journal of Alloys and Compounds*, vol. 724, pp. 365–372, 2017. [Online]. Available: https://www.sciencedirect.com/science/article/pii/S092583881732409X

[91] M. Grouchko, A. Kamyshny, and S. Magdassi, “Formation of air-stable copper-silver core-shell nanoparticles for inkjet printing,” *Journal of Materials Chemistry - J MATER CHEM*, vol. 19, 01 2009.

[92] S. Kim, M. Kim, and J.-H. Lee, “Sinter bonding and formation of a near-full-density bondline at 250 Â°c via addition of submicrometer cu particles to micrometer ag-coated cu particles,” *Journal of Materials Science: Materials in Electronics*, vol. 27, 10 2020.

[93] G. Yang, P. Wang, Y. Liu, S. Lu, B. Luo, T. Lai, S. Ta, T. Lin, J. Luo, Y. Zhang, and C. Cui, “Effect of ag coating on the oxidation resistance, sintering properties, and migration resistance of cu particles,” *Journal of Alloys and Compounds*, vol. 923, p. 166271, 2022. [Online]. Available: https://www.sciencedirect.com/science/article/pii/S0925838822026627

[94] W. Yang, W. Zhu, X. Wang, S. Hu, P. Cui, Y. Fang, Z. Li, F. Qi, H. Cao, H. Xu, and M. Li, “Low-temperature packaging through ag-cu supersaturated solid solution nanoparticle paste for high-temperature power electronics,” *Materials Letters*, vol. 357, p. 135675, 12 2023.

[95] M. Won, D. Kim, H. Yang, and C. Oh, “Low-temperature sinterable cu@ag paste with superior strength driven by pre-heating process,” *Energies*, vol. 16, p. 5419, 07 2023.

[96] Y. Tian, Z. Jiang, C. Wang, s. ding, J. Wen, Z.-Q. Liu, and C. Wang, “Sintering mechanism of the cu-ag core-shell nanoparticle paste at low temperature in ambient air,” *RSC Adv.*, vol. 6, 01 2016.

[97] A. P. Swierzy, Y. Farraj, A. Kamyshny, and S. Magdassi, “Air stable copper-silver core-shell submicron particles: Synthesis and conductive ink formulation,” *Colloids and Surfaces A: Physicochemical and Engineering Aspects*, vol. 521, pp. 272–280, 2017, dynamics of wetting by surfactant solutions. [Online]. Available: https://www.sciencedirect.com/science/article/pii/S0927775716306641

[98] A. Pajor-Świerzy, Y. Farraj, A. Kamyshny, and S. Magdassi, “Effect of carboxylic acids on conductivity of metallic films formed by inks based on copper@silver core-shell particles,” *Colloids and Surfaces A: Physicochemical and Engineering Aspects*, vol. 522, pp. 320–327, 2017. [Online]. Available: https://www.sciencedirect.com/science/article/pii/S0927775717302558

[99] A. Pajor-Świerzy, K. Szczepanowicz, A. Kamyshny, and S. Magdassi, “Metallic core-shell nanoparticles for conductive coatings and printing,” *Advances in Colloid and Interface Science*, vol. 299, p. 102578, 2022. [Online]. Available: https://www.sciencedirect.com/science/article/pii/S0001868621002190

[100] C.-K. Kim, G.-J. Lee, L. Min Gu, and C. K. Rhee, “A novel method to prepare cu@ag coreâ€“shell nanoparticles for printed flexible electronics,” *Powder Technology*, vol. 263, pp. 1–6, 09 2014.

[101] N. R. Kim, Y. Lee, C. Lee, J. Koo, and H. Lee, “Surface modification of oleylamine-capped agâ€“cu nanoparticles to fabricate low-temperature-sinterable agâ€“cu nanoink,” *Nanotechnology*, vol. 27, p. 345706, 07 2016.

[102] C. Lee, N. R. Kim, J. Koo, Y. Lee, and H. Lee, “Cu-ag coreâ€“shell nanoparticles with enhanced oxidation stability for printed electronics,” *Nanotechnology*, vol. 26, p. 455601, 10 2015.

[103] A. Titkov, O. Logutenko, A. Vorobyov, E. Gerasimov, I. Shundrina, N. Bulina, and N. Lyakhov, "Synthesis of Ëœ10 nm size cu/ag core-shell nanoparticles stabilized by an ethoxylated carboxylic acid for conductive ink," *Colloids and Surfaces A: Physicochemical and Engineering Aspects*, vol. 577, 06 2019.

[104] Y. Zhang, P. Zhu, G. li, Z. Cui, C. Cui, K. Zhang, J. Gao, X. Chen, G. Zhang, R. Sun, and C. Wong, "Pvp-mediated galvanic replacement synthesis of smart elliptic cu-ag nanoflakes for electrically conductive pastes," *ACS Applied Materials Interfaces*, vol. 11, 02 2019.

[105] L. Xie, M. Mäntysalo, A. Cabezas, Y. Feng, and F. Jonsson, "Electrical performance and reliability evaluation of inkjet-printed ag interconnections on paper substrates," *Materials Letters*, vol. 88, 12 2012.

[106] D. J. Kang, Y. Jüttke, L. González-García, A. Escudero, M. Haft, and T. Kraus, "Reversible conductive inkjet printing of healable and recyclable electrodes on cardboard and paper," *Small*, vol. 16, no. 25, p. 2000928, 2020. [Online]. Available: https://onlinelibrary.wiley.com/doi/abs/10.1002/smll.202000928

[107] U. Kavcic, I. Karlovits, and J. Zule, "Deinking of screen-printed electrodes printed on invasive plant-based paper," *Sustainability*, vol. 12, 02 2020.

[108] J. Lv, G. Thangavel, Y. Xin, D. Gao, W. C. Poh, S. Chen, and P. S. Lee, "Printed sustainable elastomeric conductor for soft electronics," *Nature Communications*, vol. 14, 11 2023.

[109] A. Sudheshwar, N. Malinverno, R. Hischier, B. Nowack, and C. Som, "The need for design-for-recycling of paper-based printed electronics â€“ a prospective comparison with printed circuit boards," *Resources, Conservation and Recycling*, vol. 189, p. 106757, 2023. [Online]. Available: https://www.sciencedirect.com/science/article/pii/S0921344922005894

[110] M. Naji, M. Valimaki, L. Hakola, K. Eiroma, K. Immonen, M. Abdulkareem, and M. Horttanainen, "The effect of conductive ink alternation on the sustainability and functioning of printed electronics," *Flexible and Printed Electronics*, vol. 8, 05 2023.

[111] C. Blais, A. Dinh, □. Loranger, and G. Abdulnour, "Precious metals recovery process from electronic boards: Case study of a non-profit organization (qc, canada)," *Sustainability*, vol. 16, p. 2509, 03 2024.

[112] G. Bidini, F. Fantozzi, P. Bartocci, B. Dâ€˜Alessandro, M. Dâ€˜Amico, P. Laranci, E. Scozza, and M. Zagaroli, "Recovery of precious metals from scrap printed circuit boards through pyrolysis," *Journal of Analytical and Applied Pyrolysis*, vol. 111, pp. 140–147, 2015. [Online]. Available: https://www.sciencedirect.com/science/article/pii/S0165237014003465

[113] J. Fazari, M. Hossain, and P. Charpentier, "A review on metal extraction from waste printed circuit boards (wpcbs)," *Journal of Materials Science*, vol. 59, pp. 1–28, 07 2024.

[114] S. Bi, B. Gao, X. Han, Z. He, J. Metts, C. Jiang, and K. Asare-Yeboah, "Recent progress in printing flexible electronics: A review," 06 2024.

[115] D. Li, W.-Y. Lai, F. Feng, and W. Huang, "Post-treatment of screen-printed silver nanowire networks for highly conductive flexible transparent films," *Advanced Materials Interfaces*, vol. 8, no. 13, p. 2100548, 2021. [Online]. Available: https://onlinelibrary.wiley.com/doi/abs/10.1002/admi.202100548

[116] D. Lide, *CRC Handbook of chemistry and physics*, 01 2007.

[117] M. Talukdar and E. Baker, "Conductivity studies on silver oxide," *Solid State Communications*, vol. 7, no. 2, pp. 309–310, 1969. [Online]. Available: https://www.sciencedirect.com/science/article/pii/0038109869904074

[118] K. Rajan, I. Roppolo, A. Chiappone, S. Bocchini, D. Perrone, and C. A., "Silver nanoparticle ink technology: state of the art," *Nanotechnol Sci Appl.*, vol. 9, pp. 1–13, 2016.

[119] S. A. Paknejad and S. H. Mannan, "Review of silver nanoparticle based die attach materials for high power/temperature applications," *Microelectronics Reliability*, vol. 70, pp. 1–11, 2017. [Online]. Available: https://www.sciencedirect.com/science/article/pii/S0026271417300161

[120] W. Coblenz, J. Dynys, R. Cannon, and R. Coble, "Initial stage solid state sintering models. a critical analysis and assessment." *Materials Science Research*, vol. 13, pp. 141–157, 01 1980.

[121] P. M. Derlet, *Sintering theory*, 2017.

[122] S. P. Douglas, S. Mrig, and C. E. Knapp, "Mods vs. nps: Vying for the future of printed electronics," *Chemistry â€“ A European Journal*, vol. 27, no. 31, pp. 8062–8081, 2021. [Online]. Available: https://chemistry-europe.onlinelibrary.wiley.com/doi/abs/10.1002/chem.202004860

[123] J. Krishna, A. S. Perumal, I. Khan, R. Chelliah, S. Wei, C. M. A. Swamidoss, D.-H. Oh, and B. Bharathiraja, "Chapter 6 - synthesis of nanomaterials for biofuel and bioenergy applications," in *Nanomaterials*, R. P. Kumar and B. Bharathiraja, Eds. Academic Press, 2021, pp. 97–165. [Online]. Available: https://www.sciencedirect.com/science/article/pii/B9780128224014000313

[124] P. G. Jamkhande, N. W. Ghule, A. H. Bamer, and M. G. Kalaskar, "Metal nanoparticles synthesis: An overview on methods of preparation, advantages and disadvantages, and applications," *Journal of Drug Delivery Science and Technology*, vol. 53, p. 101174, 2019. [Online]. Available: https://www.sciencedirect.com/science/article/pii/S1773224718308189

[125] I. Kanelidis and T. Kraus, "The role of ligands in coinage-metal nanoparticles for electronics," *Beilstein Journal of Nanotechnology*, vol. 8, pp. 2625–2639, 12 2017.

[126] P. Liu and G. Chen, "Chapter two - making porous metals," in *Porous Materials*, P. Liu and G. Chen, Eds. Boston: Butterworth-Heinemann, 2014, pp. 21–112. [Online]. Available: https://www.sciencedirect.com/science/article/pii/B9780124077881000022

[127] Y. Chen and C. A. Schuh, "Contribution of triple junctions to the diffusion anomaly in nanocrystalline materials," *Scripta Materialia*, vol. 57, no. 3, pp. 253–256, 2007. [Online]. Available: https://www.sciencedirect.com/science/article/pii/S1359646207002618

[128] G. Palumbo, S. J. Thorpe, and K. T. Aust, "On the contribution of triple junctions to the structure and properties of nanocrystalline materials," *Scripta Metallurgica Et Materialia*, vol. 24, pp. 1347–1350, 1990. [Online]. Available: https://api.semanticscholar.org/CorpusID:136981512

[129] M. Lazar, *Let's Review: Physics, the Physical Setting*. Barron's Educational Series; Fifth edition, 2007.

[130] W. M. Haynes, *CRC Handbook of Chemistry and Physics*, 2016, no. 97.

[131] M. Menzinger and R. Wolfgang, "The meaning and use of the arrhenius activation energy," *Angewandte Chemie International Edition in English*, vol. 8, no. 6, pp. 438–444, 1969. [Online]. Available: https://onlinelibrary.wiley.com/doi/abs/10.1002/anie.196904381

[132] N. Q. Lam, S. J. Rothman, H. Mehrer, and L. J. Nowicki, "Self-diffusion in silver at low temperatures," *physica status solidi (b)*, vol. 57, no. 1, pp. 225–236, 1973. [Online]. Available: https://onlinelibrary.wiley.com/doi/abs/10.1002/pssb.2220570122

[133] B. Molleman and T. Hiemstra, "Surface structure of silver nanoparticles as model for understanding oxidative dissolution of silver ions," *Langmuir*, vol. 31, 11 2015.

[134] R. Glover, J. Miller, and J. Hutchison, "Generation of metal nanoparticles from silver and copper objects: Nanoparticle dynamics on surfaces and potential sources of nanoparticles in the environment," *ACS nano*, vol. 5, pp. 8950–7, 11 2011.

[135] N. T. K. Thanh, N. Maclean, and S. Mahiddine, "Mechanisms of nucleation and growth of nanoparticles in solution," *Chemical Reviews*, vol. 114, no. 15, pp. 7610–7630, 2014, pMID: 25003956. [Online]. Available: https://doi.org/10.1021/cr400544

[136] V. K. LaMer and R. H. Dinegar, "Theory, production and mechanism of formation of monodispersed hydrosols," *Journal of the American Chemical Society*, vol. 72, no. 11, pp. 4847–4854, 1950. [Online]. Available: https://doi.org/10.1021/ja01167a001

[137] J. Liu and R. Hurt, "Ion release kinetics and particle persistence in aqueous nano-silver colloids," *Environmental science technology*, vol. 44, pp. 2169–75, 02 2010.

[138] "Loctite eci 1010 ec," https://www.henkel-adhesives.com, 2023, screen printable highly conductive silver ink, Sheet Resistance: 0.007 Ω/□/25µm, Operating Temperature: Max 100ºC.

[139] "Silver conductive paste," https://www.sigmaaldrich.com, 2023, product Number: 901769, Sun Chemical, Appearance: Silver Paste, Electrical Resistance: ≤0.10 Ω/sq at 25 microns.

[140] "Dm-sip-3028as silver paste," https://www.dycotecmaterials.com, 2022, screen printable silver paste for SPD and PDLC Smart Glass applications, Volume Resistivity: <28 µΩ·cm, Sheet Resistance: <10 mΩ/□/25µm.

[141] S. Wünscher, R. Abbel, J. Perelaer, and U. S. Schubert, "Progress of alternative sintering approaches of inkjet-printed metal inks and their application for manufacturing of flexible electronic devices," *J. Mater. Chem. C*, vol. 2, pp. 10 232–10 261, 2014. [Online]. Available: http://dx.doi.org/10.1039/C4TC01820F

[142] C. Cano-Raya, Z. Z. Denchev, S. F. Cruz, and J. C. Viana, "Chemistry of solid metal-based inks and pastes for printed electronics â€“ a review," *Applied Materials Today*, vol. 15, pp. 416–430, 2019. [Online]. Available: https://www.sciencedirect.com/science/article/pii/S2352940718306802

[143] B. Nguyen and H. Nguyen Van, "Promising applications of graphene and graphene-based nanostructures," *Advances in Natural Sciences: Nanoscience and Nanotechnology*, vol. 7, p. 023002, 04 2016.

[144] Q. Huang and Y. Zhu, "Printing conductive nanomaterials for flexible and stretchable electronics: A review of materials, processes, and applications," *Advanced Materials Technologies*, vol. 4, no. 5, p. 1800546, 2019. [Online]. Available: https://onlinelibrary.wiley.com/doi/abs/10.1002/admt.201800546

[145] W. Lövenich, "Pedot-properties and applications," *Polymer Science Series C*, vol. 56, 09 2014.

[146] S. Paknejad, G. Dumas, G. West, G. Lewis, and S. Mannan, "Microstructure evolution during 300Â°c storage of sintered ag nanoparticles on ag and au substrates," *Journal of Alloys and Compounds*, vol. 617, pp. 994–1001, 2014. [Online]. Available: https://www.sciencedirect.com/science/article/pii/S0925838814019173

[147] K. Rajan, I. Roppolo, A. Chiappone, S. Bocchini, D. Perrone, and C. A., "Silver nanoparticle ink technology: state of the art," *Nanotechnol Sci Appl.*, vol. 9, pp. 1–13, 2016.

[148] L. Mo, Z. Guo, L. Yang, Q. Zhang, Y. Fang, Z. Xin, Z. Chen, K. Hu, L. Han, and L. Li, "Silver nanoparticles based ink with moderate sintering in flexible and printed electronics," *International Journal of Molecular Sciences*, vol. 20, p. 2124, 04 2019.

[149] D. Impelen, L. González-García, and T. Kraus, "Recyclability-by-design of printed electronics by low-temperature sintering of silver microparticles," *Advanced Electronic Materials*, 11 2024.

[150] C. Chen and K. Suganuma, "Microstructure and mechanical properties of sintered ag particles with flake and spherical shape from nano to micro size," *Materials and Design*, 12 2018.

[151] C. Chen, J. Yeom, C. Choe, G. Liu, Y. Gao, Z. Zhang, B. Zhang, D. Kim, and K. Suganuma, "Necking growth and mechanical properties of sintered ag particles with different shapes under air and n2 atmosphere," *Journal of Materials Science*, vol. 54, 10 2019.

[152] C. Chen, Z. Zhang, B. Zhang, and K. Suganuma, "Micron-sized ag flake particles direct die bonding on electro-less ni-p finished dbc substrate: low-temperature pressure-free sintering, bonding mechanism and high temperature aging reliability," *Journal of Materials Science Materials in Electronics*, vol. 31, 01 2020.

[153] W. Li, Y. Li, Y. Wang, Y. Liu, C. Chen, J. Zhang, and H. Yan, "Pressureless sinter-joining of micron-ag flake pastes at 160 °c enabled by solvent and interface engineering," *Journal of Materials Processing Technology*, vol. 322, p. 118207, 10 2023.

[154] S.-C. Fu, M. Zhao, H. Shan, and Y. Li, "Fabrication of large-area interconnects by sintering of micron ag paste," *Materials Letters*, vol. 226, 05 2018.

[155] H. Zhang, C. Chen, J. Jiu, and K. Suganuma, "Solvent effect on pressureless and low-temperature sintering of ag paste for die-attachment in high-power devices," 08 2017, pp. 624–627.

[156] T. Nakanishi, K. Yamagishi, E. Iwase, H. Iwata, S. Takeoka, and T. Fujie, "Sinter-free stretchable conductive inks composed of polystyrene-block-polybutadiene-block-polystyrene and silver flakes in tetrahydrofuran," *Applied Physics Express*, vol. 12, 06 2019.

[157] D. Kang, Y. Jüttke, L. Gonzalez-Garcia, A. Escudero, M. Haft, and T. Kraus, "Reversible conductive inkjet printing of healable and recyclable electrodes on cardboard and paper," *Small*, vol. 16, 05 2020.

[158] L. Holzer and M. Cantoni, "Review of fib-tomography," *Nanofabrication using focused ion and electron beams: Principles and applications*, vol. 559201222, pp. 410–435, 2012.

[159] S. Cooper, A. Bertei, P. Shearing, J. Kilner, and N. Brandon, "Taufactor: An open-source application for calculating tortuosity factors from tomographic data," *SoftwareX*, vol. 5, pp. 203–210, 2016. [Online]. Available: https://www.sciencedirect.com/science/article/pii/S2352711016300280

[160] J. Fu, H. R. Thomas, and C. Li, "Tortuosity of porous media: Image analysis and physical simulation," *Earth-Science Reviews*, vol. 212, p. 103439, 2021.

[161] A. Cecen, E. Wargo, A. Hanna, D. Turner, S. Kalidindi, and E. Kumbur, "3-d microstructure analysis of fuel cell materials: spatial distributions of tortuosity, void size and diffusivity," *Journal of The Electrochemical Society*, vol. 159, no. 3, p. B299, 2012.

[162] X. Y. Qin, W. Zhang, L. D. Zhang, L. D. Jiang, X. J. Liu, and D. Jin, "Low-temperature resistance and its temperature dependence in nanostructured silver," *Phys. Rev. B*, vol. 56, pp. 10 596–10 604, Oct 1997. [Online]. Available: https://link.aps.org/doi/10.1103/PhysRevB.56.10596

[163] I. Bakonyi, "Accounting for the resistivity contribution of grain boundaries in metals: critical analysis of reported experimental and theoretical data for ni and cu," *Eur. Phys. J. Plus*, vol. 136, no. 4, p. "410", 2021. [Online]. Available: "https://doi.org/10.1140/epjp/s13360-021-01303-4"

[164] C. Su and X. Su, "Impact of grain size and grain size distribution on the resistivity of metal nanocrystalline systems," *Computational Materials Science*, vol. 108, pp. 62–65, 2015. [Online]. Available: https://www.sciencedirect.com/science/article/pii/S0927025615003699

[165] H. Yoshinaga, Y. Arami, O. Kajita, and T. Sakai, "Highly densed-mh electrode using flaky nickel powder and gas-atomized hydrogen storage alloy powder," *Journal of Alloys and Compounds - J ALLOYS COMPOUNDS*, vol. 330, pp. 846–850, 01 2002.

[166] P. Adler, C. Jacquin, and J. Quiblier, "Flow in simulated porous media," *International Journal of Multiphase Flow*, vol. 16, no. 4, pp. 691–712, 1990. [Online]. Available: https://www.sciencedirect.com/science/article/pii/030193229090025E

[167] T.-T. Nguyen, A. Demortière, B. Fleutot, B. Delobel, C. Delacourt, and S. J. Cooper, "The electrode tortuosity factor: why the conventional tortuosity factor is not well suited for quantifying transport

in porous li-ion battery electrodes and what to use instead," *npj Computational Materials*, vol. 6, no. 1, p. 123, 2020.

[168] K. Wakamoto, Y. Mochizuki, T. Otsuka, K. Nakahara, and T. Namazu, "Tensile mechanical properties of sintered porous silver films and their dependence on porosity," *Japanese Journal of Applied Physics*, vol. 58, p. SDDL08, 06 2019.

[169] F. Bensebaa, "Chapter 2 - wet production methods," in *Nanoparticle Technologies*, ser. Interface Science and Technology, F. Bensebaa, Ed. Elsevier, 2013, vol. 19, pp. 85–146. [Online]. Available: https://www.sciencedirect.com/science/article/pii/B9780123695505000021

[170] P. Chattopadhyay, T. Gemming, A. EychmÃ¼ller, and J. Simmchen, "Polyol-assisted synthesis of copper particles," *The Journal of Physical Chemistry C*, vol. 125, no. 45, pp. 24 887–24 893, 2021. [Online]. Available: https://doi.org/10.1021/acs.jpcc.1c06591

[171] E. B. Choi and J.-H. Lee, "Dewetting behavior of ag in ag-coated cu particle with thick ag shell," *Applied Surface Science*, vol. 480, pp. 839–845, 2019. [Online]. Available: https://www.sciencedirect.com/science/article/pii/S0169433219305720

[172] J. H. Kim and J.-H. Lee, "Microstructural investigation of the oxidation behavior of cu in ag-coated cu films using a focused ion beam transmission electron microscopy technique," *Japanese Journal of Applied Physics*, vol. 55, no. 6S3, p. 06JG01, may 2016. [Online]. Available: https://dx.doi.org/10.7567/JJAP.55.06JG01

[173] M. I. Kim and J.-H. Lee, "Die sinter bonding in air using cu@ag particulate preform and rapid formation of near-full density bondline," *Journal of Materials Research and Technology*, vol. 14, pp. 1724–1738, 2021. [Online]. Available: https://www.sciencedirect.com/science/article/pii/S2238785421007225

[174] Y. Kim, E. B. Choi, and J.-H. Lee, "Surface modification of ag-coated cu particles using dicarboxylic acids to enhance the electrical conductivity of sintered films by suppressing dewetting in ag shells," *Applied Surface Science*, vol. 640, p. 158326, 2023. [Online]. Available: https://www.sciencedirect.com/science/article/pii/S0169433223020068

[175] A. Zhakypov, R. Nemkayeva, Y. Yerlanuly, M. Tulegenova, B. Kurbanov, M. Aitzhanov, A. Markhabayeva, and M. Gabdullin, "Synthesis and in situ oxidation of copper micro- and nanoparticles by arc discharge plasma in liquid," *Scientific Reports*, vol. 13, 09 2023.

[176] S. Choudhary, J. V. N. Sarma, S. Pande, S. Ababou-Girard, P. Turban, B. Lepine, and S. Gangopadhyay, "Oxidation mechanism of thin Cu films: A gateway towards the formation of single oxide phase," *AIP Advances*, vol. 8, no. 5, p. 055114, 05 2018. [Online]. Available: https://doi.org/10.1063/1.5028407

9 Supporting Information

9.1 Chapter 2: State of the art and theory

2-point *in-situ* setup ($\frac{m\Omega}{sq}$)	**4-point setup ($\frac{m\Omega}{sq}$)**
8.07	9.25
2.27	3.05
1110.63	974.16
33.23	39.85
1.60	5.03
11.20	15.21

Table 9.1: Comparison between 2-point probe and 4-point probe measurements

9.2 Chapter 3: Recyclability-by-design of Printed Electronics by Low-Temperature Sintering of Silver Microparticles

9.2.1 SEM images of the precipitated and atomized particles

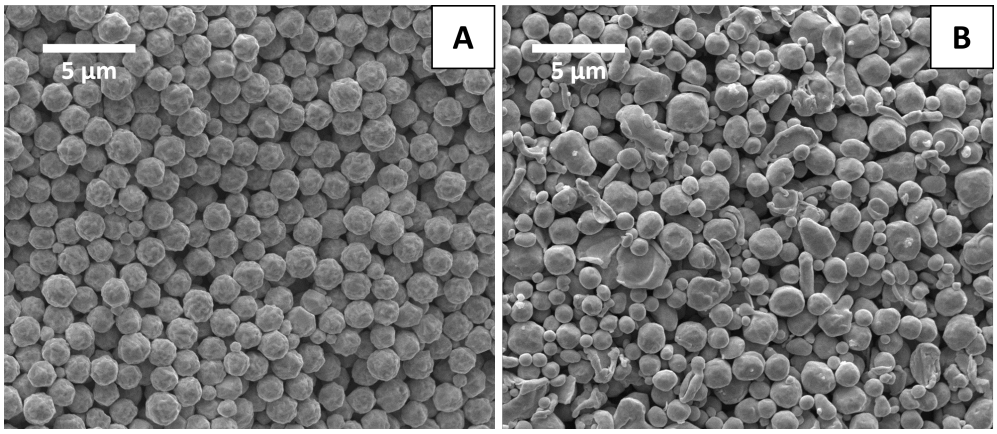

Figure S1: (A) Top view SEM images of 1.5 µm precipitated silver particles and (B) 1.7 µm atomized particles.

9.2.2 Surfactants on the surface of precipitated particles

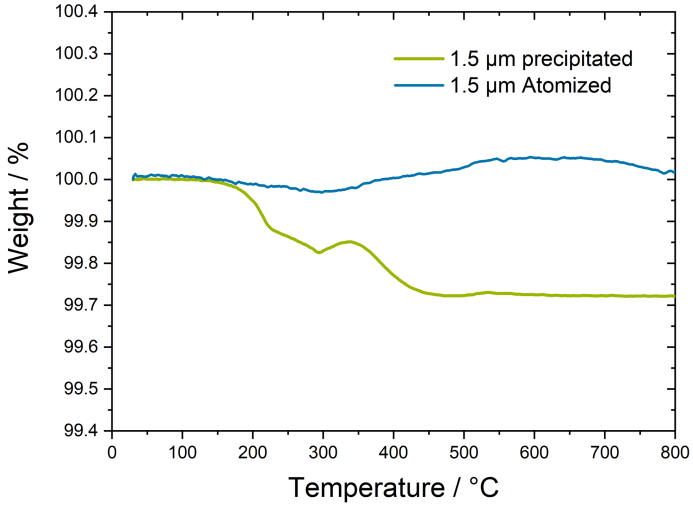

Figure S2: Thermogravimetric analysis (TGA) graphs of 1.5 µm precipitated (blue line) and 1.7 µm atomized silver particles (green line). It can be observed that precipitated particles show a weight loss due to surfactant decomposition between 200 and 400 °C. The atomized particles don't show a weight loss over the entire temperature range due to the absence of organic surfactants.

9.2.3 Porosity of the particles

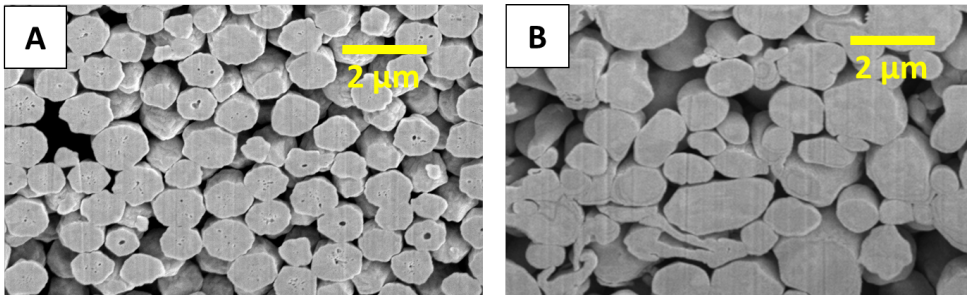

Figure S3: (A) Cross-sectional SEM images of prints containing 1 µm precipitated and (B) 1.7 µm atomized silver particles. Pores can be observed in the particle cross-sections for precipitated particles (A), compared to dense particle cross-sections for atomized particles (B).

9.2.4 Determination of the grain size

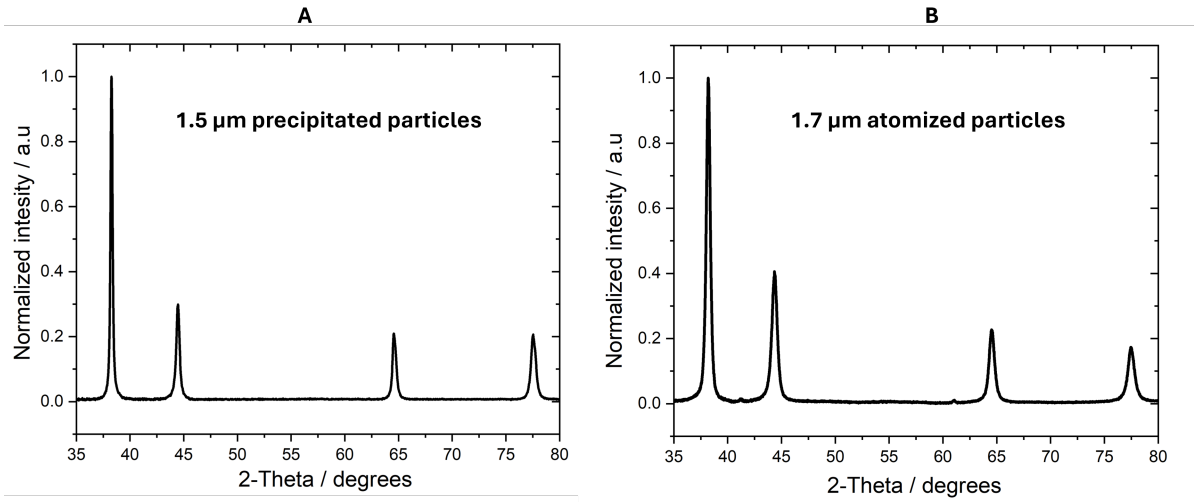

Figure S4: (A) X-ray diffraction (XRD) graphs of 1.5 µm precipitated and (B) 1.7 µm atomized particles.

To determine the crystallite size of both precipitated and atomized particles Scherrer‘s formula was used:

$$D_p = \frac{K \cdot \lambda}{B \cdot \cos(\theta)} \tag{9.1}$$

D_p is the crystallite diameter in nm, K is Scherrer's constant ($K = 0.94$ is used, the value for spherical grains with cubic symmetry), λ is the x-ray wavelength in nm, B is full width at half maximum of the observed peak, and θ is the XRD peak position. D_p was determined for the (111) peak at $\theta = 38.19°$ in Figure S4 A and B.

9.2.5 Growth of the grain size during sintering

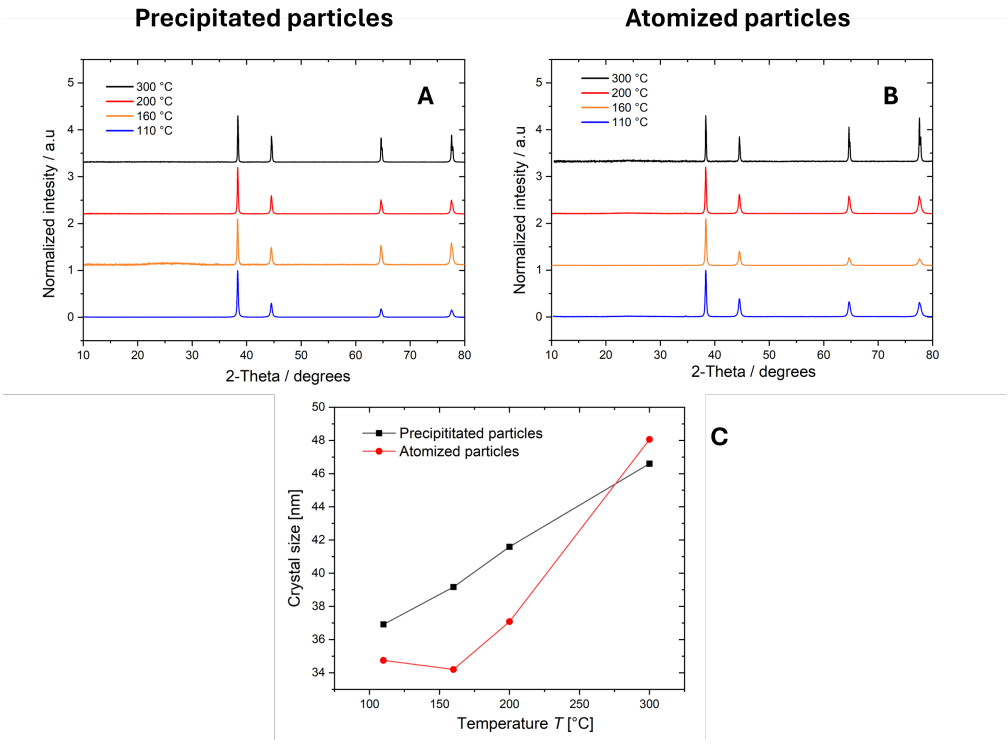

Figure S5: Grain growth due to sintering of both precipitated and atomized particles. (A) XRD graphs of precipitated particles and (B) atomized particles, treated at 110 , 160 , 200 , and 300 °C. (C) The grain size of precipitated and atomized particles at each temperature.

The grain sizes in Figure S5 were determined in the same way as described in Section 9.2.4.

9.2.6 Precipitated particles in commercial pastes

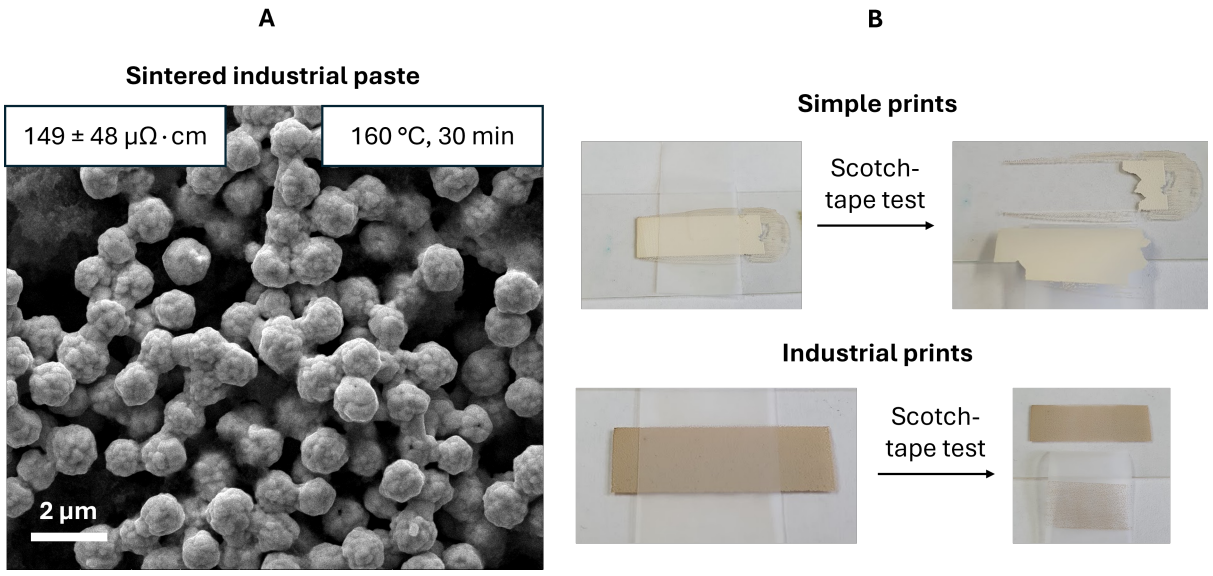

Figure S6: A comparison of sintering behavior and adhesion of prints based on simple pastes studied in the manuscript and industrial pastes made by our partner company. (A) A top-view SEM image of a sintered industrial paste containing 1 µm-diameter particles at 160 °C for 30 min. (B) Images before and after a scotch-tape test of simple prints from the manuscript (above) and industrial prints by pastes from our partner company (below).

We collaborated with a company that produces commercial screen-printing pastes (GSB Wahl) to test full formulations and tested prints from those pastes using standard scotch adhesion tests. Figure S6 shows that the standard matrix enhanced adhesion as expected. Importantly, the sintering behavior of the matrix-containing pastes was similar to the ethylene glycol-based pastes.

9.2.7 Statistics of the in-situ measurements: Precipitated particles

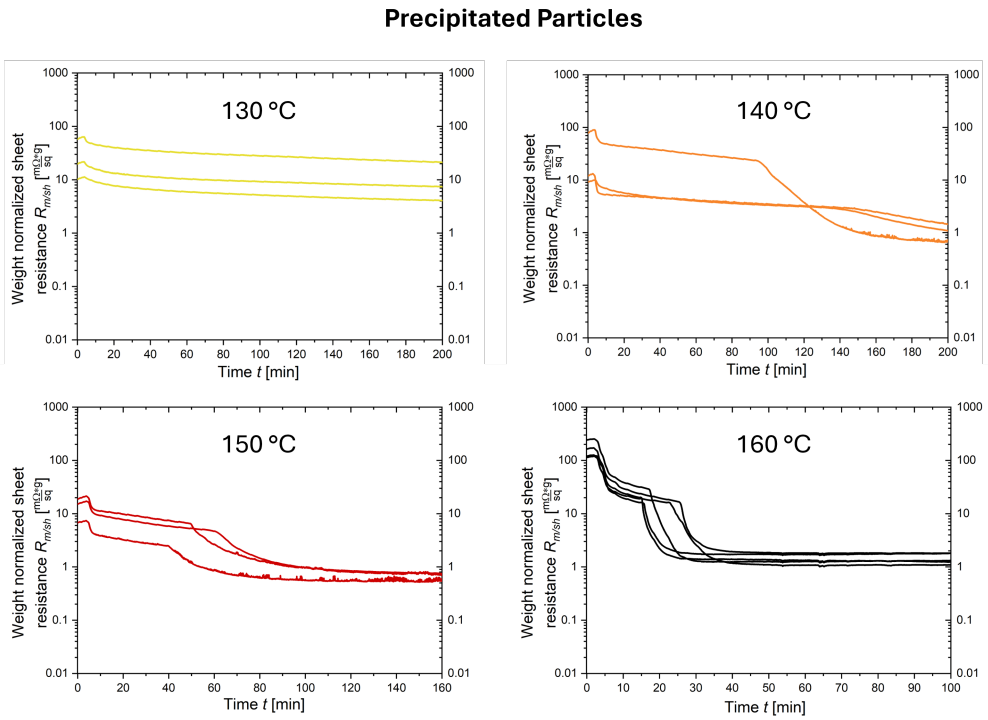

Figure S7: All in-situ measurements for each temperature for prints containing precipitated particles.

9.2.8 Statistics of the in-situ measurements: Atomized particles

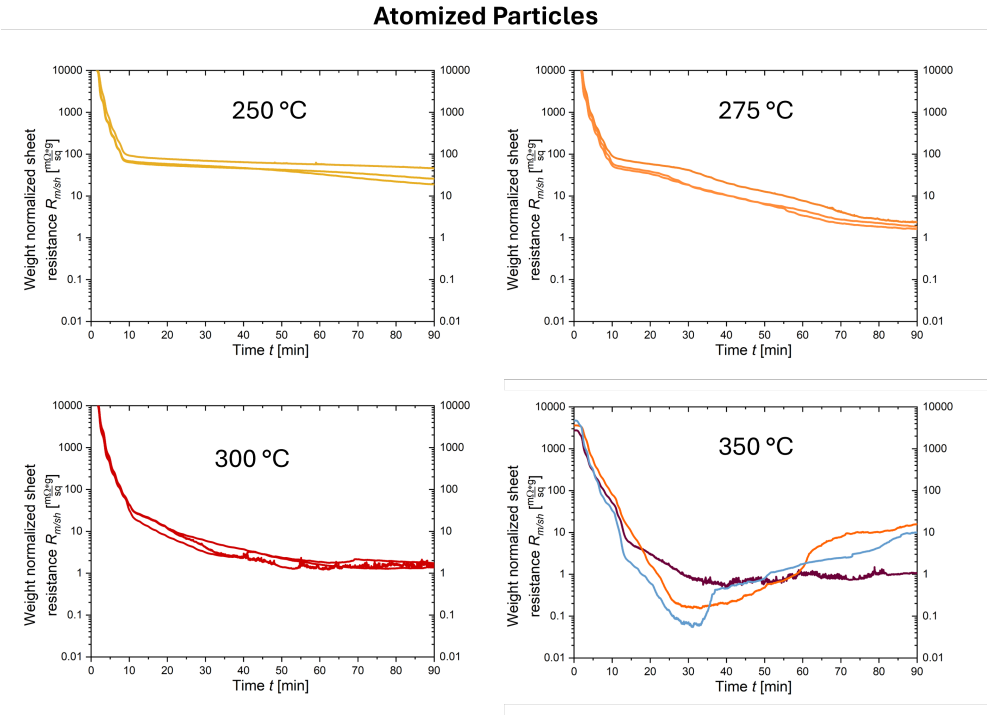

Figure S8: All in-situ measurements for each temperature for prints containing atomized particles.

9.2.9 Validation of the two-wire in-situ measurements

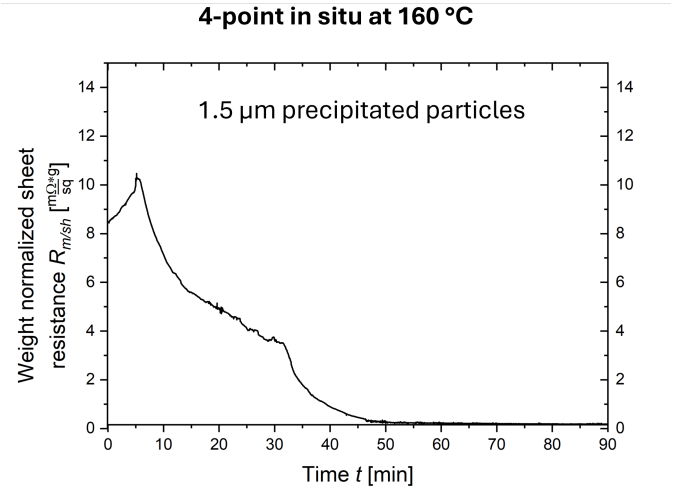

Figure S9: Validation of the two-wire measurements of Figure 3A and B. (A) Four-point in-situ measurement at 160 °C of 1.5 µm precipitated particles.

The reference 4-point measurement in Figure S9 yielded the same clearly defined sintering onset times as observed using the two-wire measurements in Figure 3.3A. The contact resistances of the two-wire in-situ measurements did not affect the onset times that we analyze in Section 3.3.2 of the manuscript.

9.2.10 Presence of residual solvent in the prints

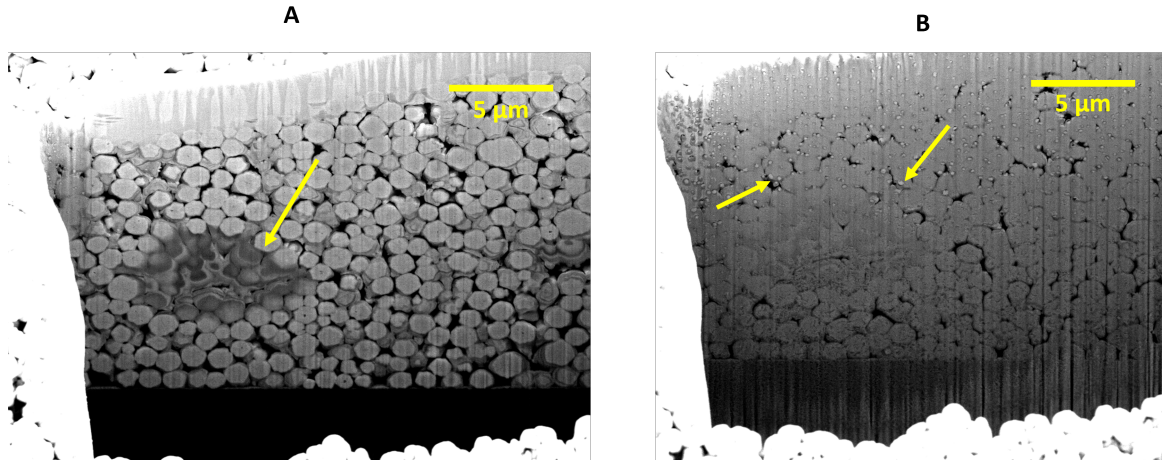

Figure S10: Cross-sectional SEM images of printed layers of 1 µm precipitated silver particles. The yellow arrow in (A) points at a dark spot caused by residual Ethylene Glycol. The yellow arrows in (B) point to droplets of Ethylene glycol still present in the printed structure. The droplets moved and evaporated within minutes during imaging, which can be explained by the exposure to the vacuum.

9.2.11 Sintering onset times determined from in-situ electrical characterization

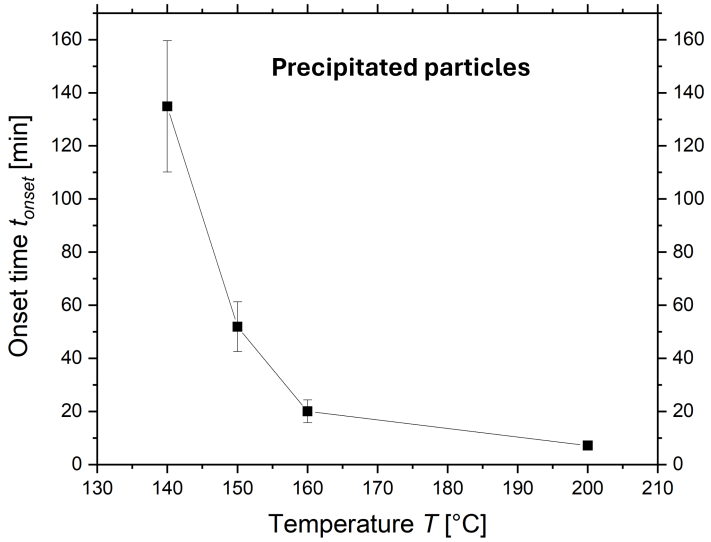

Figure S11: Average onset time as a function of temperature (130 , 140 , 150 , and 160 °C) for the sintering of precipitated particles. Each point in the graph represents the average onset time of sintering, determined from Figure 3A, with the standard deviation shown as an error bar.

9.2.12 Occurrence of nanoparticles after heat-treated prints

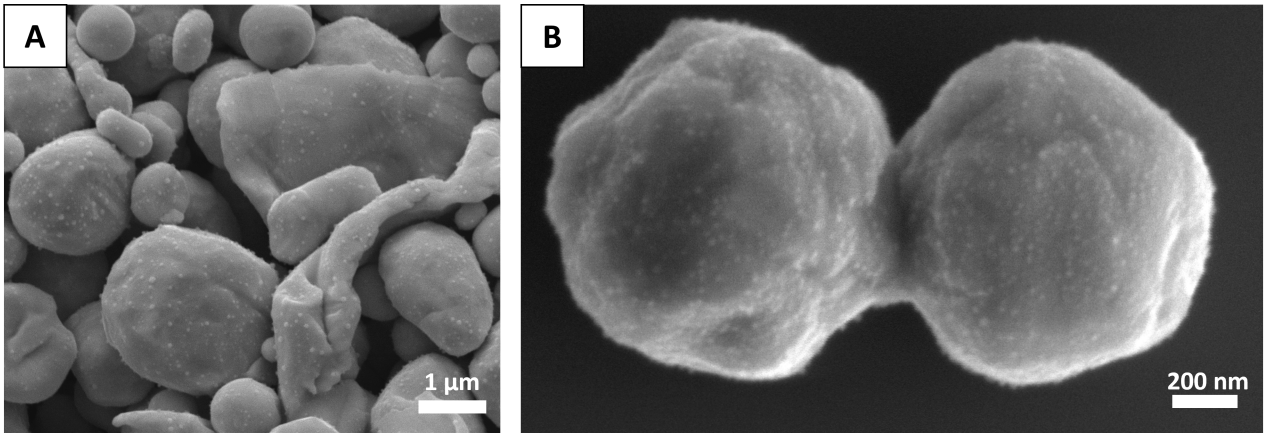

Figure S12: SEM images of (A) 1.7 µm atomized silver particles treated at 250 °C for 30 min and (B) 1 µm precipitated silver particles treated at 150 °C for 60 min. In both A and B silver nanoparticles can be observed on the surface of the microparticles.

9.2.13 Electron microscopy of reusable and non-reusable fractions after recycling

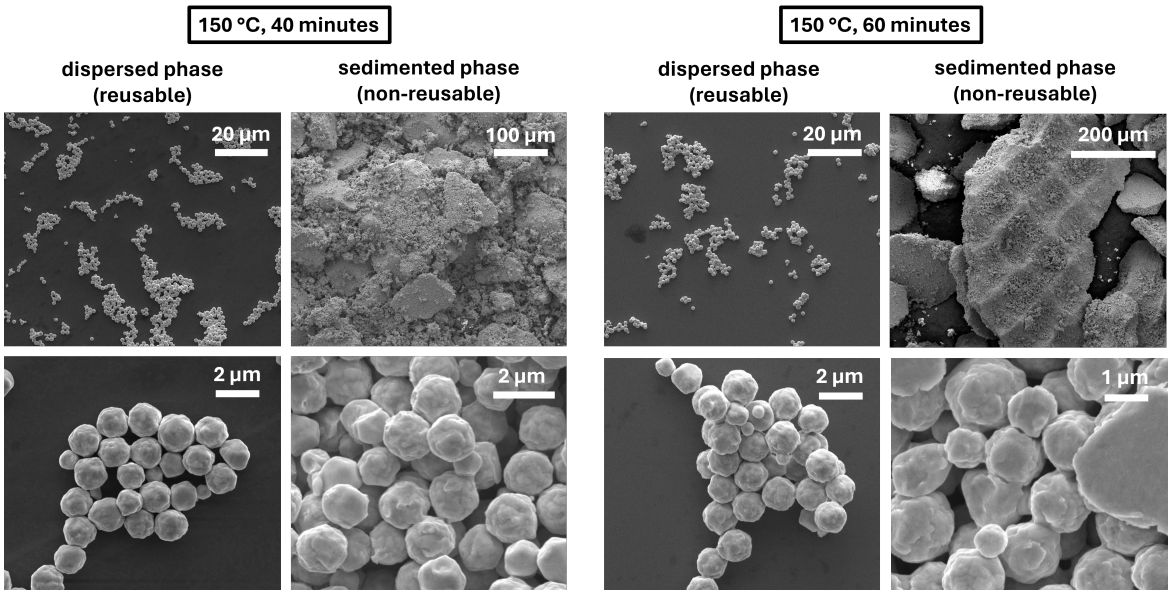

Figure S13: Scanning Electron Microscopy (SEM) images of precipitated particles after heat treatment and the recycling procedure. Both the dispersed phase (reusable powder) and the sedimented phase (non-reusable powder) are shown for precipitated particles treated for 40 and 60 min at 150 °C.

9.2.14 Particle size distributions of initial and recycled powder

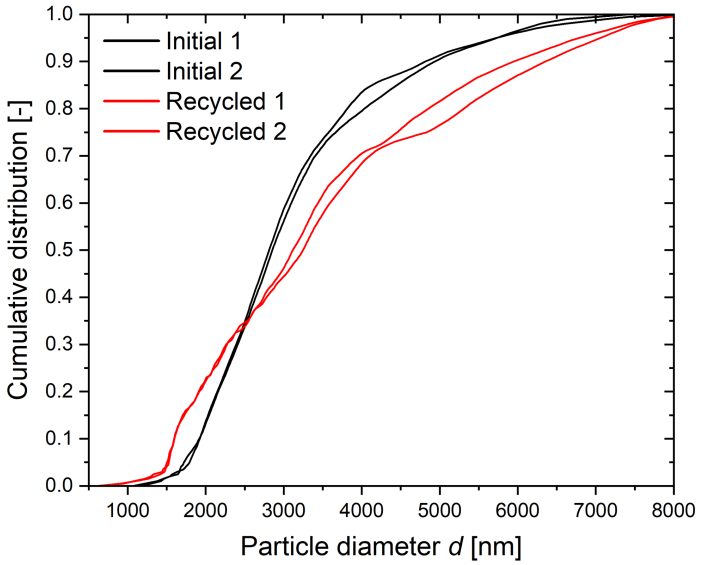

Figure S14: Cumulative, volume-weighted size distributions of initial and recycled precipitated silver powders. The printed layers underwent a heat treatment at 150 °C for 40 min before recycling. Both initial and recycled powders were measured in duplicate for reproducibility.

9.2.15 Profiles of initial and recycled prints

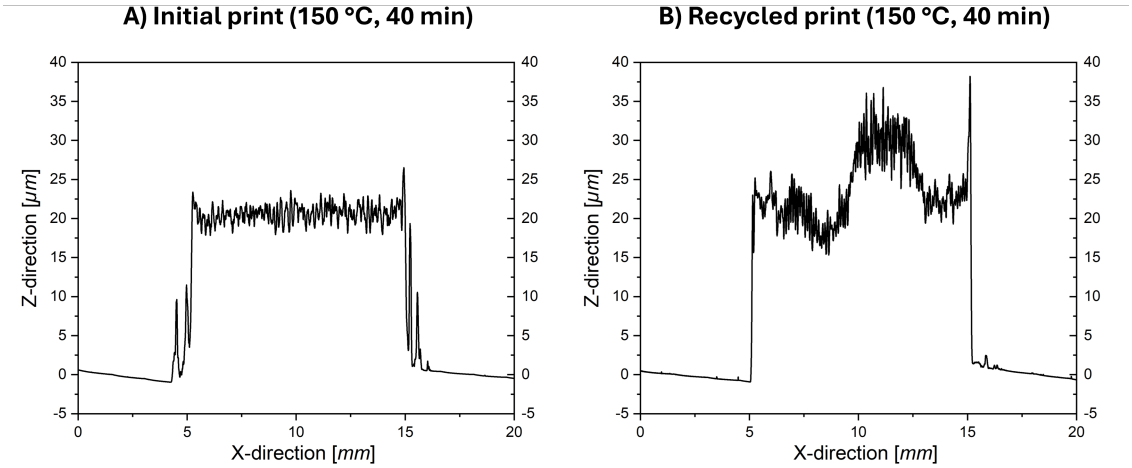

Figure S15: Thickness profiles of prints made with (A) fresh metal powders and (B) recycled metal powders. Both prints were treated at 150 °C for 40 min and measured using a 3D confocal microscope MarSurf CM explorer (Mahr, Germany).

9.2.16 Electrical evolution of resistance during heating of recycled prints

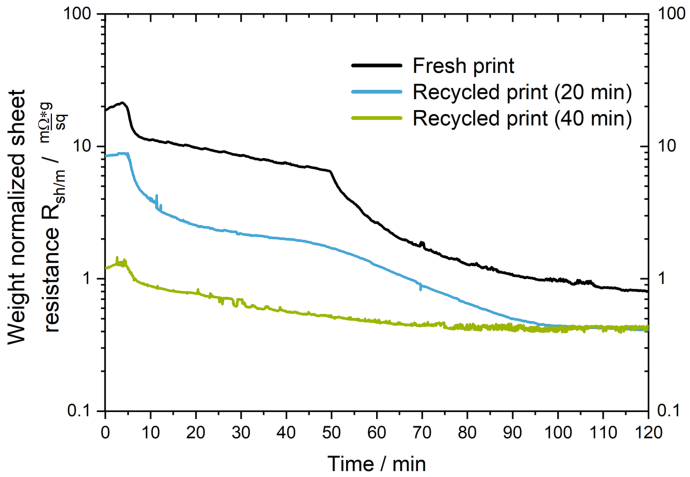

Figure S16: $R_{m/sh}$ is plotted as a function of T for prints containing fresh, recycled from 20 min at 150 °C, and recycled from 40 min at 150 °C precipitated 1.5 µm particles.

9.3 Chapter 4: The importance of shape: flakes and spheres in recyclable pastes for printed electronics

9.3.1 Prints of flakes and spheres treated at 110 °C

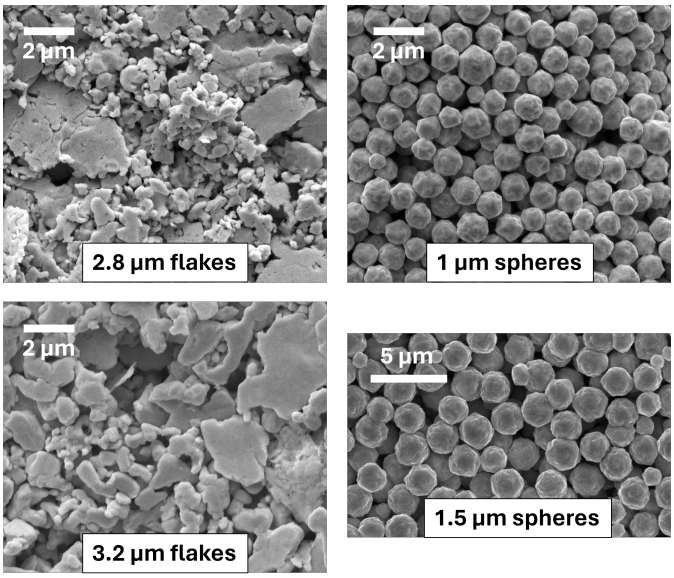

Figure S1: Top-view SEM images of flakes and spheres after 30 min at 110 °C. 2.8 and 3.2 µm flakes on the left, and 1 and 1.5 µm spheres on the right.

9.3.2 Porosity after sintering of flakes and spheres

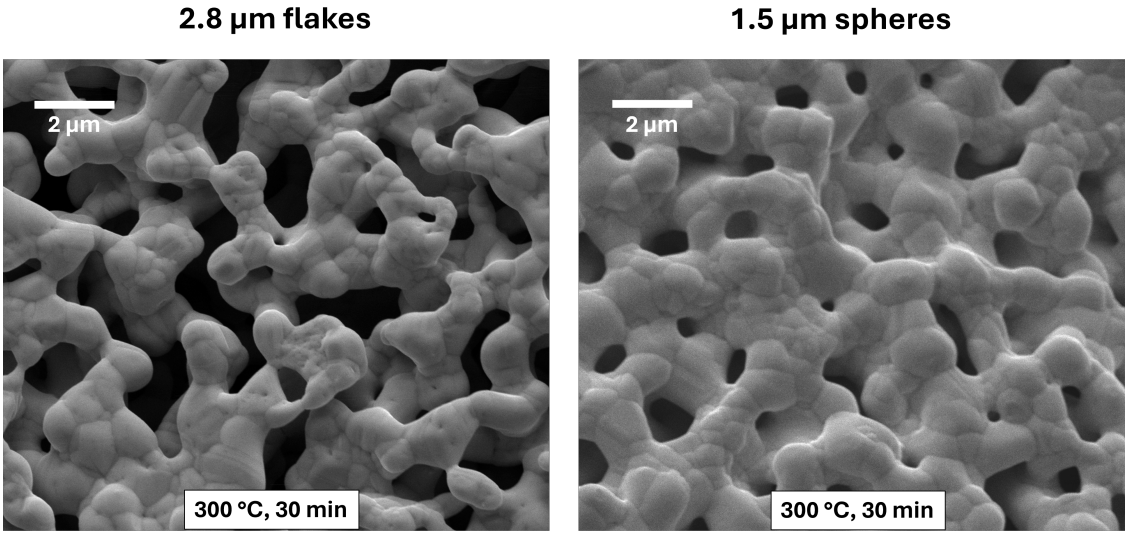

Figure S2: Comparison of the porosity of prints containing flakes and spheres after sintering at 300 °C. Top-view SEM images after sintering 2.8 µm flakes (left micrograph) and 1.5 µm spheres (right micrograph) for 30 min at 300 °C.

9.3.3 Grain size of sintered flakes and spheres

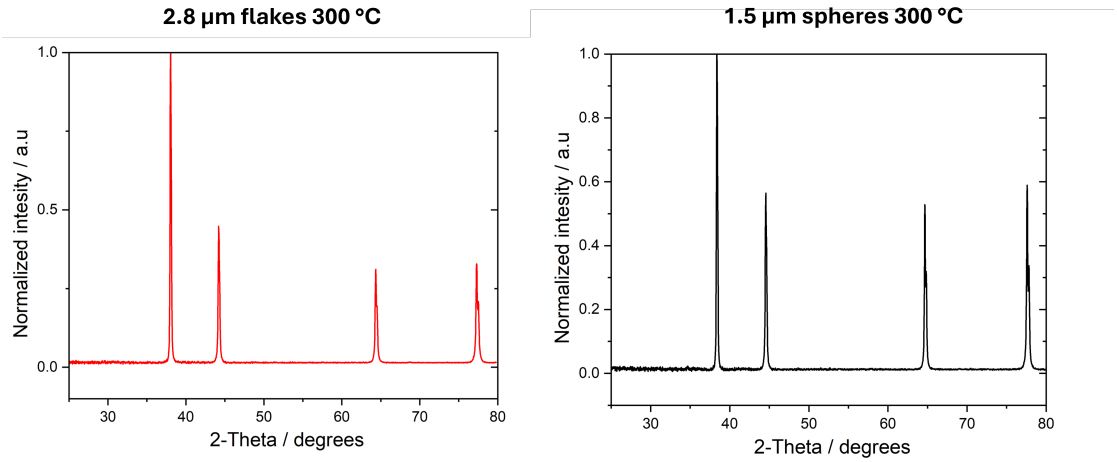

Figure S3: X-Ray Diffraction (XRD) graphs after sintering 2.8 µm flakes (left) and 1.5 µm spheres (right) for 30 min at 300 °C.

Crystallite sizes from XRD graphs in Figure S3 were calculated using Scherrer‘s formula:

$$D_p = \frac{K \cdot \lambda}{B \cdot \cos(\theta)}, \tag{9.2}$$

where D_p is the crystallite diameter in nm, K the Scherrer's constant ($K = 0.94$ is used, assuming spherical grains with cubic symmetry), λ the x-ray wavelength in nm, B the full width at half maximum of the observed peak, and θ the XRD peak position.

9.3.4 Effect of temperature on sinter necks

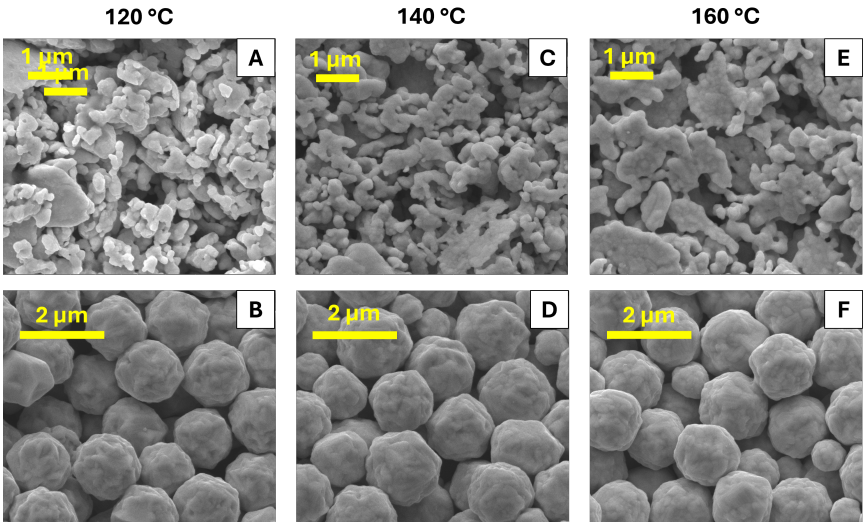

Figure S4: Top-view SEM images of 2.8 µm flakes (top row) and 1.5 µm spheres (bottom row) after sintering for 30 min at 120 , 140 , and 160 °C.

9.3.5 Sintered aggregates in recycled powder

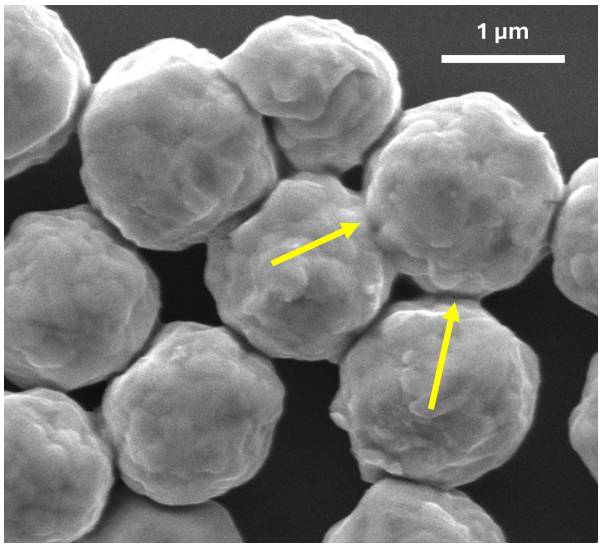

Figure S5: SEM image of recycled 1.5 µm spheres after sintering at 160 °C for 30 min.

9.4 Chapter 5: Towards the replacement of silver by copper for printed electronics.

9.4.1 Thermogravimetric analysis of precipitated copper particles

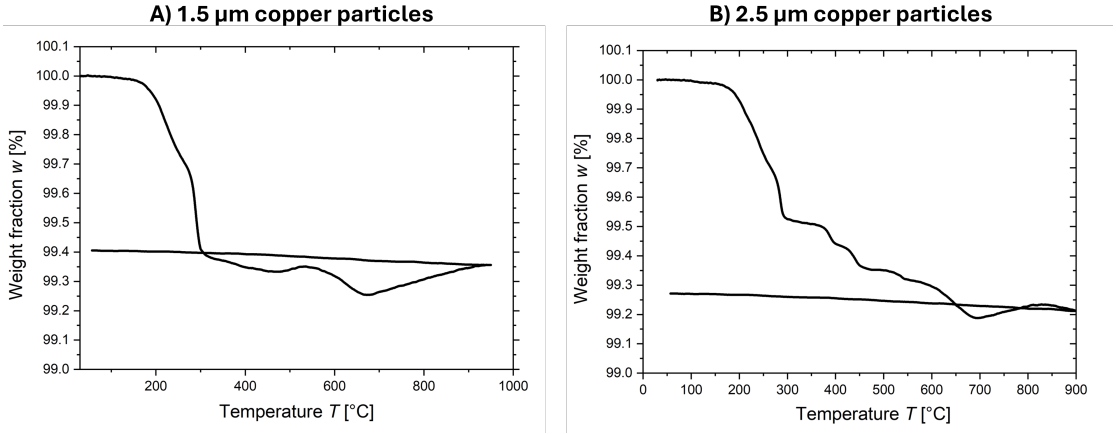

Figure S1: Thermogravimetric analysis (TGA) of precipitated copper particles. The weight fraction w is plotted as a function of the temperature T. (A) TGA of 1.5 µm copper particles, and (B) TGA of 2.5 µm copper particles.

9.5 Chapter 6: Low-temperature sintering of Cu@Ag microparticles in air for recyclable printed electronics

9.5.1 The silver coating

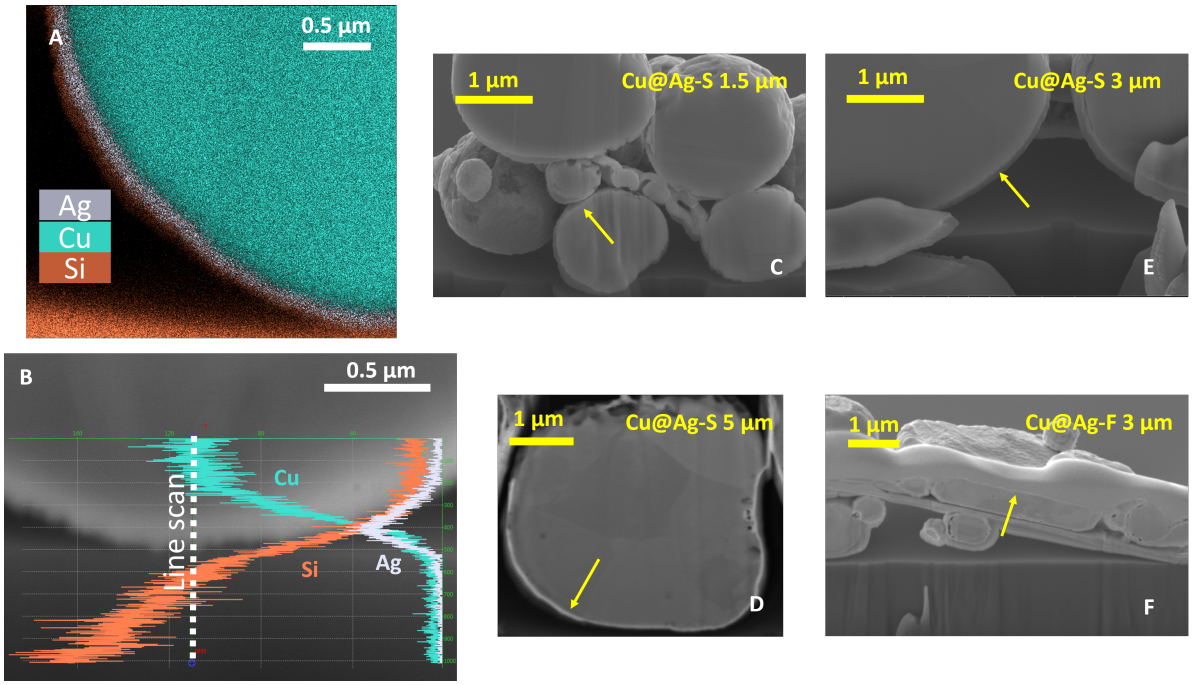

Figure S1: The silver coating thickness was determined via cross-sectional SEM imaging. (A) EDX mapping of a cross-sectional backscattered electron image of the 5 µm Cu@Ag-S. (B) EDX line scan of a cross-sectional backscattered electron image of the 5 µm Cu@Ag-S. (C-F) The images from which the silver coating thickness of 1.5 , 3 , and 5 µm Cu@Ag-S, and 3 µm Cu@Ag-F were determined. The yellow arrows indicate where the silver coating can be spotted in the image.

9.5.2 The effect of using L-Ascorbic Acid

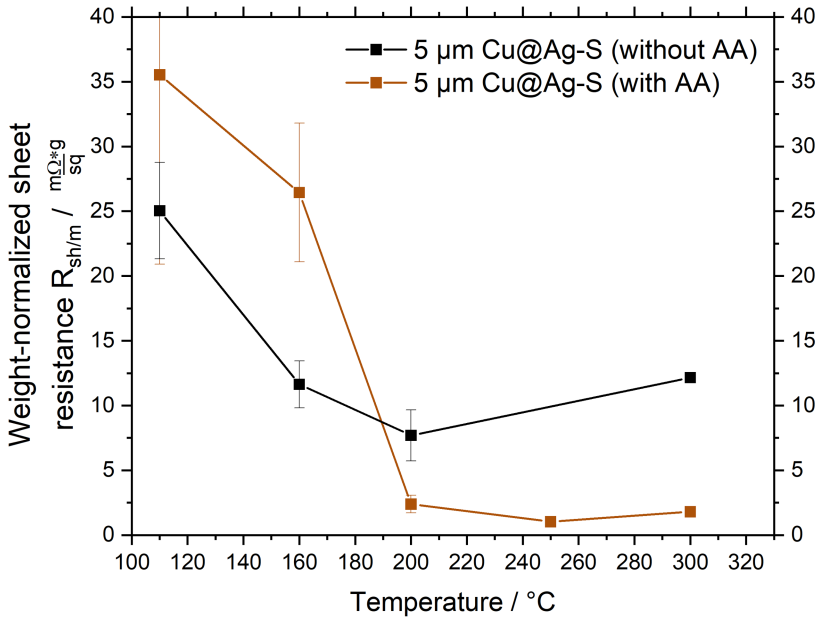

Figure S2: The effect of using L-Ascorbic Acid (AA) in the paste formulation of coated copper particles is demonstrated. $R_{m/sh}$ as a function of temperature T is plotted for prints made from 5 µm Cu@Ag-S pastes with (brown line) and without (black line) the addition of AA.

9.5.3 Internal pore formation at the silver-copper interface

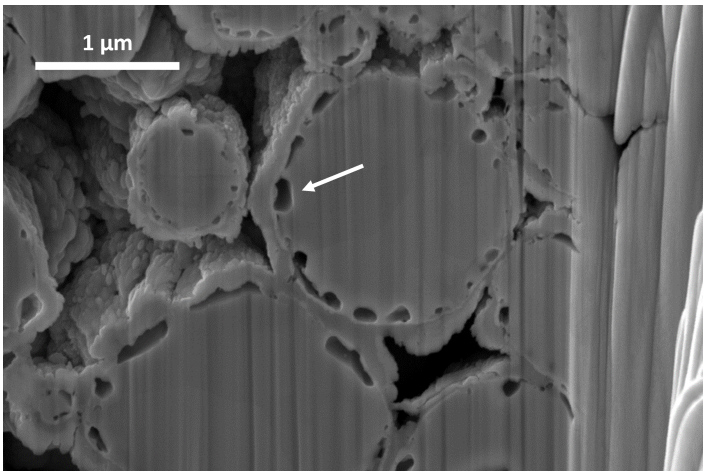

Figure S3: The formation of internal pores at the copper-silver interface. A cross-sectional SEM image of a print made from 3 µm Cu@Ag-S treated at 250 °C for 90 min. The white arrow indicates one of the pores that formed at the copper-silver interface.